Title
Nonconvex Sparse Recovery Methods

Permalink
https://escholarship.org/uc/item/2099g1s6

Author
Adhikari, Lasith

Publication Date
2017

Peer reviewed|Thesis/dissertation

UNIVERSITY OF CALIFORNIA, MERCED

Nonconvex Sparse Recovery Methods

A dissertation submitted in partial satisfaction of the
requirements for the degree
Doctor of Philosophy

in

Applied Mathematics

by

Lasith Adhikari

Committee in charge:

Professor Roummel F. Marcia, Chair
Professor Arnold D. Kim
Professor Changqing Li

2017

The dissertation of Lasith Adhikari is approved, and it is acceptable in quality and form for publication on microfilm and electronically:

(Professor Arnold D. Kim)

(Professor Changqing Li)

(Professor Roummel F. Marcia, Chair)

University of California, Merced

2017

This dissertation work is dedicated to my dearest parents, Swarana, Hemanta, and my sister Nipuni and to my lovely wife Madushani.

EPIGRAPH

The Universe is sparse,
but life is dense.
— Lasith Adhikari

TABLE OF CONTENTS

LIST OF TABLES

LIST OF NOTATIONS AND ABBREVIATIONS

Notations

$\mathbf{f}^*$: Signal or image vector to be reconstructed

$\hat{\mathbf{f}}$: Estimate of the signal or image vector

$\mathbf{y}$: Measurement vector corrupted by Poisson noise

$\mathbf{b}$: Measurement vector corrupted by Gaussian noise

$\mathbf{A}$: System matrix or observation matrix

$\mathbf{I}$: Identity matrix

$\mathbf{W}$: Orthonormal matrix

$\mathbf{1}$: Vector of ones

Abbreviations

1D : 1-Dimension

2D : 2-Dimension

3D : 3-Dimension

ADMM : Alternating Direction Method of Multipliers

BB : Barzilai and Borwein

BCD : Block Coordinate Descent

BFGS : Broyden-Fletcher-Goldfarb-Shanno

BLT : Bioluminescence Tomography

CCD : Charge-Coupled Device

CNR : Contrast-to-Noise Ratio

CS : Compressed Sensing

CT : Computed Tomography

dB : Decibel

DNA : Deoxyribonucleic Acid

FISTA : Fast Iterative Shrinkage-Thresholding Algorithm

FLIM : Fluorescence Lifetime Imaging

FMT	:	Fluorescence Molecular Tomography
GASV	:	Geometric Analysis of Structural Variants
GPSR	:	Gradient Projection for Sparse Reconstruction
GST	:	Generalized Soft-Thresholding
IEEE	:	Institute of Electrical and Electronics Engineers
JP	:	Justice Pursuit
LASSO	:	Least Absolute Shrinkage and Selection Operator
L-BFGS	:	Limited-Memory Broyden-Fletcher-Goldfarb-Shanno
MRI	:	Magnetic Resonance Imaging
MSE	:	Mean-Squared Error
NUMOS	:	Non-Uniform Multiplicative Weighting with Ordered Subsets
PET	:	Positron Emission Tomography
PSNR	:	Peak Signal to Noise Ratio
QR	:	Quick Response
RGB	:	Red, Green and Blue
RMSE	:	Root-Mean-Square Error
ROC	:	Receiver Operating Characteristic
SNR	:	Signal to Noise Ratio
SPECT	:	Single Photon Emission Computed Tomography
SPIRAL	:	Sparse Poisson Intensity Reconstruction ALgorithm
SV	:	Structural Variant
TrustSpa	:	Trust-Region Method for Sparse Relaxation
TV	:	Total Variation
VR	:	Volume Ratio
YALL1	:	Your ALgorithm for L1

ACKNOWLEDGEMENTS

I would also like to thank Prof. Sunethra Weerakoon, Dr. Menaka Liyanage, and Dr. Jayantha Lanel, who are faculty members at the University of Sri Jayewardenepura, Sri Lanka, who provided me with support and motivation in pursuing a Ph.D. degree.

I deeply thank my parents, Swarna Adhikari and Hemanta Adhikari, for their unconditional trust, timely encouragement, and endless patience.

Finally, and most importantly, I am grateful to my wife Anusha Madushani for her support, encouragement, patience, and delicious food to get through this agonizing period in the most positive way.

VITA

2008	B. Sc. (Hons) in Information Technology, Sri Lanka Institute of Information Technology, Sri Lanka
2010	B. Sc. (Special) in Mathematics, University of Sri Jayewardenepura, Sri Lanka
2017	Ph. D. in Applied Mathematics, University of California, Merced, USA

PUBLICATIONS

L. Adhikari and R. Marcia, "Nonconvex relaxation for Poisson intensity reconstruction," *Proceedings of 2015 IEEE International Conference on Acoustics, Speech and Signal Processing*, April 2015.

L. Adhikari and R. Marcia, "p-th power total variation regularization in photon-limited imaging via iterative reweighting," *Proceedings of 2015 European Signal Processing Conference*, September 2015.

L. Adhikari, D. Zhu, C. Li, and R. Marcia, "Nonconvex reconstruction for low-dimensional fluorescence molecular tomographic Poisson observations," *Proceedings of 2015 IEEE International Conference on Image Processing*, September 2015.

A. Orkusyan, L. Adhikari , J. Valenzuela, and R. Marcia, "Analysis of p-norm regularized subproblem minimization for sparse photon-limited image recovery," *Proceedings of 2016 IEEE International Conference on Acoustics, Speech and Signal Processing*, March 2016.

M. Banuelos, R. Almanza, L. Adhikari , S. Sindi, and R. Marcia, "Sparse signal recovery methods for variant detection in next-generation sequencing data," *Proceedings of 2016 IEEE International Conference on Acoustics, Speech and Signal Processing*, March 2016.

M. Banuelos, R. Almanza, L. Adhikari, R. Marcia, and S. Sindi, "Sparse genomic structural variant detection: exploiting parent-child relatedness for signal recovery," *Proceedings of 2016 IEEE Workshop on Statistical Signal Processing*, June 2016.

M. Banuelos, R. Almanza, L. Adhikari, R. Marcia, and S. Sindi, "Constrained variant detection with SPaRC: Sparsity, Parental Relatedness, and Coverage," *Proceedings of International Conference of the IEEE Engineering in Medicine and Biology Society*, August 2016.

L. Adhikari and R. Marcia, "Bounded sparse photon-limited image recovery," *Proceedings of 2016 IEEE International Conference on Image Processing*, September 2016.

L. Adhikari, R. Marcia, J. B. Erway, and R. J. Plemmons, "Trust-region methods for nonconvex sparse recovery optimization," *Proceedings of 2016 International Symposium on Information Theory and Its Applications*, November 2016.

L. Adhikari, A. D. Kim, and R. Marcia, "Nonconvex sparse Poisson intensity reconstruction for time-dependent bioluminescence tomography," *Proceedings of 2016 International Symposium on Information Theory and Its Applications*, November 2016.

L. Adhikari, A. D. Kim, and R. Marcia, "Sparse reconstruction for fluorescence lifetime imaging microscopy with Poisson noise," *Proceedings of 2016 IEEE Global Conference on Signal and Information Processing*, December 2016.

L. Adhikari and R. Marcia, "Non-convex sparse optimization for photon-limited imaging," *Proceedings of M.Sc./Ph.D. Forum in the 2017 IEEE International Conference on Acoustics, Speech and Signal Processing*, March 2017.

M. Banuelos, L. Adhikari, A. Fujikawa, J. Sahagún, K.Sanderson, M. Spence, R. Almanza, S. Sindi, and R. Marcia, "Nonconvex regularization for sparse genomic variant signal detection," *Accepted to 2017 IEEE International Symposium on Medical Measurements and Applications*, 2017.

M. Banuelos, L. Adhikari, A. Fujikawa, J. Sahagún, K.Sanderson, M. Spence, R. Almanza, S. Sindi, and R. Marcia, "Sparse diploid spatial biosignal recovery for genomic variation detection," *Accepted to 2017 IEEE International Symposium on Medical Measurements and Applications* , 2017.

M. Banuelos, R. Almanza, L. Adhikari, S. Sindi, and R. Marcia, "Biomedical signal recovery: Genomic variant detection in family lineages," *Proceedings of 2017 IEEE 5th Portuguese Meeting on Bioengineering*, 2017.

L. Adhikari, J. Erway, S. Lockhart, and R. Marcia, "Limited memory trust-region methods for sparse relaxation," *Accepted to SPIE: Wavelets and Sparsity XVII*, 2017.

L. Adhikari and R. Marcia, "Non-convex Shannon entropy for photon-limited imaging," *Accepted to SPIE: Wavelets and Sparsity XVII*, 2017.

F. Wen, L. Adhikari, P. Liu, R. Marcia, and W. Yu, "Recovery and demixing of sparse signals using nonconvex regularization," *Submitted*, 2017.

ABSTRACT OF THE DISSERTATION

Nonconvex Sparse Recovery Methods

by

Lasith Adhikari

Doctor of Philosophy in Applied Mathematics

University of California Merced, 2017

Professor Roummel F. Marcia, Chair

Critical to accurate reconstruction of sparse signals from low-dimensional observations is the solution of nonlinear optimization problems that promote sparse solutions. Sparse signal recovery is a common problem of many different applications ranging from photography to tomography and from radiology to biology. Within the compressive imaging community, minimizing the ℓ_1-norm or the total variation (TV) seminorm penalized least-squares problem is the most conventional approach for sparse signal recovery. The least-squares data-fidelity term assumes a Gaussian noise model. However, there are many real-world applications that do not follow Gaussian noise statistics. For an instance, when the number of observed photon counts is relatively low at the camera detector, they are corrupted by Poisson noise. This phenomenon can be seen in a variety of different applications including astronomy, night vision, and medical imaging. Therefore, the contribution of the dissertation to sparse signal recovery is two-fold. First, we propose several nonconvex algorithms operate on Poisson statistics to promote sparsity. Second, we will present methods based on trust-region and alternating minimization techniques for sparse signal recovery under Gaussian statistics.

While convex optimization for low-light imaging has received some attention by the imaging community, non-convex optimization techniques for photon-limited imaging are still in their nascent stages. Theoretically, the non-convex ℓ_p-norm regularization $(0 \leq p < 1)$ would lead to more accurate reconstruction than the

convex ℓ_1-norm relaxation. In this dissertation, we explore sparse Poisson intensity reconstruction methods using gradient based optimization approach with the nonconvex regularization techniques: ℓ_p-norm, TV_p-seminorm, and the *generalized* Shannon entropy. The proposed methods lead to more accurate and high strength reconstructions in medical imaging and computational genomics. In particular, we developed a stage-based nonconvex approach to solve time dependent bioluminescence and fluorescence lifetime imaging problems in the Poisson noise context.

In Gaussian noise context, we solve the ℓ_2-ℓ_1 and ℓ_2-ℓ_p sparse recovery problems by transforming the objective function into an unconstrained differentiable function and apply a limited-memory trust-region method. Unlike gradient projection-type methods, which uses only the current gradient, our approach uses gradients from previous iterations to obtain a more accurate Hessian approximation. Numerical experiments with simulated compressive sensing 1D and 2D data are provided to illustrate that our proposed approach eliminates spurious solutions more effectively while improving the computational time to converge in comparison to standard approaches. Moreover, we employ nonconvex ℓ_p-norm regularization for better recovery and demixing of sparse signals arise in image inpainting and source separation applications.

Chapter 1

Introduction

Over the course of this dissertation, I will present methods for accurate reconstruction of sparse signals from low dimensional observations with applications to medical imaging, signal processing, and computational genomics. In particular, we will discuss algorithms that can be used for sparse recovery in Gaussian noise and Poisson noise contexts separately. Before we begin, I would like to motivate our research work and outline our main contributions to sparse recovery in this chapter.

1.1   Sparse Signal Recovery

Most signals such as images and sounds seem to carry an overwhelming amount of data, however, they contain a lot of redundant information and repeated hidden patterns. These signals have a high level of *sparsity* – signals can be represented by relatively few number of crucial information components. For example, natural images are often sparse in wavelet (see Fig. 1.1(b)) or discrete cosine basis. These transformations typically help to discard redundant information before we store them in electronic devices. In medical imaging, magnetic resonance images have sparsity properties in Fourier basis, while some fluorescence molecular tomography signals are known to be sparse in the canonical basis with relatively small targets (see Fig. 1.1(c)). Moreover, sparse signal representations can be seen in many different applications including seismic imaging, DNA microarray sensing, com-

Source: T. J. Muldoon *et al.*, Optics Express, 2007.

(a)   (b)   (c)
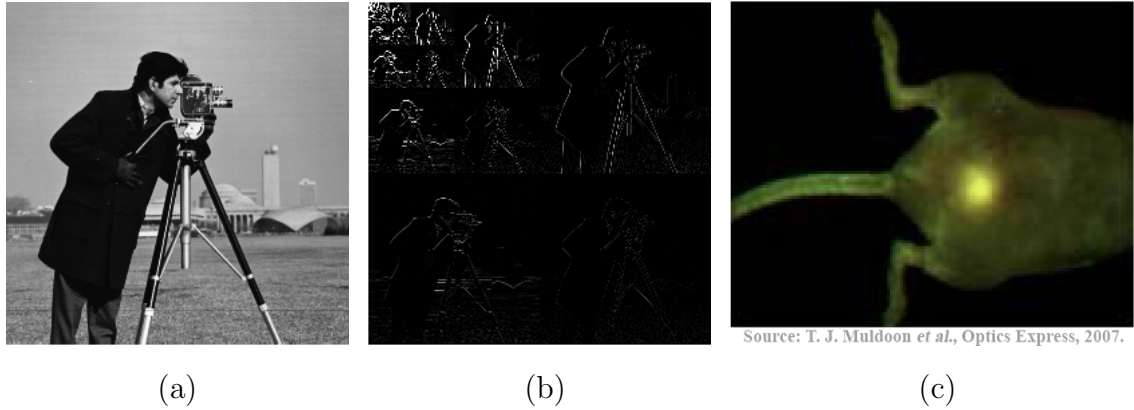
Figure 1.1: (a) The "Cameraman" image. (b) Sparse wavelet coefficients of the "cameraman" image in (a). (c) Sparse fluorescence target in medical imaging.

munication, and networks [103]. Due to the diversity of its applications, sparse signal recovery has attracted the attention of statistician, mathematicians, and engineers. Mathematically, if $\mathbf{f}^* \in \mathbb{R}^{\mathbf{n}}$ represents the true signal or image vector to be recovered, then the measurement process is typically modeled as a discrete linear system of the form

$$\mathbf{y_t} = \mathbf{A}\mathbf{f}^*, \tag{1.1}$$

where $\mathbf{y_t} \in \mathbb{R}^{\mathbf{m}}$ is a vector of observed true measurements and $\mathbf{A} \in \mathbb{R}^{\mathbf{m} \times \mathbf{n}}$ is a projection matrix. If $\mathbf{f}^*$ is sparse in sparsifying basis $\mathbf{W} \in \mathbb{R}^{\mathbf{n} \times \mathbf{n}}$, then $\mathbf{f}^*$ in (1.1) can be replaced by $\mathbf{W}\boldsymbol{\theta}^*$ (i.e., $\mathbf{y_t} = \mathbf{A}\mathbf{W}\boldsymbol{\theta}^*$), where the sparse coefficients are now given by $\boldsymbol{\theta}^* \in \mathbb{R}^n$ (if $\mathbf{f}^*$ is sparse itself, then $\mathbf{f}^* = \boldsymbol{\theta}^*$ and $\mathbf{W} = \mathbf{I}$). The linear projection matrix $\mathbf{A}$ is constructed based on the application. For example, in image deblurring applications, $\mathbf{A}$ is computed using a convolution with a blur kernel. In optical tomography, $\mathbf{A}$ is constructed based on light propagation inside of a tissue sample. In practice, the true measurements $\mathbf{y_t}$ are corrupted by noise which is due to measuring hardware issues, quantization error, and transmission channel errors [84]. Next I describe sparse recovery under two noise settings: Gaussian noise and Poisson noise.

1.1.1 Recovery under Gaussian Noise

Under Gaussian noise, we modify the measurement process in (1.1) by adding a noise vector $\mathbf{w} \in \mathbb{R}^{\mathbf{m}}$ to the true measurement vector $\mathbf{y_t}$, which is generated from Gaussian distribution with zero-mean and variance σ^2:

$$
\begin{aligned}
\mathbf{y_t} + \mathbf{w} &\approx \mathbf{Af}^* & (1.2) \\
\mathbf{b} &\approx \mathbf{Af}^*, & (1.3)
\end{aligned}
$$

where measurement vector $\mathbf{b} = \mathbf{y_t} + \mathbf{w} \in \mathbb{R}^{\mathbf{m}}$ is corrupted by Gaussian noise.

In the inverse problem setting, i.e., $\mathbf{f}^*$ is to be recovered when $\mathbf{b}$ and $\mathbf{A}$ are given, a most straightforward method is to follow the least squares approach that estimates $\mathbf{f}^*$ by minimizing the discrepancy between corrupted measurements and its prediction:

$$
\hat{\mathbf{f}} = \arg\min_{\mathbf{f} \in \mathbb{R}^n} \|\mathbf{Af} - \mathbf{b}\|_{\mathbf{2}}^{\mathbf{2}}. \tag{1.4}
$$

It can be shown that this least squares model is proportional to the negative Gaussian log-likelihood function:

$$
\|\mathbf{Af} - \mathbf{b}\|_2^2 \quad \propto \quad -\sum_{i=1}^{m} \log\left[\mathrm{p}(b_i | (\mathbf{Af})_i)\right].
$$

However, in some applications such as medical imaging, we observe only low-dimensional measurements at the tissue boundary. In that case, the optimization problem in (1.4) becomes ill-posed. In addition, the system matrix $\mathbf{A}$ often becomes ill-conditioned in many applications (e.g., high scattering and high absorption of light inside tissue make $\mathbf{A}$ ill-conditioned [51]) that leads $\hat{\mathbf{f}}$ to be unstable [28]. To obtain a stable and unique solution, we incorporate a regularization term to the problem (1.4). The Tikhonov regularization [126] is one of the most popular techniques in which an ℓ_2-norm term is added to the objective function of (1.4):

$$
\hat{\mathbf{f}} = \arg\min_{\mathbf{f} \in \mathbb{R}^n} \|\mathbf{Af} - \mathbf{b}\|_{\mathbf{2}}^{\mathbf{2}} + \tau \|\mathbf{f}\|_{\mathbf{2}}^{\mathbf{2}}, \tag{1.5}
$$

where $\tau > 0$ is a regularization parameter. The ℓ_2-norm regularized problem (1.5) is simple and efficient to solve using gradient based methods; however, the resulting

solution is over smoothed [82]. In sparse recovery, since the true signal is sparse or sparse in some other basis, the reconstruction $\hat{\mathbf{f}}$ also should be sparse. With this prior knowledge, a sparse solution can be achieved by incorporating the ℓ_0-norm regularization term, which counts the number of nonzero entries in the solution, to the original problem:

$$\hat{\mathbf{f}} = \arg\min_{\mathbf{f} \in \mathbb{R}^n} \|\mathbf{Af} - \mathbf{b}\|_2^2 + \tau \|\mathbf{f}\|_0,$$

Solving the ℓ_0-norm minimization problem is NP-hard and computationally infeasible for high-dimensional problems [94]. As a good approximation to the ℓ_0-norm, the ℓ_1-norm regularization has been used to promote the sparsity of the solution:

$$\hat{\mathbf{f}} = \arg\min_{\mathbf{f} \in \mathbb{R}^n} \|\mathbf{Af} - \mathbf{b}\|_2^2 + \tau \|\mathbf{f}\|_1,$$

where $\|\mathbf{f}\|_1 = \sum_i |f_i|$. Recovering such a sparse signal only using fewer measurements is the main problem of compressed sensing (CS) [48]. Much of the early research work on sparse signal recovery with the ℓ_1-norm can be found in [38, 49, 134, 91, 61, 142], to name just a few.

Theoretically, nonconvex ℓ_p-norm ($0 < p < 1$) should lead to more accurate sparse reconstruction than the convex ℓ_1-norm relaxation. The optimization problem with ℓ_p-norm relaxation is given by

$$\hat{\mathbf{f}} = \arg\min_{\mathbf{f} \in \mathbb{R}^n} \|\mathbf{Af} - \mathbf{b}\|_2^2 + \tau \|\mathbf{f}\|_p^p, \tag{1.6}$$

where $\|\mathbf{f}\|_p^p = \sum_i |f_i|^p$. The problem (1.6) is nonconvex and global minimum is difficult to trace. However, Chartrand demonstrated that the local minimum of this nonconvex problem can produce exact sparse reconstruction with many fewer measurements than the ℓ_1-norm required. Accurate reconstruction of sparse signals/image from few number of measurements is crucial in application such as radiation-based medical imaging (to reduce radiation doses for patients). According to the literature, ℓ_p-norm regularization has garnered significant recent attention due to the better recovery performance in many applications (see e.g., [101, 81, 146, 89, 137]).

1.1.2 Recovery under Poisson Noise

There are many real world situations, where the measurement noise does not follow a Gaussian distribution but a Poisson distribution. This phenomena occurs in a wide variety of real world applications, including astronomy [66, 117], medical imaging [115] (such as Positron Emission Tomography (PET), Single Photon Emission Computed Tomography (SPECT), and fluorescent tomohraphy), night vision, traffic models [129], and computational genomics [18]. Under the inhomogeneous Poisson process model [113], we can write our measurement process as

$$\mathbf{y} \sim \text{Poisson}(\mathbf{A}\mathbf{f}^*), \tag{1.7}$$

where measurement $\mathbf{y} \in \mathbb{Z}_+^m$ is corrupted by Poisson noise (also known as *shot noise*), $\mathbf{A} \in \mathbb{R}_+^{m \times n}$ is a linear projection matrix, and $\mathbf{f}^* \in \mathbb{R}_+^n$ is the nonnegative true signal/image of interest.

Under the Poisson process model (1.7), an unknown true signal $\mathbf{f}^*$ is estimated by minimizing the negative Poisson log-likelihood function

$$F(\mathbf{f}) = \mathbf{1}^T \mathbf{A} \mathbf{f} - \sum_{i=1}^{m} y_i \, \log(\mathbf{e}_i^T \mathbf{A} \mathbf{f}), \tag{1.8}$$

where $\mathbf{1}$ is an m-vector of ones, $\mathbf{e}_i$ is the i-th column of the $m \times m$ identity matrix. In particular, the function $F(\mathbf{f})$ in (1.8) is derived using the *maximum likelihood principle*: given $\mathbf{y}$, choose the parameter of interest $\mathbf{A}\mathbf{f}^*$ in such a way that the data are most likely (see Appendix A.1 for details).

In our research, $\mathbf{f}^*$ is estimated from measurement vector $\mathbf{y}$, when

1) the true signal $\mathbf{f}^*$ is known to be sparse or sparse in some basis $\mathbf{W}$ (i.e., $\mathbf{f}^* = \mathbf{W}\boldsymbol{\theta}$, where $\boldsymbol{\theta}$ is sparse approximation), and

2) the dimension of the true signal $\mathbf{f}^*$ is larger than the dimension of the measurement $\mathbf{y}$.

Therefore, the estimation of $\mathbf{f}^*$ is related to the *compressed sensing* framework [48], but our research is mostly connected to the general problem of sparse signal recovery in the context of Poisson noise. In particular, Poisson sparse recovery

problems such as tomographic reconstruction in photon-limited medical imaging will restrict the matrix $\mathbf{A}$ and the signal $\mathbf{f}^*$ to be nonnegative. This nonnegativity of $\mathbf{f}^*$ will introduce a set of inequality constraints to the problem and would lead to a more challenging optimization problem.

To avoid the singularity of negative Poisson log-likelihood function (1.8) when $\mathbf{f} = 0$, a small parameter $\beta > 0$ (typically $\beta \ll 1$) is used inside the log function [57]. Then the function (1.8) can be rewritten as

$$F(\mathbf{f}) = \mathbf{1}^T \mathbf{A}\mathbf{f} - \sum_{i=1}^m y_i \, \log(\mathbf{e}_i^T \mathbf{A}\mathbf{f} + \beta), \tag{1.9}$$

which is convex. Approximating $\mathbf{f}^*$ by minimizing $F(\mathbf{f})$ in (1.9) is ill-posed if the dimension of the measurement vector $\mathbf{y}$ is smaller than the dimension of the true signal $\mathbf{f}^*$. Therefore, various penalization schemes are usually incorporated to pose the problem better as we explain in Section 1.1.1. The regularized Poisson intensity reconstruction problem has the following constrained optimization form:

$$\begin{aligned} \hat{\mathbf{f}} \quad &= \quad \underset{\mathbf{f} \in \mathbb{R}^n}{\arg\min} \quad F(\mathbf{f}) + \tau \, \mathrm{pen}(\mathbf{f}) \\ &\qquad \text{subject to} \quad \mathbf{f} \succeq 0, \end{aligned} \tag{1.10}$$

where $\tau > 0$ is the regularization parameter, and pen: $\mathbb{R}^n \longrightarrow \mathbb{R}$ is an usually nonsmooth and potentially nonconvex penalty functional (see e.g., [56]).

1.2 Contribution of the Dissertation

In this dissertation, we explicitly model noise using Poisson or Gaussian statistics for low-dimensional measurements and further enforce sparsity and structure in the solution using nonconvex sparsity promoting regularizers. We developed the following novel optimization methods for solving sparse recovery problems arising in medical imaging, signal/image processing, and computational genomics:

(1) SPIRAL-ℓ_p is a method for minimizing the negative Poisson log-likelihood with nonconvex ℓ_p-norm regularization ($0 \leq p < 1$) to infer sparse signals from low-count measurements. We have analyzed zero-finding methods for

solving the ℓ_p-norm regularized minimization subproblems arising from a sequential quadratic approach. We have also provided a local convergence proof for the nonconvex method under mild conditions. To the best of my knowledge, this is the first method to bridge the gap between convex ℓ_1-norm and ℓ_0 counting seminorm in Poisson noise context. We applied this method to solve a 3D fluorescence molecular tomography problem in collaboration with the Li Lab in Bioengineering at UC Merced.

(2) SPIRAL-TV$_p$ is an algorithm to recover image from photon-limited observations when the image is not sparse. This nonconvex p-th power total variation (TV) regularization problem is solved in a convex setting by using a reweighting strategy for each iteration. We have shown that the proposed algorithm converges to a reasonably good local solution that is more accurate than the existing TV$_1$ global solution.

(3) SPIRAL-Shannon, a sparsity promoting algorithm in which we propose to regularize the Poisson log-likelihood by the *generalized* nonconvex Shannon entropy function. In particular, this non-separable Shannon regularization function is approximated using its first-order Taylor series. We explore the effectiveness and efficiency of the proposed method using numerical experiments. Unlike previous nonconvex methods, the proposed method achieved comparable results with less computational effort.

(4) Bounded-SPIRAL-ℓ_1 is a method for minimizing the negative Poisson log-likelihood where upper and lower bounds on the true signal are known *a priori*. This method incorporates additional information beyond sparsity, such as signal support and maximal signal intensity, to improve signal reconstruction. We applied this method to deblur Quick Response (QR) codes and phantoms from medical imaging under low-light conditions.

(5) We designed and implemented stage-based methods to solve time-dependent bioluminescence tomography and fluorescence lifetime imaging problems. Our approach is different in the following manner: (a) We incorporate a nonconvex ℓ_p-norm regularization to promote further sparsity and highlight

different structural properties of the solution, (b) we explicitly model CCD camera measurements using Poisson noise model, and (c) we recover the support of the signal using the time-averaged data and reconstruct the signal intensity and lifetime using the time-dependent data. We demonstrate the effectiveness of the proposed stage-based methods through numerical experiments in 2D imaging.

(6) TrustSpa-ℓ_1 and TrustSpa-ℓ_p ($0 < p < 1$) are two limited-memory trust-region methods for minimizing a least-squares fidelity term with a convex and nonconvex regularization penalties, respectively. Our approach is novel in the transformation of the sparse recovery problem to a differentiable unconstrained minimization problem and in the use of eigenvalues for efficiently solving the trust-region subproblem. Unlike gradient projection-type methods, which use only the current gradient, our approach uses gradients from previous iterations to obtain a more accurate Hessian approximation. Numerical experiments show that our proposed approach eliminates spurious solutions more effectively while improving the computational time to converge.

In addition, I have collaborated on sparse signal recovery methods for next-generation DNA sequence data with the Sindi Lab at UC Merced. Most of this work involves developing novel computational methods to predict structural variants, which are rearrangements of an individual's genome. Furthermore, as a result of another collaborative work with Dr. Fei Wen from Shanghai Jiao Tong University, I proposed to employ the ℓ_p-norm ($0 \leq p < 1$) regularization for demixing problems in signal and image processing.

1.3 Organization of the Dissertation

Generally, this dissertation is divided into two parts: The first part of the dissertation (i.e., Chapter 2 and 3) will discuss nonconvex sparse Poisson intensity reconstruction methods with their applications and the second part (i.e., Chapter

4) is concerned with nonconvex sparse recovery methods with Gaussian noise. Chapters in this dissertation are organized as follows:

Chapter 2: Photon-Limited Imaging

In this chapter, We propose four novel optimization methods for sparse signal recovery under low-light conditions: (1) A bounded photon-limited image recovery algorithm, (2) a non-convex ℓ_p-norm regularization method (SPIRAL-ℓ_p) with an analysis for the subproblem minimization. We are also able to provide local convergence guarantees under mild conditions for SPIRAL-ℓ_p, (3) a non-convex p-th power total variation regularization method, (4) a non-convex Shannon entropy regularization method for efficient sparse recovery from photon-limited observations.

Chapter 3: Applications with Poisson Process Model

In this chapter, We concern on demonstrating the effectiveness of proposed Poisson sparse recovery algorithms in Chapter 2 with real world applications. First, we investigate the effectiveness of our ℓ_p-norm regularized method in solving the fluorescence molecular tomography problem with low photon counts. Second, we propose two novel stage-based methods to solve tomography problems in functional imaging: A two-stage method for bioluminescence tomography and three-stage method for fluorescence lifetime imaging problem in low photon context. Lastly, we will discuss my contribution on structural variants detection algorithms in computational genomics with the Sindi Lab.

Chapter 4: Sparse Recovery Methods with Gaussian Noise

This chapter focuses on sparse recovery methods and their applications under Gaussian noise. First, we propose two novel methods (using convex regularization and nonconvex regularization) to solve the ℓ_2-ℓ_1 problem by transforming its objective function into an unconstrained differentiable function and apply a limited-memory trust-region method. After that, we will briefly discuss a collab-

orative work with Dr. Fei Wen on sparse recovery and demixing signals with an image inpainting example.

Chapter 5: Conclusion

Finally, this chapter concludes the dissertation and suggests several new avenues in photon-limited imaging for future research.

Chapter 2

Photon-Limited Imaging

Reconstructing high-dimensional sparse signals from low-dimensional low-count photon observation is a challenging nonlinear optimization problem. In low photon context, the arrival of photons at the detector is typically modeled by the inhomogeneous Poisson process (1.7). In this chapter, we propose three algorithms to minimize the Poisson log-likelihood function using three nonconvex sparsity-promoting regularizers: (1) ℓ_p-norm ($0 \leq p < 1$), (2) p-th power ($0 \leq p < 1$) total variation, and (3) generalized Shannon entropy, for accurate sparse signal recovery. In addition, I will discuss a bounded photon-limited image recovery algorithm where maximum and minimum amplitudes at specific regions of an image are known *a priori.*

2.1 Prior Work

According to the literature, inverse problems with Poisson data has garnered significant attention by applied mathematicians and statisticians in many applications including medicine, engineering and astronomy (see e.g., [118, 67, 20, 30, 73]). A Poisson intensity reconstruction algorithm to solve the Poisson problem in (1.10) has been investigated in several works using different techniques. In particular, Fessler proposed a algorithm in [57] based on finding paraboloidal surrogate functions for the log-likelihood at each iteration and maximized these surrogate functions using existing algorithms such as coordinate ascent. In [97] and [96], Nowak

and Kolaczyk introduced a Bayesian multiscale framework with the expectation-maximization algorithm for linear inverse problems involving Poisson data. Other recent effort [58] known as the alternating direction method of multipliers (ADMM) solved the problem of restoring Poissonian images based on an alternating direction optimization method. The main hurdle of the ADMM method is that it requires to solve a linear system at each iteration with a matrix inverse operation. In [77], Jansen proposed a wavelet-based Poisson estimation method, which leads to inaccurate solutions when the observed number of photons per pixel is very low. In our research, we consider the recent Sparse Poisson Intensity Reconstruction ALgorithm (SPIRAL) [70], which is a flexible framework to solve the Poisson inverse problem with state-of-the-art performance by modifying the penalty term.

2.1.1 Sparse Poisson Intensity Reconstruction ALgorithm (SPIRAL)

In SPIRAL [70], we approximate the negative Poisson log-likelihood function $F(\mathbf{f})$ in (1.9) with a sequence of quadratic subproblems. Each iterate is obtained from the previous iterate by solving

$$
\begin{aligned}
\mathbf{f}^{k+1} \quad = \quad & \underset{\mathbf{f}\in\mathbb{R}^n}{\arg\min} \quad F^k(\mathbf{f}) + \tau\,\mathrm{pen}(\mathbf{f}), \\
& \text{subject to} \quad \mathbf{f} \succeq 0,
\end{aligned}
$$

where $F^k(\mathbf{f})$ denotes the second order Taylor series approximation to the $F(\mathbf{f})$ at $\mathbf{f}^k$:

$$
F^k(\mathbf{f}) \approx F(\mathbf{f}^k) + (\mathbf{f} - \mathbf{f}^k)^T \nabla F(\mathbf{f}^k) + \frac{1}{2}(\mathbf{f} - \mathbf{f}^k)^T \nabla^2 F(\mathbf{f}^k)(\mathbf{f} - \mathbf{f}^k). \tag{2.1}
$$

Then the Hessian $\nabla^2 F(\mathbf{f}^k)$ in (2.1) is approximated by a scaled identity matrix $\alpha_k \mathbf{I}$, with $\alpha_k > 0$ [134]. This yields

$$
F^k(\mathbf{f}) \approx F(\mathbf{f}^k) + (\mathbf{f} - \mathbf{f}^k)^T \nabla F(\mathbf{f}^k) + \frac{\alpha_k}{2} \parallel \mathbf{f} - \mathbf{f}^k \parallel_2^2, \tag{2.2}
$$

where α_k is chosen by a modified Barzilai-Borwein (BB) method [23] as

$$
\alpha_k \quad = \quad \frac{\left\| \sqrt{\mathbf{y}} \cdot (\mathbf{A}\delta^k)/(\mathbf{A}\mathbf{f}^k + \beta\,\mathbf{1}) \right\|_2^2}{\parallel \delta^k \parallel_2^2},
$$

where $\delta^k = \mathbf{f}^k - \mathbf{f}^{k-1}$ and $\sqrt{\cdot}, \cdot, /$ are component-wise operators. As described in the Appendix A.2, simplifying the second-order approximation in (2.2) yields a sequence of subproblems of the form

$$
\begin{aligned}
\mathbf{f}^{k+1} \;\; = \;\; & \underset{\mathbf{f} \in \mathbb{R}^n}{\arg\min} \;\; \frac{1}{2} \parallel \mathbf{f} - \mathbf{s}^k \parallel_2^2 \; + \frac{\tau}{\alpha_k} \operatorname{pen}(\mathbf{f}) \\
& \text{subject to} \quad \mathbf{f} \succeq 0,
\end{aligned}
\tag{2.3}
$$

where

$$
\mathbf{s}^k = \mathbf{f}^k - \frac{1}{\alpha_k} \nabla F(\mathbf{f}^k).
$$

In SPIRAL, the Poisson intensity reconstruction was achieved by replacing the penalty function $\operatorname{pen}(\mathbf{f})$ in (2.3) by a variety of convex penalty terms such as ℓ_1-norm, ℓ_1-norm with noncanonical basis, and *total variation* (TV) seminorm. In our research, we introduce nonconvex penalty functionals to SPIRAL to promote sparse solutions with more accuracy.

2.2 Bounded Sparse Photon-Limited Image Recovery

The work describes in this section is based on the paper by Adhikari and Marcia [6]. Photon-limited recovery methods typically incorporate sparsity and nonnegativity through constraints and penalizers (see e.g., [57, 58, 70]). In addition to sparsity and nonnegativity, other information about the true signal may be known in practice. In particular, its maximum and minimum amplitudes at specific regions might be known *a priori.* In medical imaging, structural information such as tissue geometries are used to improve the accuracy of tomography. For example, in near infrared diffuse optical tomography, structural priors from magnetic resonance imaging are incorporated to limit smoothing across their shared boundaries and adjust the image smoothness [135, 136, 33]. These structural priors can be expressed as bounds on the signal intensity, and as such, they can be incorporated into the photon-limited image recovery problem to enhance the quality of the reconstruction. Here, we describe an optimization method (based on the SPIRAL approach [70]) that includes upper and lower bound constraints that model

additional signal intensity information. We demonstrate the effectiveness of the proposed approach on two different low-light deblurring examples.

Problem Formulation

When the maximum and minimum signal intensity information is known, the sparsity-promoting Poisson intensity reconstruction problem has the following constrained minimization form:

$$\hat{\mathbf{f}} = \underset{\mathbf{f} \in \mathbb{R}^n}{\arg\min} \quad F(\mathbf{f}) + \tau \|\mathbf{f}\|_1$$
$$\text{subject to } \mathbf{b_L} \preceq \mathbf{f} \preceq \mathbf{b_U},$$

where $F(\mathbf{f})$ is the negative Poisson log-likelihood function (1.9), $\tau > 0$ is the regularization parameter, and $\mathbf{b_L}$ and $\mathbf{b_U}$ are the lower and upper bounds on signal $\mathbf{f}$, respectively (note these bounds take the dimension as the signal/image). Based on the SPIRAL framework [70], our subproblems are of the form

$$\mathbf{f}^{k+1} = \underset{\mathbf{f} \in \mathbb{R}^n}{\arg\min} \quad \frac{1}{2} \| \mathbf{f} - \mathbf{s}^k \|_2^2 + \frac{\tau}{\alpha_k} \|\mathbf{f}\|_1$$
$$\text{subject to} \quad \mathbf{b_L} \preceq \mathbf{f} \preceq \mathbf{b_U},$$

where $\mathbf{s}^k = \mathbf{f}^k - \frac{1}{\alpha_k} \nabla F(\mathbf{f}^k)$. If the signal of interest is sparse in some orthonormal basis $\mathbf{W}$, then the penalty term $\|\mathbf{f}\|_1$ is replaced by $\|\boldsymbol{\theta}\|_1$, where $\boldsymbol{\theta} = \mathbf{W}^T\mathbf{f}$. Then the minimization subproblem becomes

$$\boldsymbol{\theta}^{k+1} = \underset{\boldsymbol{\theta} \in \mathbb{R}^n}{\arg\min} \quad \phi^k(\boldsymbol{\theta}) = \frac{1}{2}\|\boldsymbol{\theta} - \mathbf{s}^k\|_2^2 + \frac{\tau}{\alpha_k}\|\boldsymbol{\theta}\|_1,$$
$$\text{subject to } \mathbf{b_L} \preceq \mathbf{W}\theta \preceq \mathbf{b_U}. \tag{2.4}$$

We note that typically, $\mathbf{b_L} = \mathbf{0}$, but we do not make that assumption here. We can solve this minimization problem by solving its Lagrangian dual. The discussion below follows [70] very closely. Our main contribution is the extension of the constraints to general bounds and the inclusion of a convergence proof for the subproblem minimization.

First, we introduce $\mathbf{u}, \mathbf{v} \in \mathbb{R}^n$ with $\mathbf{u}, \mathbf{v} \succeq 0$ and write $\boldsymbol{\theta} = \mathbf{u} - \mathbf{v}$ so that $\phi^k(\boldsymbol{\theta})$

in (2.4) is differentiable [58, 70]:

$$(\mathbf{u}^{k+1}, \mathbf{v}^{k+1}) = \arg\min_{\mathbf{u}, \mathbf{v} \in \mathbb{R}^n} \quad \frac{1}{2}\|\mathbf{u} - \mathbf{v} - \mathbf{s}^k\|_2^2 + \frac{\tau}{\alpha_k}\mathbf{1}^T(\mathbf{u} + \mathbf{v})$$

$$\text{subject to} \quad \mathbf{u}, \mathbf{v} \succeq 0, \ \mathbf{b_L} \preceq \mathbf{W}(\mathbf{u} - \mathbf{v}) \preceq \mathbf{b_U}. \qquad (2.5)$$

Note, however, that the new problem now has twice as many parameters and has additional nonnegativity constraints on the new parameters. The last constraints can be expressed as $\mathbf{W}(\mathbf{u} - \mathbf{v}) - \mathbf{b_L} \succeq 0$ and $\mathbf{b_U} - \mathbf{W}(\mathbf{u} - \mathbf{v}) \succeq 0$. The Lagrangian function corresponding to (2.5) is given by

$$\begin{aligned}
\mathscr{L}(\mathbf{u}, \mathbf{v}, \boldsymbol{\lambda}_1, \boldsymbol{\lambda}_2, \boldsymbol{\lambda}_3, \boldsymbol{\lambda}_4) &= \frac{1}{2}\|\mathbf{u} - \mathbf{v} - \mathbf{s}^k\|_2^2 + \frac{\tau}{\alpha_k}\mathbf{1}^T(\mathbf{u} + \mathbf{v}) - \boldsymbol{\lambda}_1^T\mathbf{u} - \boldsymbol{\lambda}_2^T\mathbf{v} \\
&\quad - \boldsymbol{\lambda}_3^T(\mathbf{W}(\mathbf{u} - \mathbf{v}) - \mathbf{b_L}) - \boldsymbol{\lambda}_4^T(\mathbf{b_U} - \mathbf{W}(\mathbf{u} - \mathbf{v})),
\end{aligned}$$

where $\boldsymbol{\lambda}_1, \boldsymbol{\lambda}_2, \boldsymbol{\lambda}_3, \boldsymbol{\lambda}_4 \in \mathbb{R}^n$ are the Lagrange multipliers corresponding to the constraints in (2.5). Differentiating $\mathscr{L}$ with respect to $\mathbf{u}$ and $\mathbf{v}$ and setting the derivatives to zero yields

$$\mathbf{u} - \mathbf{v} = \mathbf{s}^k + \boldsymbol{\lambda}_1 - \frac{\tau}{\alpha_k}\mathbf{1} + \mathbf{W}^T\boldsymbol{\lambda}_3 - \mathbf{W}^T\boldsymbol{\lambda}_4, \ \text{and} \qquad (2.6)$$

$$\boldsymbol{\lambda}_2 = \frac{2\tau}{\alpha_k}\mathbf{1} - \boldsymbol{\lambda}_1.$$

Then it follows that $\frac{\tau}{\alpha_k}\mathbf{1}^T(\mathbf{u} + \mathbf{v}) - \boldsymbol{\lambda}_1^T\mathbf{u} - \boldsymbol{\lambda}_2^T\mathbf{v} = \frac{\tau}{\alpha_k}\mathbf{1}^T(\mathbf{u} - \mathbf{v}) - \boldsymbol{\lambda}_1^T(\mathbf{u} - \mathbf{v})$ in $\mathscr{L}$. Therefore

$$\begin{aligned}
\mathscr{L}(\mathbf{u}, \mathbf{v}, \boldsymbol{\lambda}_1, \boldsymbol{\lambda}_2, \boldsymbol{\lambda}_3, \boldsymbol{\lambda}_4) &= \frac{1}{2}\|\mathbf{u} - \mathbf{v}\|_2^2 + \frac{1}{2}\|\mathbf{s}^k\|_2^2 \\
&\quad -(\mathbf{u} - \mathbf{v})^T(\mathbf{s}^k + \boldsymbol{\lambda}_1 - \frac{\tau}{\alpha_k}\mathbf{1} + \mathbf{W}^T\boldsymbol{\lambda}_3 - \mathbf{W}^T\boldsymbol{\lambda}_4) \\
&\quad + \boldsymbol{\lambda}_3^T\mathbf{b_L} - \boldsymbol{\lambda}_4^T\mathbf{b_U}.
\end{aligned}$$

Substituting $\mathbf{u} - \mathbf{v}$ from (2.6) in $\mathscr{L}$, we obtain the Lagrangian dual function independent of the primal variables, $\mathbf{u}$ and $\mathbf{v}$:

$$\begin{aligned}
g(\boldsymbol{\lambda}_1, \boldsymbol{\lambda}_3, \boldsymbol{\lambda}_4) &= -\frac{1}{2}\|\mathbf{s}^k + \boldsymbol{\lambda}_1 - \frac{\tau}{\alpha_k}\mathbf{1} + \mathbf{W}^T(\boldsymbol{\lambda}_3 - \boldsymbol{\lambda}_4)\|_2^2 \\
&\quad + \boldsymbol{\lambda}_3^T\mathbf{b_L} - \boldsymbol{\lambda}_4^T\mathbf{b_U} + \frac{1}{2}\|\mathbf{s}^k\|_2^2.
\end{aligned}$$

Next, let $\boldsymbol{\gamma} = \boldsymbol{\lambda}_1 - \frac{\tau}{\alpha_k}\mathbf{1}$. For the Lagrange dual problem corresponding to (2.5), the Lagrange multipliers $\boldsymbol{\lambda}_i \succeq 0$ for $i \in \{1, 2, 3, 4\}$. Since

$$0 \ \preceq \ \boldsymbol{\lambda}_2 = \frac{2\tau}{\alpha_k}\mathbf{1} - \boldsymbol{\lambda}_1 = \frac{\tau}{\alpha_k}\mathbf{1} - \boldsymbol{\gamma} \ \text{and}$$

$$0 \ \preceq \ \boldsymbol{\lambda}_1 = \boldsymbol{\gamma} + \frac{\tau}{\alpha_k}\mathbf{1},$$

then $\boldsymbol{\gamma}$ satisfies $-\frac{\tau}{\alpha_k}\mathbf{1} \preceq \boldsymbol{\gamma} \preceq \frac{\tau}{\alpha_k}\mathbf{1}$. The Lagrange dual problem associated with (2.5) is thus given by

$$
\begin{aligned}
\underset{\boldsymbol{\gamma},\boldsymbol{\lambda}_3,\boldsymbol{\lambda}_4\in\mathbb{R}^n}{\text{minimize}} \ h(\boldsymbol{\gamma},\boldsymbol{\lambda}_3,\boldsymbol{\lambda}_4) = {}& \tfrac{1}{2}\|\mathbf{s}^k + \boldsymbol{\gamma} + \mathbf{W}^T(\boldsymbol{\lambda}_3 - \boldsymbol{\lambda}_4)\|_2^2 \\
& - \boldsymbol{\lambda}_3^T\mathbf{b_L} + \boldsymbol{\lambda}_4^T\mathbf{b_U} - \tfrac{1}{2}\|\mathbf{s}^k\|_2^2
\end{aligned}
$$

$$
\text{subject to} \ \ \boldsymbol{\lambda}_3, \boldsymbol{\lambda}_4 \succeq 0, \ \ -\tfrac{\tau}{\alpha_k}\mathbf{1} \preceq \boldsymbol{\gamma} \preceq \tfrac{\tau}{\alpha_k}\mathbf{1}. \tag{2.7}
$$

At the dual optimal values $\boldsymbol{\gamma}^\star$, $\boldsymbol{\lambda}_3^\star$, and $\boldsymbol{\lambda}_4^\star$, the primal iterate $\boldsymbol{\theta}^{k+1}$ is given by

$$
\boldsymbol{\theta}^{k+1} = \mathbf{u}^{k+1} - \mathbf{v}^{k+1} = \mathbf{s}^k + \boldsymbol{\gamma}^\star + \mathbf{W}^T(\boldsymbol{\lambda}_3^\star - \boldsymbol{\lambda}_4^\star).
$$

We note that the duality gap for (2.5) and its dual (2.7) is zero, i.e., $\phi^k(\boldsymbol{\theta}^{k+1}) = -h(\boldsymbol{\gamma}^\star,\boldsymbol{\lambda}_3^\star,\boldsymbol{\lambda}_4^\star)$ because (2.5) satisfies (a weakened) Slater's condition [32]. In addition, the function $-h(\boldsymbol{\gamma},\boldsymbol{\lambda}_3,\boldsymbol{\lambda}_4)$ is a lower bound on $\phi^k(\boldsymbol{\theta})$ at any dual feasible point. We note that the objective function $h(\boldsymbol{\gamma},\boldsymbol{\lambda}_3,\boldsymbol{\lambda}_4)$ can be written as

$$
\begin{aligned}
h(\boldsymbol{\gamma},\boldsymbol{\lambda}_3,\boldsymbol{\lambda}_4) \ = \ & \{\tfrac{1}{2}\|\boldsymbol{\gamma}\|_2^2 + \boldsymbol{\gamma}^T\mathbf{s}^k\} + \boldsymbol{\gamma}^T W^T(\boldsymbol{\lambda}_3 - \boldsymbol{\lambda}_4) + \\
& \{\tfrac{1}{2}\|\boldsymbol{\lambda}_3 - \boldsymbol{\lambda}_4\|_2^2 + (\boldsymbol{\lambda}_3 - \boldsymbol{\lambda}_4)^T W\mathbf{s}^k - \boldsymbol{\lambda}_3^T\mathbf{b_L} + \boldsymbol{\lambda}_4^T\mathbf{b_U}\}.
\end{aligned}
$$

We minimize the objective function $h(\boldsymbol{\gamma},\boldsymbol{\lambda}_3,\boldsymbol{\lambda}_4)$ by solving for $\boldsymbol{\gamma}$, $\boldsymbol{\lambda}_3$, and $\boldsymbol{\lambda}_4$ alternatingly, which is done by taking the partial derivatives of $h(\boldsymbol{\gamma},\boldsymbol{\lambda}_3,\boldsymbol{\lambda}_4)$ and setting them to zero. Each component is then constrained to satisfy the bounds in (2.7). We now describe each step more explicitly.

Step 1. Given $\boldsymbol{\lambda}_3^{(j-1)}$ and $\boldsymbol{\lambda}_4^{(j-1)}$ from the previous iterate, solve

$$
\begin{aligned}
\boldsymbol{\gamma}^{(j)} = \ \underset{\boldsymbol{\gamma}\in\mathbb{R}^n}{\arg\min} \ \ & \tfrac{1}{2}\|\boldsymbol{\gamma}\|_2^2 + \boldsymbol{\gamma}^T\mathbf{s}^k + \boldsymbol{\gamma}^T W^T(\boldsymbol{\lambda}_3^{(j-1)} - \boldsymbol{\lambda}_4^{(j-1)}) \\
& \text{subject to} \ -\tfrac{\tau}{\alpha_k}\mathbf{1} \preceq \boldsymbol{\gamma} \preceq \tfrac{\tau}{\alpha_k}\mathbf{1}.
\end{aligned} \tag{2.8}
$$

The solution to (2.8) is obtained via thresholding:

$$
\boldsymbol{\gamma}^{(j)} = \text{mid}\Big\{-\tfrac{\tau}{\alpha_k}\mathbf{1}, -\mathbf{s}^k - \mathbf{W}^T\Big(\boldsymbol{\lambda}_3^{(j-1)} - \boldsymbol{\lambda}_4^{(j-1)}\Big), \tfrac{\tau}{\alpha_k}\mathbf{1}\Big\}, \tag{2.9}
$$

where the operator $\text{mid}\{\mathbf{a},\mathbf{b},\mathbf{c}\}$ chooses the middle value of the three arguments component-wise.

Step 2. Given $\boldsymbol{\gamma}^{(j)}$, solve

$$
\begin{aligned}
(\boldsymbol{\lambda}_3^{(j)}, \boldsymbol{\lambda}_4^{(j)}) = \underset{\boldsymbol{\lambda}_3, \boldsymbol{\lambda}_4 \in \mathbb{R}^n}{\arg\min} \quad & \mathcal{L}(\boldsymbol{\lambda}_3, \boldsymbol{\lambda}_4) \equiv \tfrac{1}{2}\|\boldsymbol{\lambda}_3 - \boldsymbol{\lambda}_4\|_2^2 \\
& + \boldsymbol{\lambda}_3^T\big(\mathbf{W}(\mathbf{s}^k + \boldsymbol{\gamma}^{(j)}) - \mathbf{b_L}\big) \\
& + \boldsymbol{\lambda}_4^T\big(\mathbf{b_U} - \mathbf{W}(\mathbf{s}^k + \boldsymbol{\gamma}^{(j)})\big)
\end{aligned}
$$

$$\text{subject to} \quad \boldsymbol{\lambda}_3, \boldsymbol{\lambda}_4 \succeq 0. \tag{2.10}$$

The minimization problem (2.10) has the following solution. Noting $\frac{1}{2}\|\boldsymbol{\lambda}_3 - \boldsymbol{\lambda}_4\|_2^2 = \frac{1}{2}\|\boldsymbol{\lambda}_3\|_2^2 - \boldsymbol{\lambda}_3^T\boldsymbol{\lambda}_4 + \frac{1}{2}\|\boldsymbol{\lambda}_4\|_2^2$, and letting $\boldsymbol{r_L}^{(j)} = \mathbf{W}(\mathbf{s}^k + \boldsymbol{\gamma}^{(j)}) - \mathbf{b_L}$ and $\boldsymbol{r_U}^{(j)} = \mathbf{b_U} - \mathbf{W}(\mathbf{s}^k + \boldsymbol{\gamma}^{(j)})$, then (2.10) can be written as

$$
\begin{aligned}
(\boldsymbol{\lambda}_3^{(j)}, \boldsymbol{\lambda}_4^{(j)}) = \underset{\boldsymbol{\lambda}_3, \boldsymbol{\lambda}_4 \in \mathbb{R}^n}{\arg\min} \quad & \tfrac{1}{2}\|\boldsymbol{\lambda}_3\|_2^2 + \boldsymbol{\lambda}_3^T\boldsymbol{r_L}^{(j)} - \boldsymbol{\lambda}_3^T\boldsymbol{\lambda}_4 \\
& + \tfrac{1}{2}\|\boldsymbol{\lambda}_4\|_2^2 + \boldsymbol{\lambda}_4^T\boldsymbol{r_U}^{(j)}
\end{aligned}
$$

$$\text{subject to} \quad \boldsymbol{\lambda}_3, \boldsymbol{\lambda}_4 \succeq 0. \tag{2.11}$$

Note that if $\boldsymbol{r_L}^{(j)} \succeq 0$ and $\boldsymbol{r_U}^{(j)} \succeq 0$, i.e., $\mathbf{b_L} \preceq \mathbf{W}(\mathbf{s}^k + \boldsymbol{\gamma}^{(j)}) \preceq \mathbf{b_U}$, then $\mathcal{L}(\boldsymbol{\lambda}_3, \boldsymbol{\lambda}_4) \succeq 0$ for $\boldsymbol{\lambda}_3, \boldsymbol{\lambda}_4 \succeq 0$, and is therefore minimized at $\boldsymbol{\lambda}_3 = \boldsymbol{\lambda}_4 = 0$. We now assume otherwise. Computing the gradient of $\mathcal{L}(\boldsymbol{\lambda}_3, \boldsymbol{\lambda}_4)$ with respect to $\boldsymbol{\lambda}_3$ and $\boldsymbol{\lambda}_4$ yields

$$\nabla_{\boldsymbol{\lambda}_3}\mathcal{L}(\boldsymbol{\lambda}_3, \boldsymbol{\lambda}_4) = \boldsymbol{\lambda}_3 + \boldsymbol{r_L}^{(j)} - \boldsymbol{\lambda}_4$$

and

$$\nabla_{\boldsymbol{\lambda}_4}\mathcal{L}(\boldsymbol{\lambda}_3, \boldsymbol{\lambda}_4) = \boldsymbol{\lambda}_4 + \boldsymbol{r_U}^{(j)} - \boldsymbol{\lambda}_3.$$

For each i, unless $(\mathbf{b_L})_i = (\mathbf{b_U})_i$, both $(\nabla_{\boldsymbol{\lambda}_3}\mathcal{L})_i$ and $(\nabla_{\boldsymbol{\lambda}_4}\mathcal{L})_i$ cannot be simultaneously 0 (since this implies $(\boldsymbol{r_L}^{(j)})_i + (\boldsymbol{r_U}^{(j)})_i = 0$, or equivalently, $(\mathbf{b_U})_i - (\mathbf{b_L})_i = 0$). Therefore, the components of the gradient of the minimizer must be 0 or the corresponding components of the minimizer must lie on the boundary, i.e., $(\nabla_{\boldsymbol{\lambda}_3}\mathcal{L})_i = 0$ and $(\boldsymbol{\lambda}_4)_i = 0$, or $(\boldsymbol{\lambda}_3)_i = 0$ and $(\nabla_{\boldsymbol{\lambda}_4}\mathcal{L})_i = 0$. These conditions define the values of the solutions $\boldsymbol{\lambda}_3^{(j)}$ and $\boldsymbol{\lambda}_4^{(j)}$:

$$
\begin{aligned}
\boldsymbol{\lambda}_3^{(j)} &= [-\boldsymbol{r_L}^{(j)}]_+ = [-\mathbf{W}(s^k + \boldsymbol{\gamma}^{(j)}) + \mathbf{b_L}]_+ \\
\boldsymbol{\lambda}_4^{(j)} &= [-\boldsymbol{r_U}^{(j)}]_+ = [\ \mathbf{W}(s^k + \boldsymbol{\gamma}^{(j)}) - \mathbf{b_U}]_+.
\end{aligned}
$$

where the operator $[\,\cdot\,]_+ = \max\{\,\cdot\,, \mathbf{0}\}$ component-wise.

Convergence. We prove the convergence of this alternating minimization strategy from techniques found in [25]. Let

$$
\begin{aligned}
\psi(\boldsymbol{\gamma}, \boldsymbol{\lambda}_3, \boldsymbol{\lambda}_4) &= \boldsymbol{\gamma}^T \mathbf{W}^T (\boldsymbol{\lambda}_3 - \boldsymbol{\lambda}_4) \\
g_1(\boldsymbol{\gamma}) &= \tfrac{1}{2}\|\boldsymbol{\gamma}\|_2^2 + \boldsymbol{\gamma}^T \mathbf{s}^k \\
g_2(\boldsymbol{\lambda}_3, \boldsymbol{\lambda}_4) &= \tfrac{1}{2}\|\boldsymbol{\lambda}_3 - \boldsymbol{\lambda}_4\|_2^2 + (\boldsymbol{\lambda}_3 - \boldsymbol{\lambda}_4)^T \mathbf{W}\mathbf{s}^k \\
&\quad -\boldsymbol{\lambda}_3^T \mathbf{b_L} + \boldsymbol{\lambda}_4^T \mathbf{b_U}
\end{aligned}
$$

so that $h(\boldsymbol{\gamma}, \boldsymbol{\lambda}_3, \boldsymbol{\lambda}_4) = \psi(\boldsymbol{\gamma}, \boldsymbol{\lambda}_3, \boldsymbol{\lambda}_4) + g_1(\boldsymbol{\gamma}) + g_2(\boldsymbol{\lambda}_3, \boldsymbol{\lambda}_4)$. Note the following: (A) Both functions g_1 and g_2 are continuous functions whose domains are closed. Consequently, they are closed (see Sec. A.3.3 in [32]). (B) ψ is bilinear in $\boldsymbol{\gamma}$ and in $(\boldsymbol{\lambda}_3, \boldsymbol{\lambda}_4)$. Therefore, it is a continuously differentiable convex function. (C) The gradient of ψ with respect to $\boldsymbol{\gamma}$ is constant, and therefore $\nabla_{\boldsymbol{\gamma}}\psi$ is Lipschitz continuous. (D) The gradient of ψ with respect to $(\boldsymbol{\lambda}_3, \boldsymbol{\lambda}_4)$ is constant, and therefore $\nabla_{\boldsymbol{\lambda}_3, \boldsymbol{\lambda}_4}\psi$ is Lipschitz continuous. (E) Since the primal problem (2.4) has a continuous objective function and has a closed and bounded domain, it must have a minimum by the Extreme Value Theorem. Because the duality gap is zero, i.e., $\phi^k(\boldsymbol{\theta}^{k+1}) = -h(\boldsymbol{\gamma}^\star, \boldsymbol{\lambda}_3^\star, \boldsymbol{\lambda}_4^\star)$, the dual problem (2.7) must have a solution. In addition, the subproblems (2.8) and (2.10) have explicit minimizers. With these, the assumptions needed to apply Lemma 3.2 in [25] are satisfied. In particular, we obtain the following convergence result:

Theorem 1: Let $\{(\boldsymbol{\gamma}^{(j)}, \boldsymbol{\lambda}_3^{(j)}, \boldsymbol{\lambda}_4^{(j)})\}_{j\geq 0}$ be the sequence generated by the proposed alternating minimization method. Any accumulation point of $\{(\boldsymbol{\gamma}^{(j)}, \boldsymbol{\lambda}_3^{(j)}, \boldsymbol{\lambda}_4^{(j)})\}$ is a stationary point of problem (2.7).

Feasibility. We now show that at the end of each iteration j, the approximate solution $\boldsymbol{\theta}^{(j)} = \mathbf{s}^k + \boldsymbol{\gamma}^{(j)} + \mathbf{W}^T(\boldsymbol{\lambda}_3^{(j)} - \boldsymbol{\lambda}_4^{(j)})$ to (2.4) is feasible with respect to the constraint $\mathbf{b_L} \preceq \mathbf{W}\theta \preceq \mathbf{b_U}$. First, note that

$$
\begin{aligned}
\mathbf{W}\boldsymbol{\theta}^{(j)} &= \mathbf{W}\mathbf{s}^k + \mathbf{W}\boldsymbol{\gamma}^{(j)} + \boldsymbol{\lambda}_3^{(j)} - \boldsymbol{\lambda}_4^{(j)} \\
&= \mathbf{W}(\mathbf{s}^k + \boldsymbol{\gamma}^{(j)}) + \left[\mathbf{b_L} - \mathbf{W}(\mathbf{s}^k + \boldsymbol{\gamma}^{(j)})\right]_+ \\
&\quad - \left[\mathbf{W}(\mathbf{s}^k + \boldsymbol{\gamma}^{(j)}) - \mathbf{b_U}\right]_+.
\end{aligned}
\tag{2.12}
$$

We note that (2.12) is equivalent to

$$\mathbf{W}\boldsymbol{\theta}^{(j)} = \mathrm{mid}\{\mathbf{b_L}, \mathbf{W}(\mathbf{s}^k + \boldsymbol{\gamma}^{(j)}), \mathbf{b_U}\}.$$

Thus, we can terminate the iterations for the dual problem early and still obtain a feasible point.

Numerical Results

We investigate the effectiveness of the proposed bounded SPIRAL-ℓ_1 (B-SPIRAL-ℓ_1) method by solving two image deblurring problems. In both experiments, the blurry observations are obtained from $\mathbf{A}\mathbf{f}^*$, where the signal $\mathbf{f}^*$ is convolved with a 5×5 blur matrix, whose action is represented by the matrix $\mathbf{A}$. The MATLAB's `poissrnd` function is used to add Poisson noise. Here, we used the Daubechies-2 (DB-2) wavelet basis for $\mathbf{W}$.

We implemented the B-SPIRAL-ℓ_1 algorithm by including constraints to the existing SPIRAL approach [69] to solve subproblem (2.4). The algorithm is initialized using the lower and upper bound information incorporated $\mathbf{A}^T\mathbf{y}$ and terminates if the relative difference between consecutive iterates converged to $\|\mathbf{f}^{k+1} - \mathbf{f}^k\|_2/\|\mathbf{f}^k\|_2 \leq 10^{-6}$. Similar to the SPIRAL approach, we define 30 as the minimum number of iterations to avoid any issues with premature termination. Finally, we compare the results with nonnegatively constrained SPIRAL-ℓ_1 method based on RMSE (%) $= 100 \cdot \|\hat{\mathbf{f}} - \mathbf{f}^*\|_2/\|\mathbf{f}^*\|_2$. The final SPIRAL-$\ell_1$ reconstructions are thresholded using the same bounds used in B-SPIRAL-ℓ_1. The regularization parameters (τ) for both experiments are optimized to get the minimum RMSE value.

QR code deblurring

(a) True image $\mathbf{f}^*$ (b) Observation $\mathbf{y}$ (c) Zoomed region
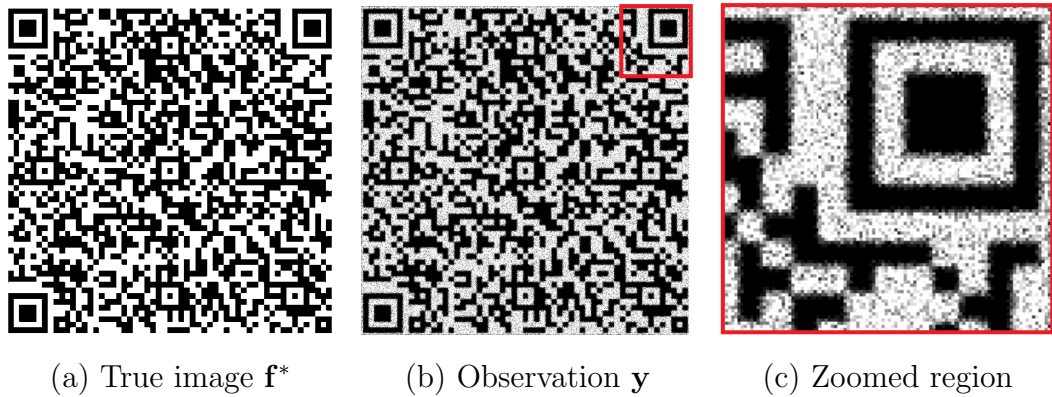
Figure 2.1: Experimental setup: (a) True QR code image $\mathbf{f}^*$, (b) noisy and blurry observation $\mathbf{y}$ with mean photon count 5.7, (c) a zoomed region of $\mathbf{y}$.

In this experiment, we wish to recover a Quick Response (QR) code of size 512×512 (see Fig. 2.1(a)) from the Poisson-noise corrupted blurry image (see Fig. 2.1(b) and the red zoomed region in Fig. 2.1(c)). We set $\mathbf{b_U}$ as the peak intensity of $\mathbf{f}^*$, i.e., $\mathbf{b_U} = 3\mathrm{e}{+}4$, and $\mathbf{b_L}$ as the zero intensity.

The SPIRAL-ℓ_1 method took 16.52 sec (32 iterations) to converge, and its reconstruction $(\hat{\mathbf{f}}_S)$ has RMSE = 18.92%. In contrast, the proposed B-SPIRAL-ℓ_1 method took 25.06 sec (30 iterations) to converge, but its reconstruction $(\hat{\mathbf{f}}_B)$ has RMSE = 16.42%. The B-SPIRAL-ℓ_1 improvements can be best seen in the magnitude of the log error between the true signal $\mathbf{f}^*$ and the reconstructions (see Figs. 2.2(a) and (b)). Note that the $\hat{\mathbf{f}}_B$ reconstruction more closely matches the original signal $\mathbf{f}^*$ than the $\hat{\mathbf{f}}_S$ reconstruction by the prevalence of blue regions in Fig. 2.2(b).
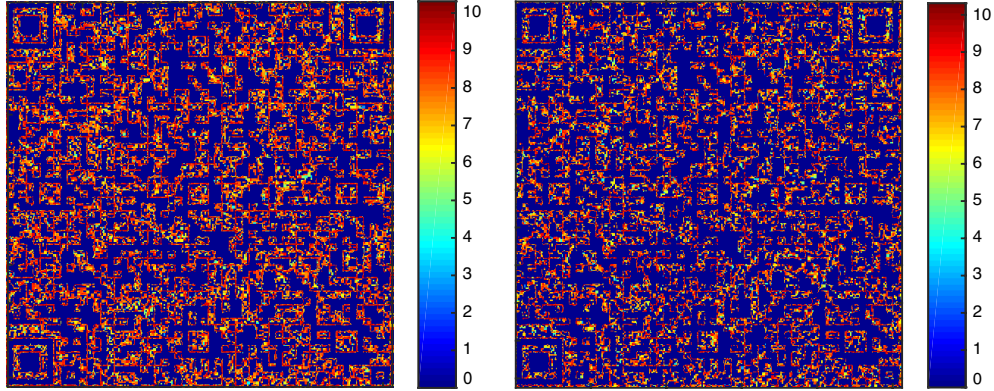
(a) $\log(\mathbf{1} + |\mathbf{f}^* - \hat{\mathbf{f}}_S|)$

(RMSE = 18.92%)

(b) $\log(\mathbf{1} + |\mathbf{f}^* - \hat{\mathbf{f}}_B|)$

(RMSE = 16.42 %)

Figure 2.2:   (a) Log magnitude of error between the true image, $\mathbf{f}^*$, and the SPIRAL-ℓ_1 reconstruction $\hat{\mathbf{f}}_S$, (b) Log magnitude of error between $\mathbf{f}^*$ and the proposed B-SPIRAL-ℓ_1 reconstruction $\hat{\mathbf{f}}_B$. RMSE (%) $= 100 \cdot \|\hat{\mathbf{f}} - \mathbf{f}^*\|_2/\|\mathbf{f}^*\|_2$. Note the lower RMSE for the proposed method's reconstruction, $\hat{\mathbf{f}}_B$, whose log error is closer to zero (represented in blue) than the original method.

Shepp-Logan phantom image deblurring

In the reconstruction of optical images, anatomical information (the tissue shape and/or structure) from x-ray computed tomography (CT) or magnetic resonance imaging (MRI) can be used to improve the spatial resolution [22, 87]. In this experiment, we wish to apply a similar approach to recover the Shepp-Logan phantom image of size 128×128 from the observed image (see Fig. 2.3(a) and (b) respectively), when the tissue outer boundary is known. More specifically, we incorporate that outer boundary as a structural information (see Fig. 2.3(c)), where the lower and upper bound intensities are known based on the region (i.e., 0 and 1e+6 are outside and inside tissue maximum intensities respectively).

For this problem, the SPIRAL-ℓ_1 method took 1.89 sec (39 iterations) to converge, and its reconstruction ($\hat{\mathbf{f}}_S$) has RMSE = 21.57%. The proposed B-SPIRAL-ℓ_1 method took 1.98 sec (30 iterations) to converge, and its reconstruction ($\hat{\mathbf{f}}_B$) has a lower RMSE = 18.85% (see Figs. 2.4(a) and (b)). Note the more accurate reconstruction along the top edges as well as the overall improved accuracy within

the body (represented in yellow) in comparison to the $\hat{\mathbf{f}}_S$ reconstruction.

(a) True image $\mathbf{f}^*$ (b) Observation $\mathbf{y}$ (c) Mask
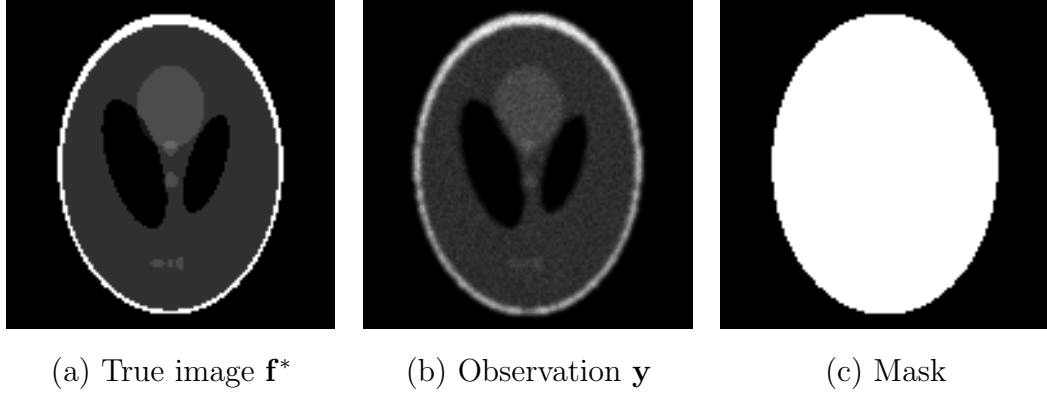
Figure 2.3: Experimental setup: (a) True phantom image $\mathbf{f}^*$, (b) noisy and blurry observation $\mathbf{y}$ with mean photon count 45.8, (c) a mask with prior structural information.

(a) $\log(\mathbf{1} + |\mathbf{f}^* - \hat{\mathbf{f}}_S|)$ (b) $\log(\mathbf{1} + |\mathbf{f}^* - \hat{\mathbf{f}}_B|)$

(RMSE = 21.57%)   (RMSE = 18.85%)
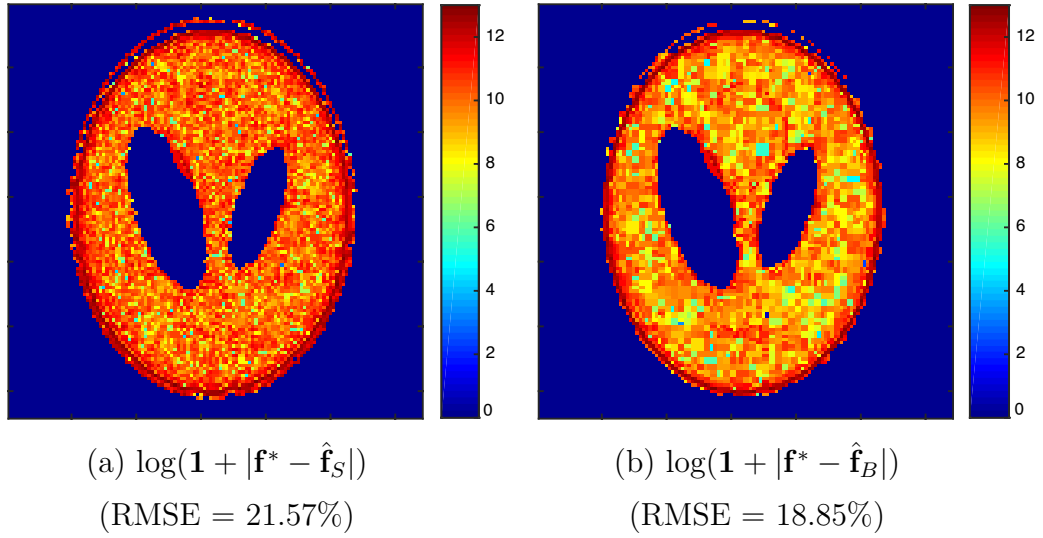
Figure 2.4: (a) Log magnitude of error between the true image, $\mathbf{f}^*$, and $\hat{\mathbf{f}}_S$, and (b) log magnitude of error between $\mathbf{f}^*$ and $\hat{\mathbf{f}}_B$. RMSE (%) $= 100 \cdot \|\hat{\mathbf{f}} - \mathbf{f}^*\|_2 / \|\mathbf{f}^*\|_2$. Note the proposed method's log error is lower on the whole (represented in yellow) in contrast to the mostly orange in (a).

Conclusion

In this method, we formulated a sparsity-promoting bound-constrained photon-limited image recovery method by solving the dual problem based on an alternating minimization strategy. The utilization of any available prior image information has proven very successful for accurately recovering images. We demonstrate that the proposed B-SPIRAL-ℓ_1 method leads to more accurate reconstructions than the simply thresholded solutions from the nonnegatively constrained minimization method.

2.3 Nonconvex Regularization for Photon-Limited Imaging

Reconstructing high-dimensional sparse signals from low-dimensional low-count photon observations is a challenging nonlinear optimization problem. Theoretically, non-convex regularization would lead to more accurate reconstruction than the convex relaxation commonly used in sparse signal recovery. In this Section, we propose to regularize the negative Poisson log-likelihood objective function using three different nonconvex regularizers: ℓ_p-norm, TV_p-norm ($0 \leq p < 1$), and nonconvex Shannon entropy.

2.3.1 Non-convex ℓ_p-norm Regularization

The method describes in this section is based on the paper by Adhikari and Marcia [5]. Here, we consider the recent Sparse Poisson Intensity Reconstruction ALgorithm (SPIRAL) [70], which is a flexible framework to solve the Poisson inverse problem with state-of-the-art performance by modifying the penalty term. Solving the ℓ_0-norm regularized minimization problem is NP-hard and computationally infeasible for high-dimensional problems. The ℓ_1-norm has been shown to be a very good approximation to the ℓ_0-norm in sparse signal recovery [125]. While the SPIRAL method with ℓ_1-norm (SPIRAL-ℓ_1) yielded reasonably good results, its reconstruction contained some spurious artifacts. These artifacts can

be corrected by using a nonconvex ℓ_p penalty term ($p < 1$) while keeping the reconstruction error low (see Fig. 2.5 for comparison between ℓ_1-norm ball and ℓ_p-norm ball in 2D).

$$\text{(a)} \qquad\qquad\qquad\qquad \text{(b)}$$
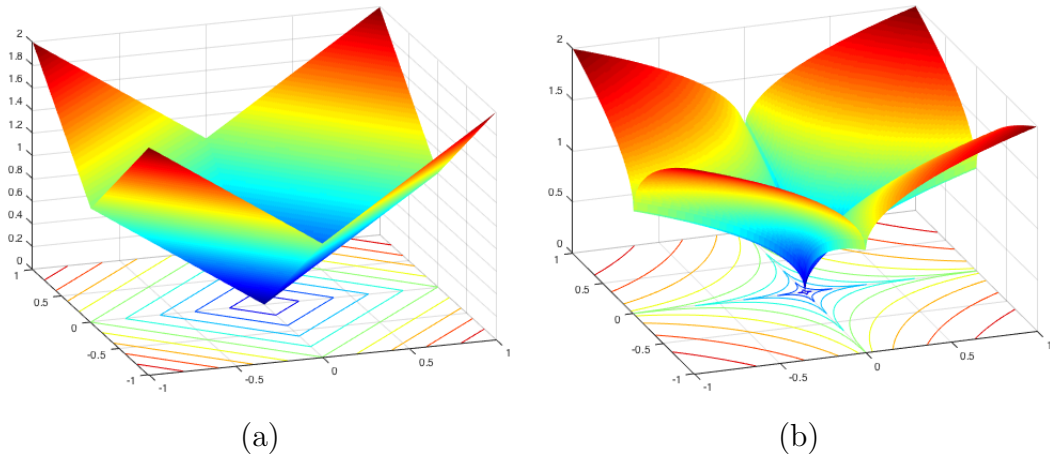
Figure 2.5: (a) The ℓ_1-norm ball with its contour lines in 2D. (b) The ℓ_p-norm ball when $p = 0.5$ with its contour lines in 2D. Note that the ℓ_p-norm ball is nonconvex.

In the proposed method called SPIRAL-ℓ_p ($0 \leq p < 1$), we consider $\text{pen}(\mathbf{f}) = \|\mathbf{f}\|_p^p$ as the penalty term in (1.10). Then the corresponding subproblems in (2.3) can be written as

$$
\begin{aligned}
\mathbf{f}^{k+1} \;=\; &\underset{\mathbf{f} \in \mathbb{R}^n}{\arg\min} \qquad \frac{1}{2} \| \mathbf{f} - \mathbf{s}^k \|_2^2 \;+\; \frac{\tau}{\alpha_k} \; \| \mathbf{f} \|_p^p \\
&\text{subject to} \quad \mathbf{f} \succeq 0.
\end{aligned}
\tag{2.13}
$$

Note that the subproblems (2.13) can be separated into scalar minimization problems of the form

$$
\begin{aligned}
f^* \;=\; &\underset{f \in \mathbb{R}}{\arg\min} \qquad \Omega(f) = \frac{1}{2}(f - s)^2 + \lambda |f|^p \\
&\text{subject to} \quad f \geq 0,
\end{aligned}
\tag{2.14}
$$

where f and s denote elements of the vectors $\mathbf{f}$ and $\mathbf{s}^k$ respectively and $\lambda = \tau/\alpha_k$. Recently, Zuo et al. [148] proposed a simple and efficient iterative algorithm to solve the nonconvex scalar minimization problem in (2.14), which was an extension to the popular soft-thresholding operator [47].

Generalized Soft-Thresholding (GST) Function

As shown in Figure 2.6, for a given regularization parameter $\lambda > 0$ and p-value for $\Omega(f)$ in (2.14), there exists a threshold value $\gamma_p(\lambda)$ (that explicitly depends on p and λ) such that if $s \leq \gamma_p(\lambda)$, the global minimum of (2.14) is $f^* = 0$; otherwise, the global minimum will be a non-zero value. We now show how to compute the threshold value $\gamma_p(\lambda)$ so that we can compute f^*.
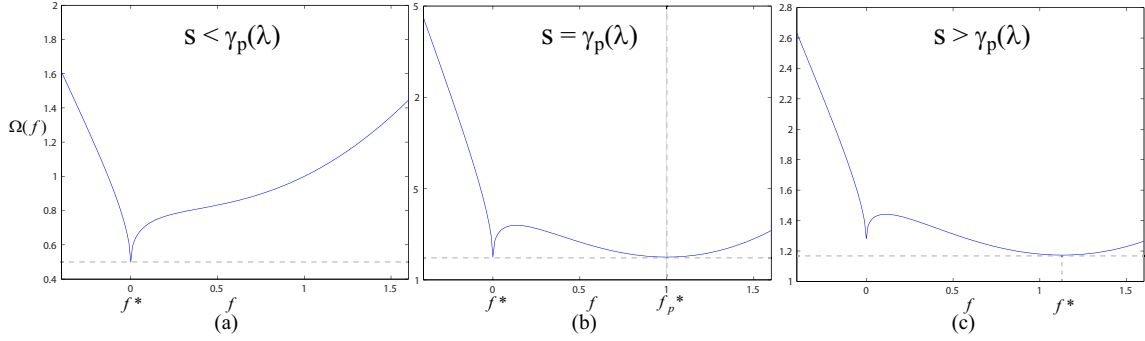
Figure 2.6: The plot of the scalar quadratic function $\Omega(f)$ with p-norm penalty term in (2.14), where $p = 0.5$ and $\lambda = 1.0$. (a) If s is less than the specific threshold value $\gamma_p(\lambda)$, then $f^* = 0$ is the global minimum. (b) If $s = \gamma_p(\lambda)$, there are global minima at $f^* = 0$ and f_p^* (to promote sparsity, we pick $f^* = 0$ as the solution). (c) If $s > \gamma_p(\lambda)$, then the global minimum is uniquely at $f^* > 0$.

Note that $\Omega(f)$ is symmetric in s (i.e., if $s > 0$, we can prove that the solution $f^* \geq 0$; otherwise, $f^* \leq 0$). Thus, without loss of generality, we consider the case $s > 0$. When $s = \gamma_p(\lambda)$, there exists f_p^* (see Figure 2.6(b)) such that

$$\Omega(f_p^*) = \Omega(0) \quad \text{and} \tag{2.15}$$

$$\Omega'(f_p^*) = 0. \tag{2.16}$$

By solving (2.15) and (2.16) simultaneously (see Appendix A.3), we can explicitly find the threshold value $\gamma_p(\lambda)$ for given p and λ values. Specifically, $\gamma_p(\lambda)$ is given by

$$\gamma_p(\lambda) = (2\lambda(1-p))^{\frac{1}{2-p}} + \lambda p(2\lambda(1-p))^{\frac{p-1}{2-p}}. \tag{2.17}$$

For any $s > \gamma_p(\lambda)$, the unique minimum $f^* = S_p(|s|, \lambda)$ of $\Omega(f)$ is greater than 0 and is obtained by setting Ω' to 0 :

$$\Omega'(S_p(|s|, \lambda)) = S_p(|s|, \lambda) - s + \lambda p(S_p(|s|, \lambda))^{p-1} = 0. \tag{2.18}$$

The root of Ω' can be computed using fixed-point iteration (we analyze root finding methods more thoroughly in Section 2.3.2). Then the solution f^* to (2.14) is given by the generalized soft-thersholding (GST) function

$$T_p(s, \lambda) = \begin{cases} 0, & \text{if } |s| \leq \gamma_p(\lambda) \\ \text{sgn}(s)S_p(|s|, \lambda), & \text{if } |s| > \gamma_p(\lambda). \end{cases} \tag{2.19}$$

When $p = 0$, the GST function $T_0(s, \lambda)$ becomes the *hard-thresholding function*, and when $p = 1$, the GST function $T_1(s, \lambda)$ becomes the *soft-thresholding function*. In both cases, we do not compute $S_p(|s|, \lambda)$ in (2.18) iteratively, but rather we compute it explicitly (see Appendix A.4).

Employing Nonnegativity Constraint

Since the subproblems in (2.13) are nonnegatively constrained, the solution of the scalar minimization problem (2.14) also needs to be nonnegative. Therefore the theresholding operator is employed to obtain the next iterate:

$$f^{k+1} = \max(0, T_p(s, \lambda)).$$

Convergence Proof

Here, we prove the convergence of SPIRAL-ℓ_p to a critical point from techniques found in [70, 134]. Suppose a problem of the form

$$\underset{\mathbf{f} \in \mathbb{R}^n}{\text{minimize}} \quad \Phi(\mathbf{f}) = \varphi(\mathbf{f}) + \rho(\mathbf{f}) \tag{2.20}$$

follows the following three mild assumptions:

(A1) φ is proper convex and Lipschitz continuously differentiable on $\mathbb{R}^n_+$,

(A2) ρ is continuous on $\mathbb{R}^n_+$ (not necessarily convex),

(A3) Φ is coercive (i.e., $\lim_{\|\mathbf{f}\| \to \infty} \Phi(\mathbf{f}) = \infty$).

If φ is the negative Poisson log-likelihood function as defined in (1.9) and the function $\rho : \mathbb{R}^n \to \bar{\mathbb{R}} = \mathbb{R} \cup \{-\infty, \infty\}$ is defined as

$$\rho(\mathbf{f}) = \tau\|\mathbf{f}\|_p^p + \delta_+(\mathbf{f}), \tag{2.21}$$

where

$$
\delta_+(\mathbf{f}) = \begin{cases} 0 & \text{if } \mathbf{f} \succeq 0, \\ \infty & \text{otherwise}, \end{cases}
$$

then solving (2.20) is equivalent to solving the SPIRAL-ℓ_p optimization problem

$$
\begin{aligned}
&\underset{\mathbf{f} \in \mathbb{R}^n}{\text{minimize}} \quad F(\mathbf{f}) + \tau \, \|\mathbf{f}\|_p^p \\
&\text{subject to} \quad \mathbf{f} \succeq 0.
\end{aligned} \tag{2.22}
$$

Now note the following: (A1) The negative Poisson log-likelihood function F is convex and Lemma 1 in [70] proves that F is Lipschitz continuously differentiable on $\mathbb{R}_+^n$ with parameter $\beta > 0$. (A2) The penalty function ρ defined in (2.21) with nonconvex ℓ_p-norm term is continuous on $\mathbb{R}_+^n$. (A3) Objective function Φ becomes infinite along any path for which $\|\mathbf{f}\|$ becomes infinite. Therefore, Φ is coercive even with the ℓ_p-norm term.

With these, we can obtain convergence results to a critical point through the following theorem:

Theorem 1. *Suppose the SPIRAL framework [70] with its acceptance test is applied to solve* (2.20) *with the assumption that (A1) to (A3) hold. Then all accumulation points are critical.*

Proof. For contradiction, assume an accumulation point generated by SPIRAL-ℓ_p is not critical. We follow the same proof of Theorem 1 in [70], which we summarize as follows. Lemma 2 [70] shows that in the vicinity of a non-critical point, the solution is a substantial distance away from the current iterate. That is, if the sequence $\{\alpha_{k_j}\}_{j \in \mathbb{Z}_+}$ were bounded, then $\|\mathbf{f}^{k_j+1} - \mathbf{f}^{k_j}\|_2 \geq \epsilon$ for some $\epsilon > 0$ and all j large enough. However, Lemma 4 [70] shows that the sequence $\{\mathbf{f}^k\}_{k \in \mathbb{Z}_+}$ generated by the algorithm is such that the step length $\|\mathbf{f}^{k_j+1} - \mathbf{f}^{k_j}\|_2$ approaches 0 as $k \to \infty$. Therefore, the Lemma 2 result contradicts Lemma 4, hence $\{\alpha_{k_j}\}_{j \in \mathbb{Z}_+}$ must be unbounded. We can now assume that $\{\alpha_{k_j}\}$ increases monotonically to ∞. In order this assumption to be true, α_{k_j} must fail the acceptance test by violating the upper safeguard $\alpha_{\max}$. Then this contradicts Lemma 3 [70]; Lemma 3 assures us to satisfy the acceptance criteria for all sufficiently large values of α_k. All these

contradictions show that any noncritical point can not be an accumulation point. Hence, all accumulation points are critical points. $\square$

Note the function Φ is nonconvex due to the nonconvexity of ρ in SPIRAL-ℓ_p. Therefore, we can not claim that critical points are always global solutions of the problem (2.22). Although it is not guaranteed to converge to a solution, any accumulation point of the SPIRAL-ℓ_p iterations will be a critical point.

Numerical Results

We evaluated the effectiveness of the proposed SPIRAL-ℓ_p method by comparing it to the existing SPIRAL-ℓ_1 method. We implemented the SPIRAL-ℓ_p method in MATLAB (on a PC with Intel Corei7 2.7GHz Processor, 2 cores, 8GB RAM) by modifying the existing MATLAB code of the SPIRAL method [69]. In the experiment, the true signal $\mathbf{f}$ is of length 100,000 with 1,500 nonzero entries (1.5% of sparsity), and the observed vector $\mathbf{y}$ is of length 40,000. We generated Poisson intensity reconstructions for 23 different p-values ranging from 0.99 to 0. For that, we used the parameters in SPIRAL-ℓ_1 experiment as our default parameters in SPIRAL-ℓ_p. More specifically, SPIRAL-ℓ_p is initialized using $\mathbf{A}^T(\mathbf{y})$ and terminates if consecutive iterates do not significantly change. The regularization parameter τ in (1.10) is optimized to get the minimum root-mean-square (RMS) error $\|\mathbf{f}^* - \hat{\mathbf{f}}\|_2 / \|\mathbf{f}^*\|_2$ for each p-value.
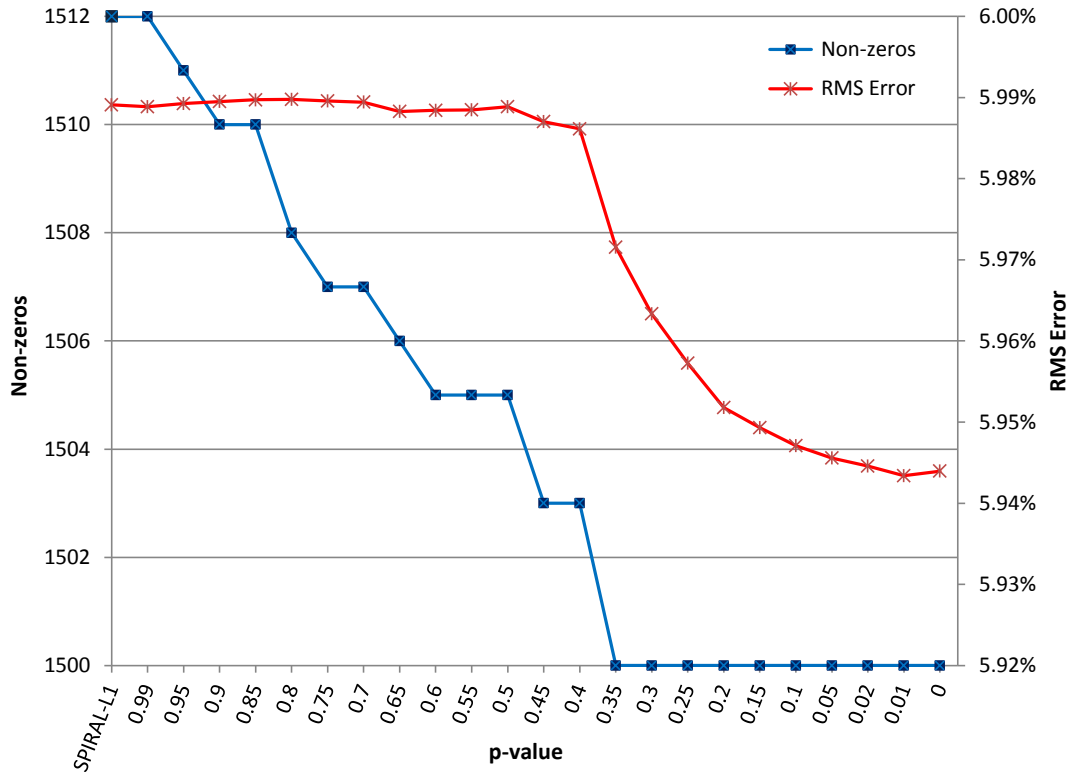
Figure 2.7: The plot of the RMS error and the number of nonzero entries in the reconstruction over the p-values ranging from 0.99 to 0. The left most data points in both curves correspond to the error and number of non-zeros of SPIRAL-ℓ_1. There is a steep decrease in the RMS error after $p = 0.4$ while, non-zeros attain their exact value 1500 at $p = 0.35$. Note RMS error $(\%) = 100 \cdot \|\mathbf{f}^* - \hat{\mathbf{f}}\|_2 / \|\mathbf{f}^*\|_2$.

The RMS error curve in the Fig. 2.7 shows that there is no considerable change in the error for the p-values ranging from 0.99 to 0.4. But when $p < 0.4$, the RMS error decreases drastically and is less than the SPIRAL-ℓ_1 RMS error. Meantime, the number of nonzero entries of the reconstruction also converge to the exact sparsity as p value decreases. These results reveal that the SPIRAL-ℓ_p with p value ranging from 0.35 to 0 can generate better reconstruction than SPIRAL-ℓ_1 method. For instance, when $p = 0.05$, Fig. 2.8 depicts the high accurate SPIRAL-ℓ_p reconstruction without the spurious solutions appear in the SPIRAL-ℓ_1 reconstruction. Furthermore, the SPIRAL-$\ell_{0.05}$ intensity reconstruction exactly matches the sparsity of the true signal. In additional, we note that the amplitude of the SPIRAL-$\ell_{0.05}$ reconstruction is greater than the SPIRAL-ℓ_1 reconstruction.
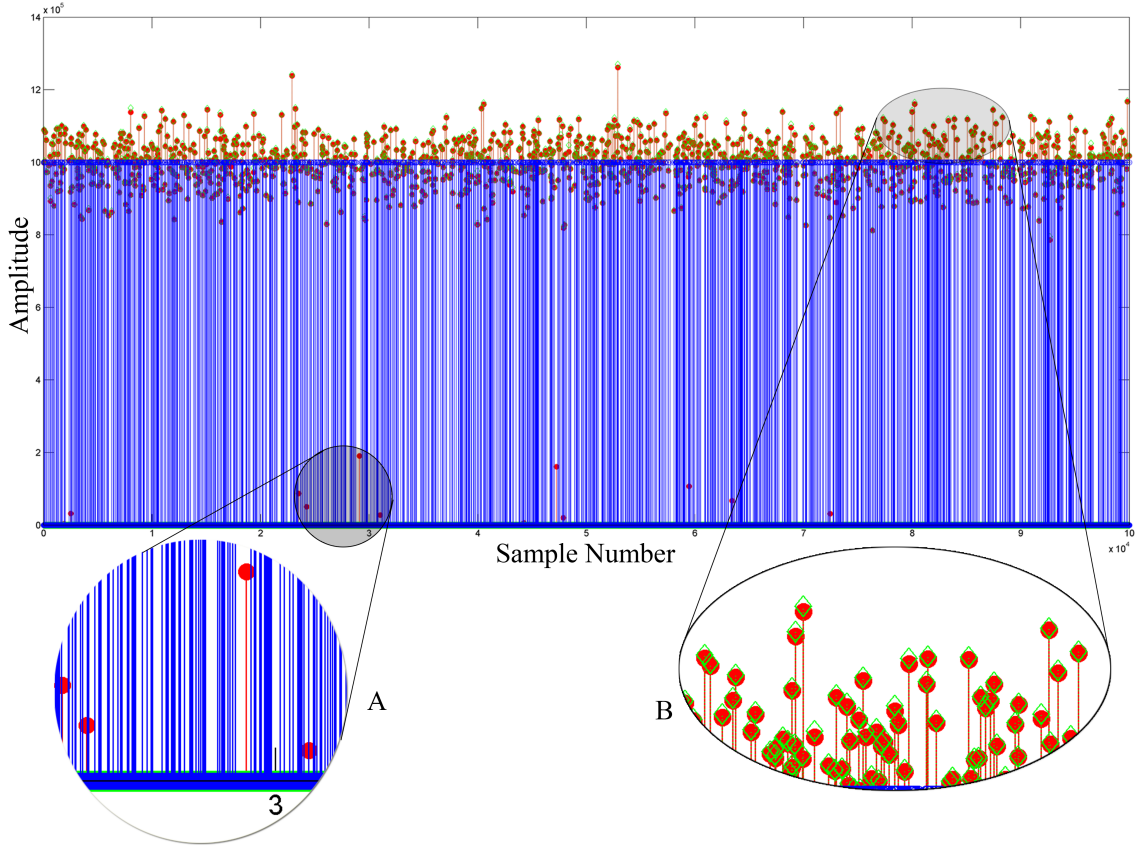
Figure 2.8: SPIRAL-ℓ_p intensity reconstruction with $p = 0.05$ (green diamond stems) compared with the SPIRAL-ℓ_1 intensity reconstruction (red filled circle stems). The blue stems depict the true signal. There are 12 spurious solutions in the SPIRAL-ℓ_1 reconstruction. (A) SPIRAL-$\ell_{0.05}$ reconstruction eliminates spurious solutions in the SPIRAL-ℓ_1 reconstruction. (B) SPIRAL-$\ell_{0.05}$ solution generally matches the SPIRAL-ℓ_1 solution with high strength.

Finally, we ran the proposed SPIRAL-ℓ_p method with $p = 0.05$ for ten different simulated measurement vectors $\mathbf{y}_1, \mathbf{y}_2, \ldots, \mathbf{y}_{10}$ with Poisson noise. Specifically, the Poisson noise levels in y_i's are around 16%, where noise $(\%) = 100 \cdot \|\mathbf{A}\mathbf{f}^* - \mathbf{y}_i\|_2 / \|\mathbf{y}_i\|_2$. The resulting RMS error and the number of nonzeros for each of the final reconstruction are shown in the Table 2.1. In particular, we were able to recover the exact sparsity of the true signal in all ten different experiments with an average of 5.998% RMS error. Therefore, we conclude that for this experimental setup, the proposed SPIRAL-ℓ_p method is robust with respect to different Poisson

Experiment	RMSE (%)	Non-zeros
1	5.945	1500
2	5.947	1500
3	5.959	1500
4	5.991	1500
5	6.140	1500
6	6.077	1500
7	5.827	1500
8	5.955	1500
9	5.973	1500
10	6.162	1500
Average	5.998	1500

Table 2.1: RMS error and number of non-zeros in reconstructions using 10 different Poisson measurements. Here, RMSE (%) $= 100 \cdot \|\mathbf{f}^* - \hat{\mathbf{f}}\|_2 / \|\mathbf{f}^*\|_2$.

noise realizations.

While SPIRAL-ℓ_p generates high accurate, high strength reconstruction for small p-values, it requires more computational time than the SPIRAL-ℓ_1 method. More precisely, SPIRAL-ℓ_1 takes less than 1 second to obtain the reconstruction, while SPIRAL-ℓ_p takes on average, 66 seconds. However, initializing the SPIRAL-ℓ_p with the SPIRAL-ℓ_1 solution improves the computational time approximately by 30%.

Conclusion

In this method, we have formulated the nonnegatively constrained sparse Poisson intensity reconstruction algorithm as a ℓ_p nonconvex regularized minimization problem (2.13). We have showed that this approach can be uncoupled into the separable ℓ_p-minimization problems in the form of (2.14), with each scalar minimization problem is solved using Generalized Soft-Thresholding (GST) function (2.19). We have demonstrated that the proposed SPIRAL-ℓ_p reconstruction for small p values eliminates the spurious artifacts found in the SPIRAL-ℓ_1 reconstruction. While the proposed method leads to more accurate and high strength

reconstructions, it requires more computational effort because evaluating the GST function requires solving a zero-finding problem (2.18) iteratively. We have found that computational time can be decreased significantly by using the SPIRAL-ℓ_1 solution to initialize the SPIRAL-ℓ_p method.

2.3.2 Analysis of the p-Norm Subproblem Minimization

The collaborative work describes in this section is based on the paper by Orkusyan et al.[100]. Recall that the subproblem (2.13) can be uncoupled into scalar minimization problems of the form (2.14), i.e.,

$$
\begin{aligned}
f_s^* \;=\; & \underset{f \in \mathbb{R}}{\arg\min} \quad \Omega_s(f) = \frac{1}{2}(f-s)^2 + \lambda |f|^p, \\
& \text{subject to} \quad f \geq 0.
\end{aligned} \tag{2.23}
$$

where f and s denote elements of the vectors $\mathbf{f}$ and $\mathbf{s}^k$ respectively and $\lambda = \tau/\alpha_k$. Recall from Section 2.3.1, given a regularization parameter $\lambda > 0$ and p-norm for $\Omega_s(f)$ in (2.23), there exists a threshold value $\gamma_p(\lambda)$ (that explicitly depends on p and λ) such that if $s \leq \gamma_p(\lambda)$, the global minimum of (2.23) is $f_s^* = 0$; otherwise, the global minimum will be a non-zero value (see Fig. 2.9). When $s = \gamma_p(\lambda)$, there exists f_γ^* such that

$$
\Omega_\gamma(f_\gamma^*) \;=\; \Omega_\gamma(0) \quad \text{and} \quad \Omega_\gamma'(f_\gamma^*) \;=\; 0. \tag{2.24}
$$

By solving (2.24) simultaneously, we can explicitly find the threshold value $\gamma_p(\lambda)$ for given p and λ values. For any $s > \gamma_p(\lambda)$, the unique minimum f_s^* of $\Omega_s(f)$ is greater than 0 and is obtained by setting Ω_s' to 0:

$$
\Omega_s'(f_s^*) = f_s^* - s + \lambda p (f_s^*)^{p-1} = 0. \tag{2.25}
$$

We now describe zero-finding algorithms to compute the root f_s^*.

Fixed-Point Iteration Method

A point f^* is said to be a fixed point of a function $G(f)$ if $G(f^*) = f^*$. Setting $\Omega_s'(f)$ equal to zero, we have $s - \lambda p (f^*)^{p-1} = f^*$. The fixed-point iteration method
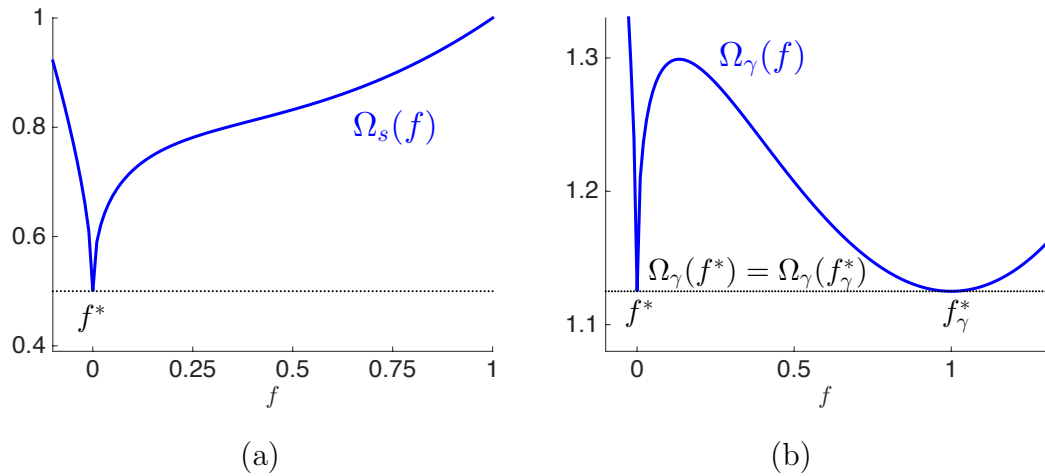
Figure 2.9: The plot of the scalar quadratic function $\Omega_s(f)$, where $p = 0.5$ and $\lambda = 1.0$. (a) When s is less than the specific threshold value $\gamma_p(\lambda)$, then $f_s^* = 0$ is the unique global minimum. (b) When $s = \gamma_p(\lambda)$, there are global minima at $f^* = 0$ and f_γ^*. If $s > \gamma_p(\lambda)$, then the global minimum is uniquely at some $f_s^* > 0$.

is an iterative method for finding fixed points of a function. In particular, it defines a sequence of points $\{f_n\}$ given by $f_{n+1} = G(f_n)$. In the previous Section 2.3.1, we used the fixed point iteration for finding the root of $\Omega_s'(f)$:

$$f_{n+1} = g(f_n) = s - \lambda p f_n^{p-1}. \tag{2.26}$$

Newton's Method

There are various ways of defining fixed point iterations. One particular fixed-point formulation is Newton's method, which is given by the iterations

$$f_{n+1} = G(f_n) = f_n - \frac{\Omega_s'(f_n)}{\Omega_s''(f_n)}.$$

In our case, the iterations for Newton's method are given by

$$f_{n+1} = f_n - \frac{f_n - s + \lambda p f_n^{p-1}}{1 + \lambda p(p-1)f_n^{p-2}} = \frac{s + \lambda p(p-2)f_n^{p-1}}{1 + \lambda p(p-1)f_n^{p-2}}.$$

In order to simplify the computation of this iteration and avoid computing two different roots f_n^{p-1} and f_n^{p-2}, we multiply the numerator and denominator by f_n^{2-p}:

$$f_{n+1} = \frac{s f_n^{2-p} + \lambda p(p-2)f_n}{f_n^{2-p} + \lambda p(p-1)}. \tag{2.27}$$

The performance of fixed-point iteration and Newton's method very much depend on the choice of the initial point f_0, which we discuss next.

Initialization

When $s = \gamma_p(\lambda)$, the solution f_γ^* such that

$$\Omega'(f_\gamma^*) = f_\gamma^* - \gamma_p(\lambda) + \lambda p (f_\gamma^*)^{p-1} = 0$$

is given explicitly by

$$f_\gamma^* = (2\lambda(1-p))^{\frac{1}{2-p}}.$$

Then if $s = \gamma_p(\lambda) + \varepsilon$ for some $\varepsilon > 0$, we now analyze how to estimate f_s^* to initialize the zero-finding methods described previously.

First-order Taylor series approximation. To define the initial point, we can linearize $\Omega_s'(f)$ around f_γ^* and find the zero of the linearization. More specifically,

$$
\begin{aligned}
\Omega_s'(f_\gamma^* + \delta) &\approx \Omega_s'(f_\gamma^*) + \delta \Omega_s''(f_\gamma^*) \\
&= f_\gamma^* - (\gamma_p(\lambda) + \varepsilon) + \lambda p (f_\gamma^*)^{p-1} \\
&\quad + \delta(1 + \lambda p(p-1)(f_\gamma^*)^{p-2}) \\
&= -\varepsilon + \delta(1 + \lambda p(p-1)(f_\gamma^*)^{p-2}).
\end{aligned}
$$

Setting this equal to zero and solving for δ suggests the use of the initialization

$$f_s^0 = f_\gamma^* + \delta, \quad \text{where } \delta = \frac{\varepsilon}{1 + \lambda p(p-1)(f_\gamma^*)^{p-2}}.$$

Second-order Taylor series approximation. Similarly, we can use a second-order Taylor approximation to Ω_s' around f_γ^*:

$$\Omega_s'(f_\gamma^* + \delta) \approx \Omega_s'(f_\gamma^*) + \delta \Omega_s''(f_\gamma^*) + \frac{\delta}{2} \Omega_s'''(f_\gamma^*),$$

which yields the following approximation:

$$f_s^0 = f_\gamma^* + \delta, \quad \text{where } \delta = \frac{-b + \sqrt{b^2 - 4ac}}{2a},$$
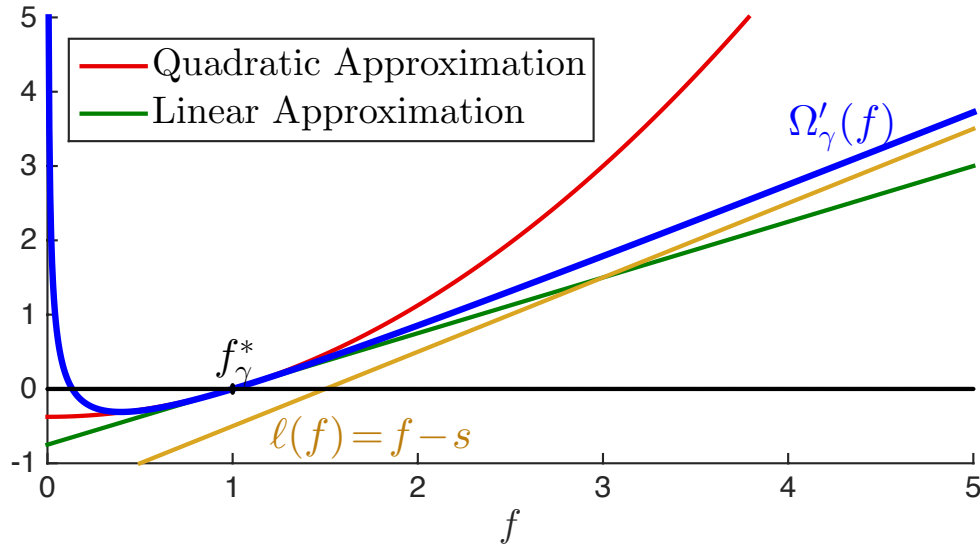
Figure 2.10: Approximations to $\Omega'_\gamma(f)$ centered at f^*_γ. As f increases, both the linear and quadratic Taylor approximation diverge from $\Omega'_\gamma(f)$. In contrast, the approximation $\ell(f) = f - s$, which are the first two terms in $\Omega'_\gamma(f)$, is more accurate for large values of f.

where

$$
\begin{aligned}
a &= \frac{\lambda p(p-1)(p-2)}{2}(f^*_\gamma)^{p-3} \\
b &= 1 + \lambda p(p-1)(f^*_\gamma)^{p-2} \\
c &= -\varepsilon.
\end{aligned}
$$

The linearization and second-order Taylor approximation, however, diverge quickly from the true solution as f^*_s becomes large (see Fig. 2.10). We now discuss bounds on f^*_s that allow us to make more effective initial approximations to f^*_s. We first prove a lemma, which will be useful in showing bounds on f^*_s as well as other results.

Lemma 1. *Let $\lambda > 0$ and $0 \leq p < 1$. Then for $s \geq \gamma_p(\lambda)$, $\lambda p(1-p)(f^*_s)^{p-2} \leq \frac{p}{2}$.*

Proof. Recall that for $s = \gamma_p(\lambda)$, there exists an $f^*_\gamma > 0$ such that (**??**) hold. From $\Omega_\gamma(f^*_\gamma) = \Omega_\gamma(0)$, we can obtain

$$
\frac{1}{2}f^*_\gamma + \lambda(f^*_\gamma)^{p-1} = \gamma_p(\lambda), \tag{2.28}
$$

and from $\Omega'_\gamma(f^*_\gamma) = 0$, we have

$$f^*_\gamma + \lambda p(f^*_\gamma)^{p-1} = \gamma_p(\lambda). \tag{2.29}$$

Setting (2.28) equal to (2.29) and with some algebraic manipulation, we have $\lambda p(1-p)(f^*_\gamma)^{p-2} = \frac{p}{2}$. For $s > \gamma_p(\lambda)$, the unique minimizer $f^*_s > f^*_\gamma$. Thus,

$$\lambda p(1-p)(f^*_s)^{p-2} < \lambda p(1-p)(f^*_\gamma)^{p-2} = \frac{p}{2},$$

which completes the proof. $\qquad\square$

This result allows us to prove the following theorem, which bounds the minimizer, f^*_s, of $\Omega_s(f)$:

Theorem 2. *For $\lambda > 0$ and $0 \le p < 1$, the minimizer, f^*_s, of Ω_s is bounded by $f^*_s \le s$. If $0 \le p \le \frac{1}{2}$, then the minimizer is further bounded by $\frac{2}{3}s \le f^*_s \le s$.*

Proof. Recall that the minimizer of Ω_s solves $\Omega'_s(f^*_s) = 0$. Solving for f^*_s, we have

$$f^*_s = \frac{s}{1 + \lambda p(f^*_s)^{p-2}}. \tag{2.30}$$

Rewriting the main result of Lemma 1, we obtain $\lambda p(f^*_s)^{p-2} \le \frac{p}{2(1-p)}$. Observe that if $p \le \frac{1}{2}$,

$$\lambda p(f^*_s)^{p-2} \le \frac{p}{2(1-p)} \le \frac{1}{2} \quad \text{and} \quad 1 \le 1 + \lambda p(f^*_s)^{p-2} \le \frac{3}{2}.$$

Using these bounds in (2.30) yields the desired results. $\qquad\square$

Note that Theorem 1 implies that as s increases, so does f^*_s. Moreover, as $s \to \infty$, $(f^*_s)^{p-2} \to 0$, and therefore, by (2.25), $f^*_s \to s$. Thus, a sensible initial estimate for f^*_s is s.

Fixed-point initialized Newton's Method. We can improve the initial guess from s by finding a point between f^*_s and s. The mean-value theorem guarantees the existence of $\xi \in (f^*_s, s)$ such that

$$\Omega''_s(\xi) = \frac{\Omega'_s(s) - \Omega'_s(f^*_s)}{s - f^*_s}.$$

Rearranging, we find that

$$f_s^* = s - \frac{\Omega_s'(s) - \Omega_s'(f_s^*)}{\Omega_s''(\xi)} = s - \frac{\lambda p s^{p-1}}{1 - \lambda p(1-p)\xi^{p-2}}.$$

By Lemma 1, $\frac{2-p}{2} \leq 1 - \lambda p(1-p)\xi^{p-2} \leq 1$, and thus,

$$f_s^* \approx s - \lambda p s^{p-1} \in (f^*, s).$$

We note that this is precisely the first fixed point iteration initialized at s.

Guarantee of Convergence

Let $e_n = f_n - f^*$ and $e_{n+1} = f_{n+1} - f^*$ represent the errors on the n-th and $n+1$-th iterations respectively. For fixed point iteration, we have

$$\begin{aligned}
e_{n+1} = f_{n+1} - f^* &= G(f_n) - f^* \\
&= G(f^* + e_n) - f^*, \\
&= G(f^*) + e_n G'(f^*) + e_n^2 G''(\xi) - f^* \\
&= f^* + e_n G'(f^*) + e_n^2 G''(\xi) - f^* \\
&= e_n G'(f^*) + e_n^2 G''(\xi).
\end{aligned}$$

For small e_n, $e_{n+1} \approx e_n G'(f^*)$. In our context,

$$G(f) = s - \lambda p f^{p-1} \quad \text{and} \quad G'(f) = \lambda p(1-p)f^{p-2}.$$

By Lemma 1, $G'(f) < 1$. Therefore, the error is decreasing and the fixed point iteration method is guaranteed to converge.

To show Newton's method is guaranteed to converge, let f_c be a critical point of $\Omega_s'(f)$ i.e. $\Omega_s''(f_c) = 0$. In particular, $f_c = (\lambda p(1-p))^{\frac{1}{2-p}}$ and for any $f > f_c$, $\Omega_s''(f) = 1 + \lambda p(p-1)f^{p-2} > 0$ i.e. $\Omega_s'(f)$ is increasing in the interval (f_c, ∞). Then, $\Omega_s'''(f) = \lambda p(p-1)(p-2)f^{p-3} > 0$ for all $f \in (0, \infty)$, which implies $\Omega_s'(f)$ is convex. Finally, we note that $f_c < (2\lambda p(p-1))^{\frac{1}{2-p}} = f_\gamma^* \leq f^*$, i.e $\Omega_s'(f)$ has a root in (f_c, ∞). Therefore, $\Omega_s'(f)$ is increasing, convex, and has a zero in (f_c, ∞), and Newton's method is guaranteed to converge from any starting point in the interval (f_c, ∞) (see Theorem 2 pg. 86 in [80]).

Rate of convergence. Let ε be some set tolerance such that on the n-th iteration if $|e_n| = |f_n - f_s^*| \leq \varepsilon$ then we will consider the algorithm to have converged to the root. For fixed point iteration, we have convergence when

$$\varepsilon \geq |e_n| = C_1|e_{n-1}| = C_1^n|e_0| \tag{2.31}$$

where $C_1 = G'(f_s^*) = \lambda p(1 - p)(f_s^*)^{p-2}$. Solving for n, the number of iterations required to converge, we have

$$n_{\text{Fixed Point}} \geq \frac{\ln \varepsilon - \ln |e_0|}{\ln C_1}. \tag{2.32}$$

For Newton's method, we have convergence when

$$\varepsilon \geq |e_n| = C_2|e_{n-1}|^2 = C_2^{2^n-1}|e_0|^{2^n} \tag{2.33}$$

where $C_2 = \frac{1}{2}\frac{\lambda p(1-p)(2-p)(f_s^*)^{p-3}}{1 - \lambda p(1-p)(f_s^*)^{p-2}}$. Solving for n in (2.33) yields

$$n_{\text{Newton}} \geq \frac{1}{\ln 2}\ln\left(\frac{\ln C_2 + \ln \varepsilon}{\ln C_2 + \ln e_0}\right). \tag{2.34}$$

Fig. 2.11 shows the theoretical number of iterations for fixed-point iterations and Newton's method to converge. Note that when s is near $\gamma_p(\lambda)$, fixed-point iterations take many more iterations than Newton's method. However, for large s, fixed-point iterations only require four iterations. Although this is still twice as many as the iterations for Newton's method, the number of floating point operations for fixed-point iterations is much smaller than that for Newton's method (compare (2.26) and (2.27)). Since s can take on any real value, we expect the average performance of fixed-point iteration and Newton's method will be comparable, which we see in the next section.

Numercal experiments

We simulated a 3D cubic phantom with two embedded fluorescence capillary rod targets. For the finite element mesh, there are a total of 8,690 nodes inside the 3D cube while only 36 nodes are located inside the two rods. The fluorophore concentration of the nodes is set to 7,000 inside the two rods and 0 outside. We
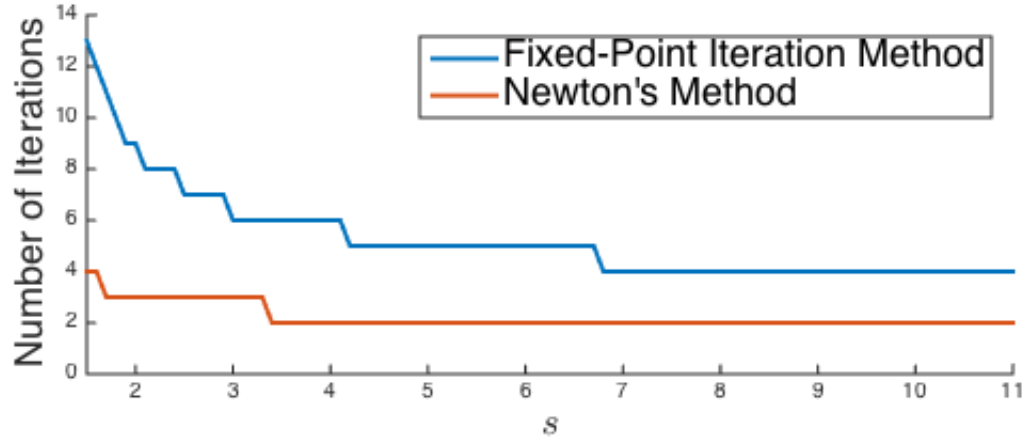
Figure 2.11: Theoretical number of iterations required to converge as a function of s. Here $p = 0.5$, $\lambda = 1$, $\varepsilon = 10^{-8}$, $e_0 = s - f^*$, and $\gamma_p(\lambda) \leq s \leq 11$.

chose a total of 20 excitation source positions and $1,057$ detector positions on the top surface of the cube, which gives us $20 \times 1{,}057 = 21{,}140$ measurements. About one-tenth of all the measurements were used (i.e. $2{,}120$ measurements). We assumed that the excitation wavelength is 650 nm and the emission wavelength is 720 nm in the construction of the system matrix $\mathbf{A}$. The tissue optical properties were $\mu_a = 0.0022\,\text{mm}^{-1}$, $\mu_s' = 1.41\,\text{mm}^{-1}$ at both 650 nm and at 720 nm. For this experiment, the simulated measurement vector $\mathbf{y}$ is corrupted by Poisson noise with signal-to-noise ratio (SNR) of 3 dB ($\approx 57\%$ noise). In our method, we used $p = 0.74$ and $\mathbf{A}^T \mathbf{y}$ as the initial guess. Fig. 2.12 shows the true signal ($\mathbf{f}^*$) and our reconstruction.

	Time (sec)	Iterations
Fixed-point iteration	21.2829	1,281,974
Newton's method	21.0128	476,585

Table 2.2: Time and iteration average over 10 trials for fixed-point iteration and Newton's method to reconstruct the fluorescence molecular tomography data.
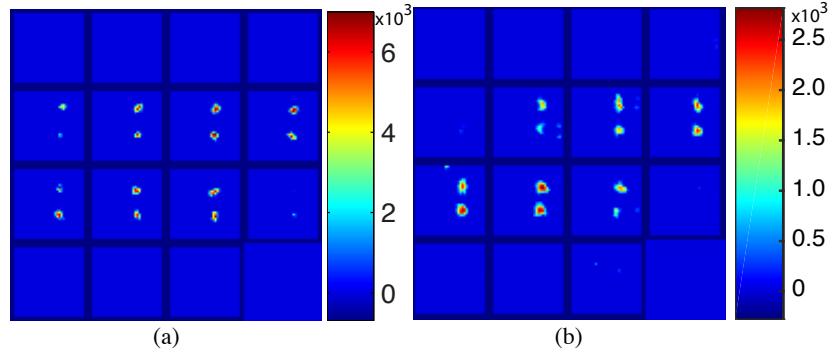
Figure 2.12: (a) Horizontal slices of a simulated fluorescence capillary rod targets. (b) Reconstruction using p-norm regularized subproblem minimization.

Conclusion

Here, we analyzed methods for solving the p-norm regularized subproblems arising from minimizing the Poisson-log likelihood for reconstructing sparse signals from photon-limited measurements. These non-convex subproblems do not have closed form solutions, and as such, they require numerical approaches for computing the minimizers. While Newton's method in theory should converge to the solution faster than fixed-point iterations, the number of floating-point operations needed to perform each iteration offsets the computational advantage of using derivative information.

2.3.3 p-th Power Total Variation Regularization

The sparse recovery method describes in this section is based on the paper by Adhikari and Marcia [4]. When the signal to be reconstructed is known to be sparse in the canonical basis, it can be recovered accurately using a nonconvex ℓ_p-norm regularization technique as we discussed in Section 2.3.1. However, when the image is not sparse, a different regularization technique must be employed. The total variation (TV) seminorm penalty [104] has been commonly used as a sparsity measure and has been shown to be very effective as a regularization term for image reconstruction. More specifically, the TV seminorm measures the first-order difference between adjacent pixels in images. Thus, an image with a small TV seminorm means that generally, it has homogeneous signal levels with few

abrupt changes or edges. The recent work of Yan and Lu [138] generalizes this TV seminorm to the p-th power (TV_p), where $0 < p \le 1$, by using a weighted TV minimization where the weights are computed to approximate the TV_p regularized problem locally.

TV seminorm regularized Poisson intensity reconstruction problem (2.4) has been solved in many previous works. In the efforts [60] and [107], the split Bergman approach [65] was used to solve the Poisson problem, but the proposed methods are not suitable for large scale problems due to a matrix inversion operation involve with those approaches. In this study, we propose to regularize the negative Poisson log-likelihood function (1.9) using the TV_p penalization method in [138]. Specifically, we use the SPIRAL approach [70] to define a sequence of minimization subproblems with the TV_p penalty. These subproblems are solved using the FISTA method for modified TV-based denoising approach [27]. We explore the effectiveness of the proposed method through numerical experiments in image deblurring and compare the results with the state-of-the-art SPIRAL-TV_1 results.

We propose to regularize the negative Poisson log likelihood function in (1.10) using a p-th power total variation [138], denoted by TV_p ($0 < p \le 1$). Then the sequence of subproblems in (2.3) can be written as

$$\mathbf{f}^{k+1} \;=\; \underset{\mathbf{f} \in \mathbb{R}^{mn}}{\arg\min} \quad \frac{1}{2} \parallel \mathbf{f} - \mathbf{s}^k \parallel_2^2 \;+\; \frac{\tau}{\alpha_k} \|\mathbf{f}\|_{\text{TV}_p} \tag{2.35}$$
$$\text{subject to} \quad \mathbf{f} \succeq 0,$$

where $\|\mathbf{f}\|_{\text{TV}_p}$ is defined as the anisotropic TV seminorm

$$\|\mathbf{f}\|_{\text{TV}_p^{(\text{A})}} = \sum_{i=1}^{m-1} \sum_{j=1}^{n} |f_{i,j} - f_{i+1,j}|^p + \sum_{i=1}^{m} \sum_{j=1}^{n-1} |f_{i,j} - f_{i,j+1}|^p, \tag{2.36}$$

or as the isotropic TV seminorm

$$\|\mathbf{f}\|_{\text{TV}_p^{(\text{I})}} = \sum_{i=1}^{m-1} \sum_{j=1}^{n-1} \sqrt{(f_{i,j} - f_{i+1,j})^{2p} + (f_{i,j} - f_{i,j+1})^{2p}}$$
$$+ \sum_{i=1}^{m-1} |f_{i,n} - f_{i+1,n}|^p + \sum_{j=1}^{n-1} |f_{m,j} - f_{m,j+1}|^p. \tag{2.37}$$

When $p = 1$ in (2.36) and (2.37), $\text{TV}_p^{(\text{A})}$ and $\text{TV}_p^{(\text{I})}$ recover the standard $\text{TV}_1^{(\text{A})}$ and $\text{TV}_1^{(\text{I})}$ respectively. Note that when $p < 1$, both TV_p penalty functions are

nonconvex, making the global minimum of (2.35) difficult to trace. In [138], the minimization of the nonconvex problem (2.35) is accomplished through the convexification of the nonconvex penalty function $\|\mathbf{f}\|_{\mathrm{TV}_p}$ using a reweighting strategy. More specifically, a weighted TV seminorm is used to approximate the anisotropic TV_p seminorm in (2.36) as

$$\|\mathbf{f}\|_{\mathrm{TV}_w^{(A)}} = \sum_{i=1}^{m-1}\sum_{j=1}^{n}\alpha_{i,j}|f_{i,j}-f_{i+1,j}| + \sum_{i=1}^{m}\sum_{j=1}^{n-1}\beta_{i,j}|f_{i,j}-f_{i,j+1}|, \quad (2.38)$$

and the isotropic TV_p seminorm in (2.37) as

$$\|\mathbf{f}\|_{\mathrm{TV}_w^{(I)}} = \sum_{i=1}^{m-1}\sum_{j=1}^{n-1}\sqrt{(\alpha_{i,j}(f_{i,j}-f_{i+1,j}))^2 + (\beta_{i,j}(f_{i,j}-f_{i,j+1}))^2}$$
$$+ \sum_{i=1}^{m-1}\alpha_{i,n}|f_{i,n}-f_{i+1,n}| + \sum_{j=1}^{n-1}\beta_{m,j}|f_{m,j}-f_{m,j+1}|. \quad (2.39)$$

In the above weighted TV definitions, $\alpha_{i,j} > 0$ and $\beta_{i,j} > 0$ are coefficients whose values are computed using $\mathbf{f}$ in the previous iterate k:

$$\alpha_{i,j} = (|f_{i,j}^{(k)} - f_{i+1,j}^{(k)}| + \epsilon)^{(p-1)}, \quad (2.40)$$
$$\beta_{i,j} = (|f_{i,j}^{(k)} - f_{i,j+1}^{(k)}| + \epsilon)^{(p-1)}, \quad (2.41)$$

where $\epsilon > 0$ to prevent the weights from being zero. By substituting (2.40) and (2.41) for $\alpha_{i,j}$ and $\beta_{i,j}$ in the weighted TV definitions (2.38) and (2.39), it can be shown that $\|\mathbf{f}\|_{\mathrm{TV}_w^{(A)}} \approx \|\mathbf{f}^{(k)}\|_{\mathrm{TV}_p^{(A)}}$ and $\|\mathbf{f}\|_{\mathrm{TV}_w^{(I)}} \approx \|\mathbf{f}^{(k)}\|_{\mathrm{TV}_p^{(I)}}$ (see [138] for details).

Modified Dual Approach with Weighted TV Norms

Using the weighted TV functions as defined in (2.38) and (2.39), we now show how to modify the FISTA approach of dual problem construction [27, 39]. In particular, we use the exact same set of notations used in Sec. 4.1 of [27] with the exception of the linear operator $\mathscr{L}$.

Let $\mathcal{P}_A$ be the set of matrix-pairs $(\mathbf{p}_1, \mathbf{q}_1)$ where $\mathbf{p}_1 \in \mathbb{R}^{(m-1)\times n}$ and $\mathbf{q}_1 \in \mathbb{R}^{m\times(n-1)}$ satisfying

$$|p_{i,j}| \leq 1, \quad i = 1, \ldots, m-1, \, j = 1, \ldots, n,$$
$$|q_{i,j}| \leq 1, \quad i = 1, \ldots, m, \, j = 1, \ldots, n-1.$$

Similarly, let $\mathcal{P}_I$ be the set of matrix-pairs $(\mathbf{p}_2, \mathbf{q}_2)$ where $\mathbf{p}_2 \in \mathbb{R}^{(m-1)\times n}$ and $\mathbf{q}_2 \in \mathbb{R}^{m\times(n-1)}$ that satisfy

$$
\begin{aligned}
p_{i,j}^2 + q_{i,j}^2 &\leq 1, \quad i = 1,\ldots,m-1, \ j = 1,\ldots,n-1, \\
|p_{i,n}| &\leq 1, \quad i = 1,\ldots,m-1, \\
|q_{m,j}| &\leq 1, \quad j = 1,\ldots,n-1.
\end{aligned}
$$

We redefine the linear operator $\mathcal{L} : \mathbb{R}^{(m-1)\times n} \times \mathbb{R}^{m\times(n-1)} \longrightarrow \mathbb{R}^{m\times n}$ as follows:

$$
\mathcal{L}(\mathbf{p}_\ell, \mathbf{q}_\ell)_{i,j} = \alpha_{i,j}p_{i,j} - \alpha_{i-1,j}p_{i-1,j} + \beta_{i,j}q_{i,j} - \beta_{i,j-1}q_{i,j-1},
$$

where ℓ is 1 or 2, and we assume that

$$
p_{0,j} = p_{m,j} = q_{i,0} = q_{i,n} \equiv 0 \ \text{ for } \ i = 1,\ldots,m, \ j = 1,\ldots,n.
$$

The operator $\mathcal{L}^T : \mathbb{R}^{m\times n} \longrightarrow \mathbb{R}^{(m-1)\times n} \times \mathbb{R}^{m\times(n-1)}$ is given by

$$
\mathcal{L}^T(\mathbf{x}) = (\mathbf{p}_\ell, \mathbf{q}_\ell),
$$

where $\mathbf{p}_\ell \in \mathbb{R}^{(m-1)\times n}$ and $\mathbf{q}_\ell \in \mathbb{R}^{m\times(n-1)}$ are the matrices defined by

$$
\begin{aligned}
p_{i,j} &= x_{i,j} - x_{i+1,j}, \quad i = 1,\ldots,m-1, \ j = 1,\ldots,n, \\
q_{i,j} &= x_{i,j} - x_{i,j+1}, \quad i = 1,\ldots,m, \ j = 1,\ldots,n-1.
\end{aligned}
$$

Since our subproblems (2.35) are non-negatively constrained, P_C is the orthogonal projection operator on to the set $C = [0, \infty)$.

Now note that the following two relations

$$
\begin{aligned}
\alpha|x| &= \max_{p}\{\alpha x p \ : \ |p| \leq 1\}, \\
\sqrt{\alpha^2 x^2 + \beta^2 y^2} &= \max_{p_1, p_2}\{\alpha x p_1 + \beta y p_2 : p_1^2 + p_2^2 \leq 1\},
\end{aligned}
$$

hold true for weights $\alpha > 0$ and $\beta > 0$ (see Appendix A.6). Therefore, the anisotropic weighted TV seminorm can be written as the maximization problem

$$
\|\mathbf{f}\|_{\mathrm{TV}_w^{(\mathrm{A})}} = \max_{(\mathbf{p}_1, \mathbf{q}_1)\in\mathcal{P}_A} T_1(\mathbf{f}, \mathbf{p}_1, \mathbf{q}_1),
$$

where

$$T_1(\mathbf{f}, \mathbf{p}_1, \mathbf{q}_1) \;=\; \sum_{i=1}^{m-1}\sum_{j=1}^{n} \alpha_{i,j}(f_{i,j} - f_{i+1,j})p_{i,j} \;+\; \sum_{i=1}^{m}\sum_{j=1}^{n-1} \beta_{i,j}(f_{i,j} - f_{i,j+1})q_{i,j}.$$

Similarly, the isotropic weighted TV seminorm also can be written as the maximization problem

$$\|\mathbf{f}\|_{\mathrm{TV}_w^{(\mathrm{I})}} = \max_{(\mathbf{p}_2,\mathbf{q}_2)\in\mathcal{P}_I} T_2(\mathbf{f}, \mathbf{p}_2, \mathbf{q}_2),$$

where

$$\begin{aligned}
T_2(\mathbf{f}, \mathbf{p}_2, \mathbf{q}_2) \;=\;& \sum_{i=1}^{m-1}\sum_{j=1}^{n-1}[\alpha_{i,j}(f_{i,j} - f_{i+1,j})p_{i,j} + \beta_{i,j}(f_{i,j} - f_{i,j+1})q_{i,j}] \\
&+ \sum_{i=1}^{m-1} \alpha_{i,n}(f_{i,n} - f_{i+1,n})p_{i,n} \;+\; \sum_{j=1}^{n-1} \beta_{m,j}(f_{m,j} - f_{m,j+1})q_{m,j}.
\end{aligned}$$

With the above defined notations, we have

$$T_1(\mathbf{f}, \mathbf{p}_1, \mathbf{q}_1) = \mathrm{Tr}(\mathscr{L}(\mathbf{p}_1, \mathbf{q}_1)^T\mathbf{f}),$$

$$T_2(\mathbf{f}, \mathbf{p}_2, \mathbf{q}_2) = \mathrm{Tr}(\mathscr{L}(\mathbf{p}_2, \mathbf{q}_2)^T\mathbf{f}).$$

Hereafter we can follow the same procedure explained in [27] to obtain the dual problem with the weighted TV norm. This dual problem is iteratively solved using a fast gradient projection method [27].

Numerical Results

In this section, we demonstrate the effectiveness of the proposed algorithm, which we call SPIRAL-TV$_p$. In particular, we consider an image deblurring problem for which TV norm regularization is highly suitable.

In this experimental setup, we used the Shepp-Logan phantom image of size 128×128 available in the MATLAB's image processing toolbox as the true image $\mathbf{f}^*$ (see Fig. 2.13(a)). The true detector blurred image (see Fig. 2.13(b)) was obtained by $\mathbf{Af}^*$, where $\mathbf{A}$ is a blurring operator ($\mathbf{f}^*$ is convolved with some blur matrix). Finally, a Poisson noisy observation matrix of size 128×128 was simulated by MATLAB's `poissrnd` function. The Poisson noisy observation matrix is shown in Fig. 2.13(c), where the mean photon count is 45.8 with a maximum of 398.

(a) Truth image (f*) (b) True detector (c) Observed photon
intensity (Af*) counts (y)
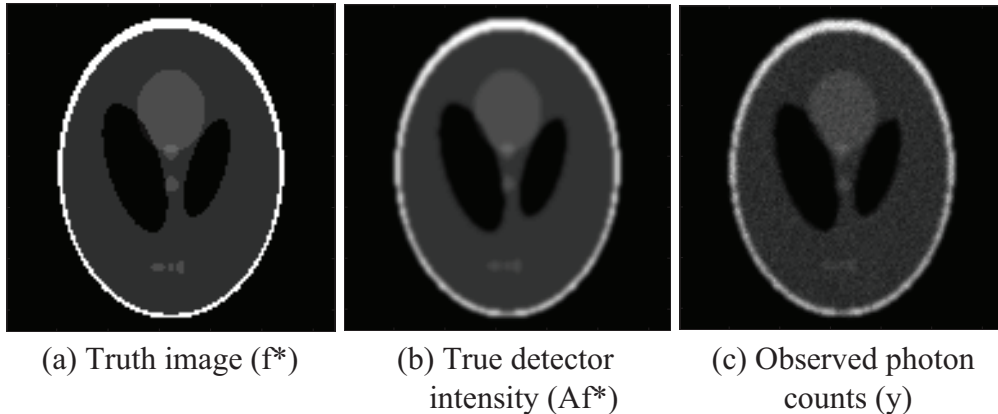
Figure 2.13: Experimental setup: (a) Shepp-Logan head phantom as true image, (b) blurred phantom image, (c) Poisson noisy phantom image with mean count 45.8.

We implemented the SPIRAL-TV$_p$ algorithm in MATLAB R2013a (on a PC with Intel Core i7 2.7GHz Processor with 8GB memory) by modifying existing codes of the SPIRAL method [69] and the TV-based FISTA denoising method [26]. SPIRAL-TV$_p$ follows a warm-start strategy, where we start the method by solving the $p = 1$ case first, and then using its solution to initiate the next problem with a smaller p value, say, $p = 0.9$. (This can be viewed as a homotopy or continuation method.) In Eqs. (2.40) and (2.41), $\epsilon = 10^{-13}$ in our numerical experiments. We run the algorithm until the relative difference between consecutive iterates converged to $\|\mathbf{f}^{k+1} - \mathbf{f}^k\|_2/\|\mathbf{f}^k\|_2 \leq 10^{-8}$ with a minimum of 50 iterations. For each p-value, the regularization parameter in (2.35) is optimized to get minimum RMSE value. Finally, we compared SPIRAL-TV$_p$ reconstruction with SPIRAL-TV$_1$ reconstruction for both isotropic and anisotropic TV types using RMSE values and peak signal-to-noise ratios (PSNR (dB) = $10\log_{10}(\max(\mathbf{f}^*)^2/\mathrm{MSE})$).

The results of the experiments for anisotropic and isotropic TV regularization are presented in Figs. 2.14 and 2.15 respectively. For the anisotropic TV regularization, the SPIRAL-TV$_{0.8}$ reconstruction has RMSE = 11.57% and PSNR =30.95 dB while the reconstruction for SPIRAL-TV$_1$ reconstruction has RMSE = 11.90% and PSNR = 30.70 dB. For the isotropic TV regularization, the SPIRAL-TV$_{0.8}$ reconstruction has RMSE = 14.45% and PSNR = 29.02 dB while the reconstruction for SPIRAL-TV$_1$ reconstruction has RMSE = 14.80% and PSNR = 28.80 dB.

(a) SPIRAL-TV$_1$
PSNR = 30.70 dB

(b) Truth − SPIRAL-TV$_1$
RMSE = 11.90%

(c) Zoomed region

(d) SPIRAL-TV$_{0.8}$
PSNR = 30.95 dB

(e) Truth − SPIRAL-TV$_{0.8}$
RMSE = 11.57%

(f) Zoomed region
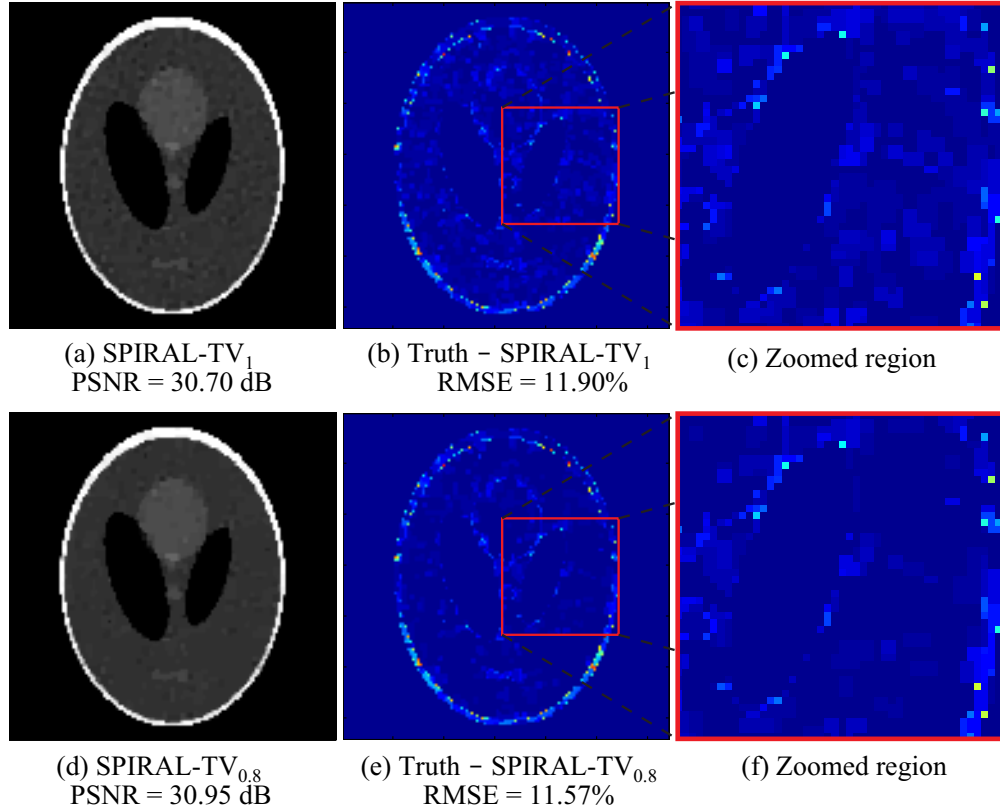
Figure 2.14: **Anisotropic TV** based reconstructions and error images. Top row: (a) SPIRAL-TV$_1$ reconstruction, (b) magnitude of error between the true image and the SPIRAL-TV$_1$ estimated image, (c) SPIRAL-TV$_1$ reconstruction has more artifacts. Bottom row: (d) SPIRAL-TV$_{0.8}$ reconstruction, (e) magnitude of error between the true image and the SPIRAL-TV$_{0.8}$ estimated image, (f) SPIRAL-TV$_{0.8}$ reconstruction has more homogeneous signal levels.

In both cases and both metrics, the SPIRAL-TV$_{0.8}$ reconstructions show improvement over the SPIRAL-TV$_1$ reconstructions. Furthermore, the SPIRAL-TV$_{0.8}$ reconstructions recovered the actual gray area in the phantom body without losing the edge details and has less prominent cloud noise-like texture (see red zoomed areas in Fig. 2.14 (c) and (f) and Fig. 2.15 (c) and (f)).

Conclusion

Here, we have formulated a TV$_p$ regularized negative log-likelihood function for photon-limited imaging problems. This nonconvex TV$_p$ regularization problem is solved in a convex setting by using a reweighting strategy for each iteration. The

(a) SPIRAL-TV$_1$
PSNR = 28.80 dB

(b) Truth − SPIRAL-TV$_1$
RMSE = 14.80%

(c) Zoomed region

(d) SPIRAL-TV$_{0.8}$
PSNR = 29.02 dB

(e) Truth − SPIRAL-TV$_{0.8}$
RMSE = 14.45%

(f) Zoomed region
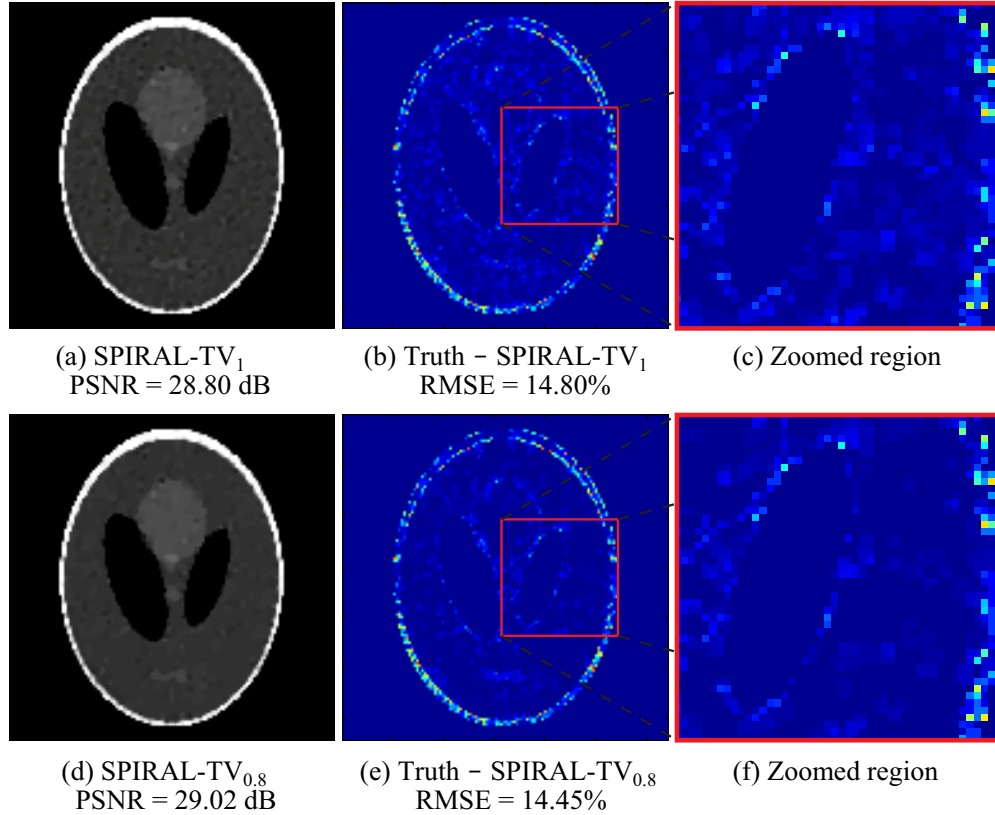
Figure 2.15: **Isotropic TV** based reconstructions and error images. Top row: (a) SPIRAL-TV$_1$ reconstruction, (b) magnitude of error between the true image and the SPIRAL-TV$_1$ estimated image, (c) SPIRAL-TV$_1$ reconstruction has more artifacts. Bottom row: (d) SPIRAL-TV$_{0.8}$ reconstruction, (e) magnitude of error between the true image and the SPIRAL-TV$_{0.8}$ estimated image, (f) SPIRAL-TV$_{0.8}$ reconstruction also has more homogeneous signal levels.

SPIRAL-TV$_1$ solution is used as the warm initial point in the proposed SPIRAL-TV$_p$ method, and we proceed with this strategy by reducing the p-value. Under the warm-start strategy, the proposed SPIRAL-TV$_p$ algorithm will converge to a reasonably good local solution that is more accurate than the SPIRAL-TV$_1$ global solution. Since the anisotropic TV is related to the ℓ_1-norm, the SPIRAL-TV$_p$ with the anisotropic TV leads to more accurate results than with the isotropic TV. In our experience with this particular data set, there is no any significant improvement in reconstructions for p-values less than 0.8. While the proposed SPIRAL-TV$_p$ method leads to more accurate results with less artifacts, it requires more computational effort than SPIRAL-TV$_1$ due to the iterative nature of the

warm-start strategy.

2.3.4 Non-Convex Shannon Entropy Regularization

The work describes in this section is based on the paper by Adhikari and Marcia [7]. In this method, we propose to regularize the Poisson log-likelihood objective function (1.9) by the *generalized* nonconvex Shannon entropy function:

$$H_p(\mathbf{f}) = -\sum_{i=1}^{n} \frac{|f_i|^p}{\|\mathbf{f}\|_p^p} \log\left(\frac{|f_i|^p}{\|\mathbf{f}\|_p^p}\right), \tag{2.42}$$

where $p > 0$. This regularizer enforces sparsity by driving the solution towards axes (see Fig. 2.16). Then the corresponding subproblems (1.10) can be written as

$$\mathbf{f}^{k+1} = \underset{\mathbf{f}\in\mathbb{R}^n}{\arg\min} \quad \frac{1}{2}\|\mathbf{f} - \mathbf{s}^k\|_2^2 + \frac{\tau}{\alpha_k} H_p(\mathbf{f}) \tag{2.43}$$
$$\text{subject to} \quad \mathbf{f} \succeq 0.$$
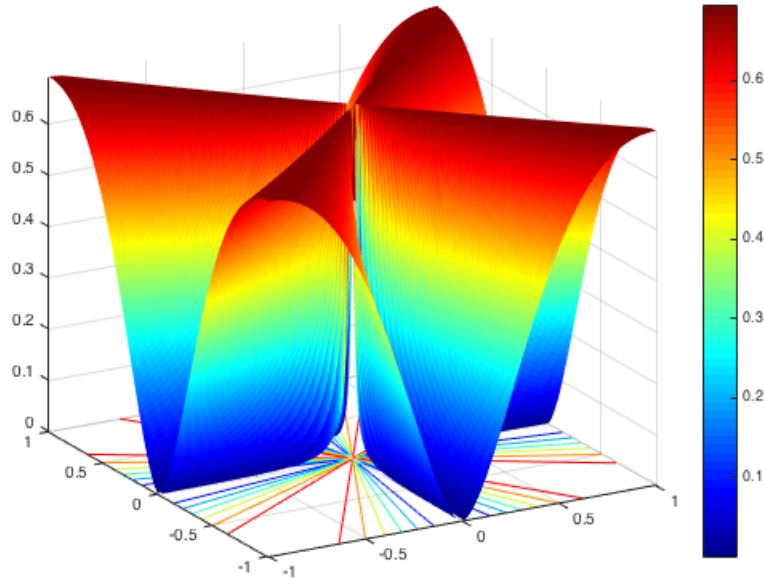
Figure 2.16: The *generalized* nonconvex Shannon entropy function $H_p(\mathbf{f})$ with $p = 0.5$ in 2D space.

The nonconvex Shannon entropy function (2.42) was recently proposed by Huang et al. [75] as a sparse-promoting penalizer for Gaussian noise based re-

constructions. A Shannon form of entropy [108] based Bayesian image reconstruction method has been studied by Nunez et al. [98] for the Hubble space telescope data. Skilling et al. [112] maximized the Shannon entropy: $-\sum_{j=1}^{n} p_j \log(p_j)$, where $p_j = f_j / \sum_{i=1}^{n} f_i$, for image recovery in astronomy. Moreover, Donoho et al. [50] recovered nearly-black objects by minimizing the Shannon entopy regularized least-squares function. Our approach is novel in regularizing the Poisson log-likelihood using the sparsity promoting generalized Shannon entropy function (2.42) in photon-limited context. In order to make the problem (2.43) separable, we replace $H_p(\mathbf{f})$ using its first-order Taylor series approximation at current iterate $\mathbf{f}^k$:

$$H_p^k(\mathbf{f}) \equiv H_p(\mathbf{f}^k) + \nabla H_p(\mathbf{f}^k)^T(\mathbf{f} - \mathbf{f}^k),$$

where the gradient of $H_p^k(\mathbf{f})$ is computed by

$$\nabla H_p(\mathbf{f}) = \begin{bmatrix} \frac{\partial H_p(\mathbf{f})}{\partial |f_1|} \\ \frac{\partial H_p(\mathbf{f})}{\partial |f_2|} \\ \vdots \\ \frac{\partial H_p(\mathbf{f})}{\partial |f_n|} \end{bmatrix},$$

where

$$\frac{\partial H_p(\mathbf{f})}{\partial |f_i|} = -\frac{p|f_i|^{p-1}}{\|\mathbf{f}\|_p^p} \log |f_i|^p + \frac{p|f_i|^{p-1}}{\|\mathbf{f}\|_p^{2p}} \sum_{\ell=1}^{n} |f_\ell|^p \log |f_\ell|^p, \qquad \text{for } i = 1 \ldots n.$$

Manipulating this Taylor approximation and ignoring constant terms yield a sequence of subproblems of the form

$$\mathbf{f}^{k+1} = \arg\min_{\mathbf{f} \succeq 0} \quad \frac{1}{2} \sum_{i=1}^{n} (f_i - s_i^k)^2 + \sum_{i=1}^{n} \frac{\tau}{\alpha_k} (\nabla H_p(\mathbf{f}^k))_i f_i, \qquad (2.44)$$

where s_i^k is the i-th element of the vector $\mathbf{s}^k$. The minimizer $\mathbf{f}^{k+1}$ can be computed analytically by solving each scalar function of the form

$$f^* = \arg\min_{f \geq 0} \quad \frac{1}{2}(f - s)^2 + \gamma f, \qquad (2.45)$$

where f and s denote i-th element of the vectors $\mathbf{f}$ and $\mathbf{s}^k$ respectively and $\gamma = \frac{\tau}{\alpha_k}(\nabla H_p(\mathbf{f}^k))_i$. Then the minimum of (2.45) is given by

$$f^* = [s - \gamma]_+,$$

where a thresholding operator $[\,\cdot\,]_+ = \max\{0,\cdot\}$ is employed to get a nonnegative solution.

Numerical Experiments

We investigate the effectiveness and efficiency of the proposed method, which we call SPIRAL-Shannon, by comparing it to the existing SPIRAL-ℓ_1 [70] and SPIRAL-ℓ_p [5] methods (on a MacBook Pro with Intel Core i7 2.8GHz 4 cores Processor with 16GB memory). Here, we use 16% Poisson noise corrupted observed vector $\mathbf{y}$ of length 4×10^4 to recover a true signal $\mathbf{f}$ of length 10^5 with 1.5% sparsity. All algorithms are initialized with $\mathbf{A}^T(\mathbf{y})$ and terminate if consecutive iterates do not change significantly.
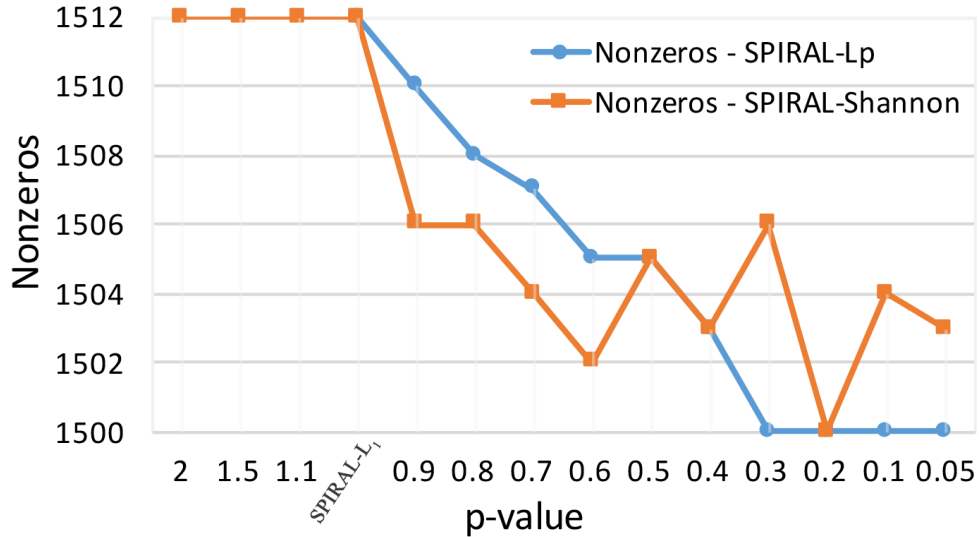
Figure 2.17: Number of nonzeros in the reconstructions of SPIRAL-ℓ_1, SPIRAL-ℓ_p and the proposed SPIRAL-Shannon over the p-values. Note that the number of nonzeros are started to decrease after $p = 1$ for both the SPIRAL-ℓ_p and SPIRAL-Shannon.

The number of nonzeros in the reconstruction of SPIRAL-Shannon (see Fig. 2.17) decreases drastically after $p < 1$ and recover the exact sparsity (i.e., $1,500$) at $p = 0.2$. Even though the SPIRAL-ℓ_p converges monotonically to the exact sparsity at $p = 0.3$, it requires more computational effort than the SPIRAL-Shannon

method (see Fig. 2.18). On average, SPIRAL-Shannon and SPIRAL-ℓ_p methods recover the true signal with root mean square error 0.059.
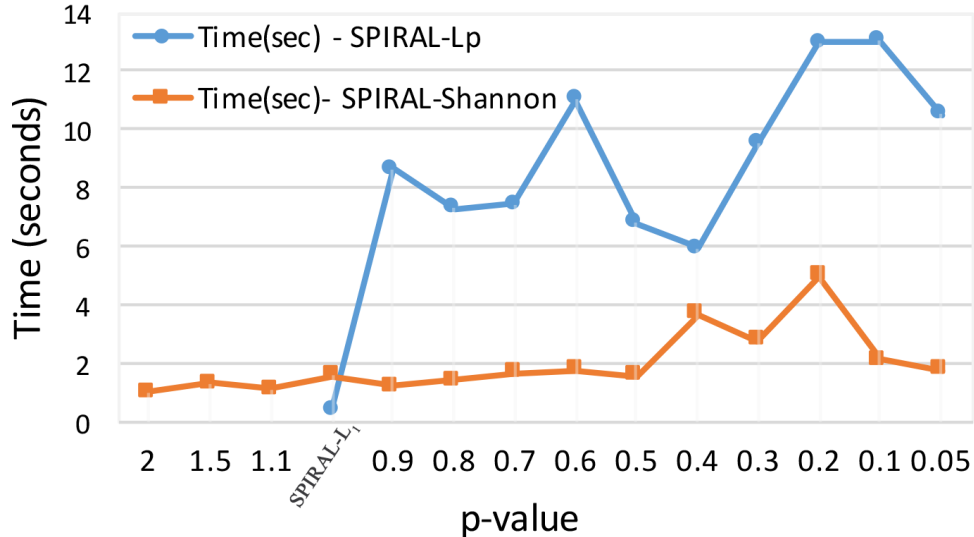
Figure 2.18: Computation time of the SPIRAL-ℓ_1, SPIRAL-ℓ_p and SPIRAL-Shannon over the p-values. Note that the proposed SPIRAL-Shannon requires significantly low computational effort to obtain comparable results.

Conclusion

We proposed a novel Poisson intensity reconstruction method by introducing sparsity promoting Shannon entropy penalizer to the photon-limited imaging. Unlike previous nonconvex methods, the proposed method achieved comparable results with less computational effort.

2.4 Summary of Contribution

In this chapter, we proposed four novel sparse signal recovery methods in the Poisson noise context: (1) A bounded photon-limited image recovery algorithm: Proposed to incorporate upper and lower bound constraints that model additional signal intensity information, (2) a non-convex ℓ_p-norm regularization method (SPIRAL-ℓ_p). Here, we provided local convergence proof under some mild

conditions for SPIRAL-ℓ_p. Furthermore, we analyzed zero-finding methods for solving the p-norm regularized minimization subproblems arising from a sequential quadratic approach, (3) a non-convex p-th power total variation (TV$_p$) regularization method. This work introduced TV$_p$ regularization for image recovery problems in photon-limited context using iterative reweighting, (4) a non-convex Shannon entropy regularization method. To the best of our knowledge, this is the first time to use the generalized version of the Shannon entropy for sparse Poisson intensity reconstruction.

Chapter 3

Applications with Poisson Process Model

In this chapter, we demonstrate the effectiveness of the proposed nonconvex sparse Poisson intensity reconstruction algorithms that we discussed in Chapter 2 with real world application in medical imaging and computational genomics. Specifically, we propose two novel stage-based approaches to solve time-dependent tomography problems in medical imaging: Bioluminescence tomography and fluorescence lifetime imaging.

3.1 Fluorescence Molecular Tomography

The work describes in this section is based on the paper by Adhikari et al. [9]. As an emerging near-infrared molecular imaging modality, fluorescence molecular tomography (FMT) has great potential in resolving the molecular and cellular processes in 3D objects through the reconstruction of the injected fluorescence probe concentration. In practice, when a charge-coupled device (CCD) camera is used to obtain FMT measurements, the observations are corrupted by noise which follows a Poisson distribution [68]. To reconstruct the original concentration, the standard least-squares function for data-fitting is not a suitable objective function to minimize since this model assumes measurement noise which follows a Gaussian distribution. Most of recent studies [130, 146] in solving FMT problem, assumed

Gaussian type noise and are based on the least-square model. In the rare cases where the Poisson noise was considered in solving the FMT problem, such as in a recent work of Yu [140], the least-squares model was still used as objective function.

Based on the SPIRAL-ℓ_p approach explained in Section 2.3.1, we propose to solve the ill-posed, ill-conditioned FMT reconstruction problem only using a relatively small number of observations with Poisson noise. Using simulated FMT data with different Poisson noise levels, we compare the performance of the proposed method with the newest Gaussian-based Non-Uniform Multiplicative weighting with Ordered Subsets (NUMOS) algorithm [147] with respect to different image quality metrics (VR, Dice, CNR, and MSE) as mentioned in Appendix A.5.

3.1.1   Numerical Results
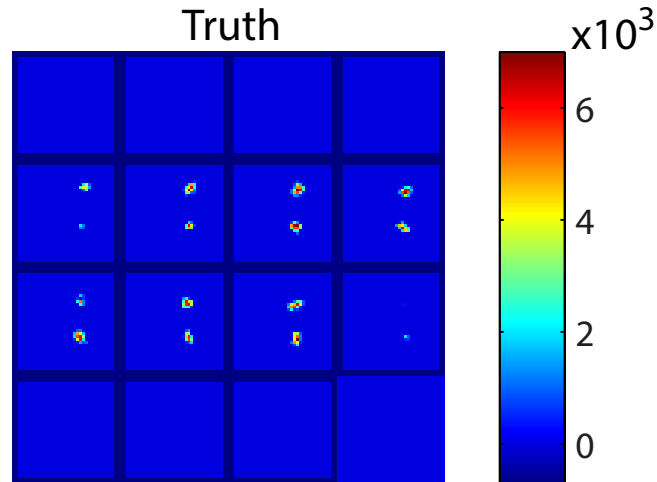
Figure 3.1: The true image of the simulated cube.

In this experiment, we simulated a 3D cubic phantom with two embedded fluorescence capillary rod targets as shown in Fig.3.1. For the finite element mesh, there are a total of 8,690 nodes inside the 3D cube while only 36 nodes are located inside the two rods. The fluorophore concentration of the nodes is set to 7,000 inside the two rods and 0 outside. More specifically, the true signal $\mathbf{f}^*$ of length 8,690 with 36 nonzero entries ($\approx 0.41\%$ of sparsity) and the corresponding system matrix $\mathbf{A}$ of size 2,120 $\times$ 8,690 were obtained from Prof. Changqing Li's medical
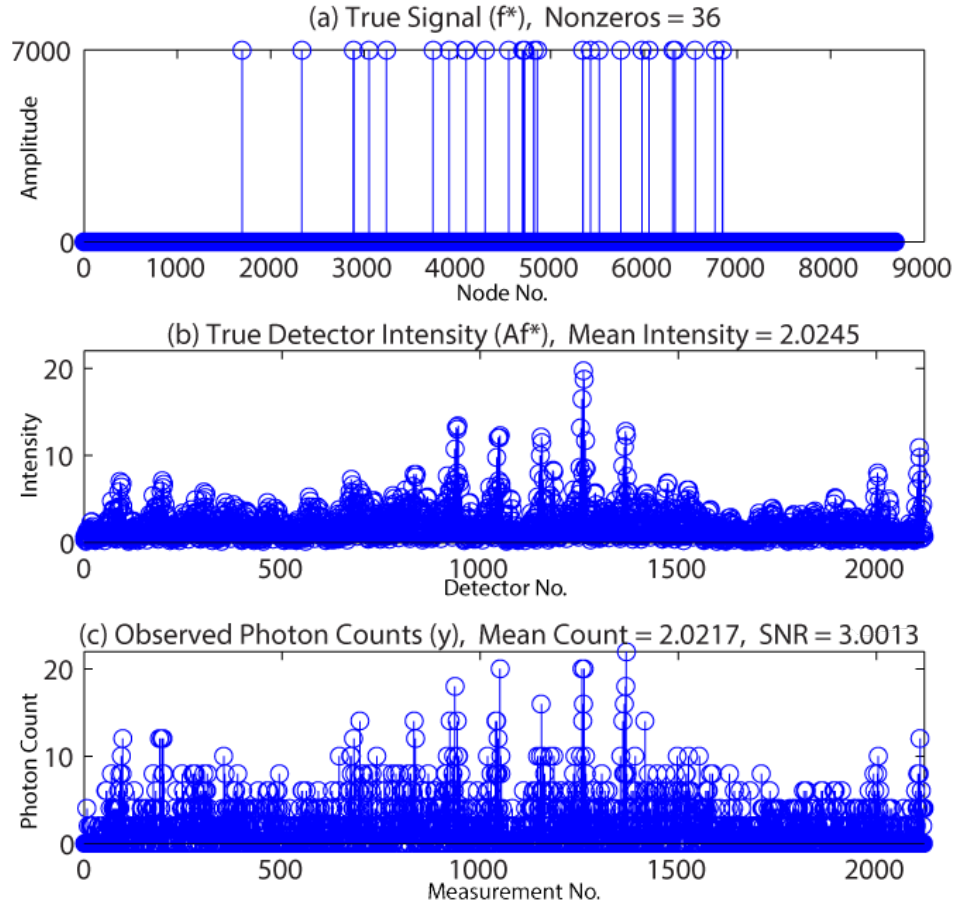
Figure 3.2: Experimental setup. (a) True signal ($\mathbf{f}^*$) of size 8,690 with 36 nonzero entries. (b) True intensity ($\mathbf{Af}^*$) at 2,120 detectors. (c) Very low mean photon count measurements ($\mathbf{y}$) with 57% Poisson noise (SNR $\approx$ 3). Note that the dimension of the measurement vector $\mathbf{y}$ is four times smaller than the dimension of the true signal ($\mathbf{f}^*$).

imaging lab. We simulated measurement vector $\mathbf{y}$ is of length 2,120 having Poisson noises with signal-to-noise ratio (SNR) of 20 ($\approx$ 10% noise), 10 ($\approx$ 30% noise) and 3 ($\approx$ 57% noise), where noise (%) $= 100 \cdot \|\mathbf{Af}^* - \mathbf{y}\|_2 / \|\mathbf{y}\|_2$. Fig. 3.2 shows the true signal ($\mathbf{f}^*$), the true detector intensity ($\mathbf{Af}^*$), and the measurement vector $\mathbf{y}$ for the case SNR $\approx$ 3.
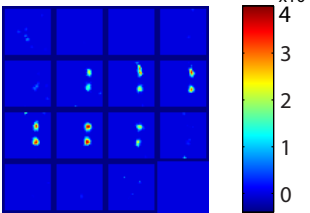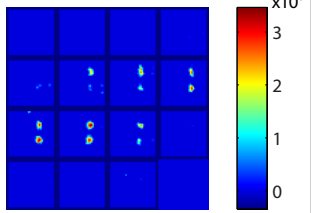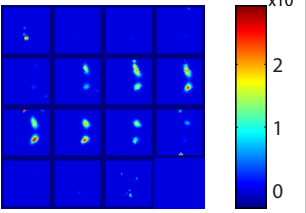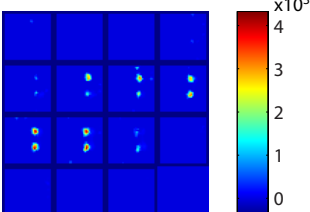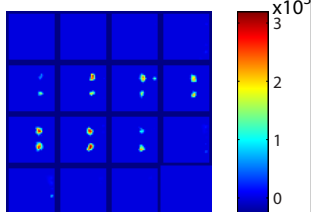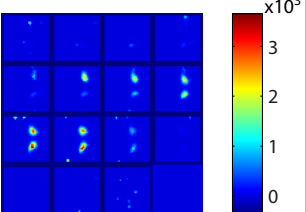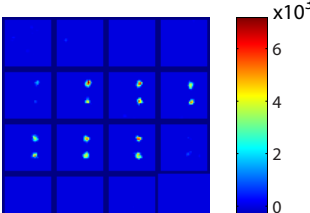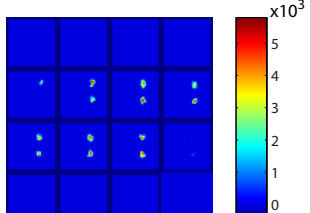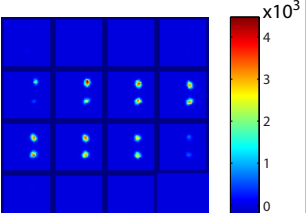
Table 3.1: Reconstructed horizontal slice images of the simulated cube using SPIRAL-ℓ_1, SPIRAL-$\ell_p(p = 0.74)$ and NUMOS method: (a) when SNR $\approx$ 3 dB (57% Poisson noise), (b) when SNR $\approx$ 10 dB (30% Poisson noise), and (c) when SNR $\approx$ 20 dB (10% Poisson noise).
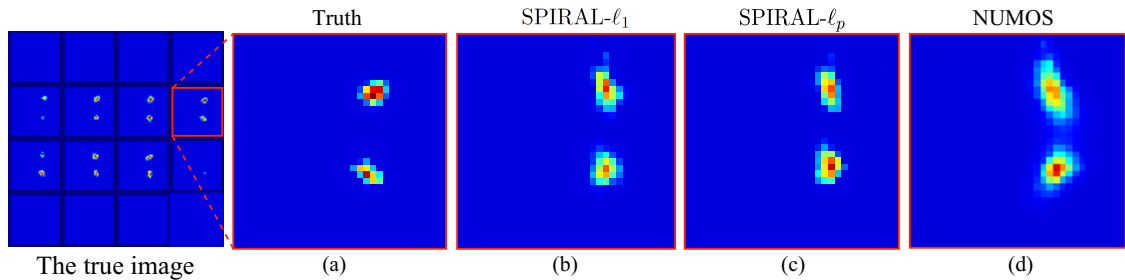
Figure 3.3: Zoomed version of a reconstructed slice image (see red box) using the three different methods when SNR $\approx$ 3: (a) Truth slice, (b) SPIRAL-ℓ_1 reconstructed slice, (c) more localized and high contrast SPIRAL-$\ell_p(p = 0.74)$ reconstructed slice, (d) NUMOS reconstructed slice with smooth-out edges.

The reconstructed results for each method for different Poisson noise levels are shown in Table 3.1, and the corresponding detailed image quality metrics are given in Table 3.2. When the SNR is high (SNR $\approx$ 20 or 10% noise), we can see that the all methods perform well. NUMOS performs particularly well in obtaining more localized targets with high location accuracy. For low SNR measurements (SNR $\approx$ 3), SPIRAL-ℓ_p method outperforms the NUMOS and SPIRAL-ℓ_1 methods in obtaining locationally accurate targets with more strength (see Fig. 3.3). In the 30% Poisson noise experiment (SNR $\approx$ 10), even though the both SPIRAL-ℓ_1 and SPIRAL-ℓ_p perform quite well with relatively close image quality metrics, SPIRAL-ℓ_p image has very low background artifacts. For the SNR $\approx$ 3 setting, on average, SPIRAL-ℓ_p requires about 30 seconds for reconstruction, SPIRAL-ℓ_1 requires 15 seconds, and NUMOS requires 3 seconds.

SNR	Algorithm	VR	Dice	CNR	MSE
	SPIRAL-ℓ_1	0.95	0.30	7.40	9.1×10^4
≈ 3	**SPIRAL$-\ell_p$**	**1.10**	**0.35**	**7.90**	**8.8×10^4**
	NUMOS	1.10	0.32	7.20	9.3×10^4
	SPIRAL-ℓ_1	1.01	0.43	10	7.0×10^4
≈ 10	**SPIRAL$-\ell_p$**	**0.98**	**0.47**	**10**	**7.8×10^4**
	NUMOS	0.94	0.42	8.70	8.3×10^4
	SPIRAL-ℓ_1	0.73	0.61	16	3.8×10^4
≈ 20	SPIRAL-ℓ_p	1.01	0.61	12	5.5×10^4
	NUMOS	**0.94**	**0.63**	**14**	**4.5×10^4**

Table 3.2: Metrics of the best reconstructions under different SNR levels ($\approx$ 3, 10, 20) using SPIRAL-ℓ_1, SPIRAL-ℓ_p ($p = 0.74$), and NUMOS algorithms. In the best case, VR and Dice metrics have to be closed to 1, CNR value should be higher, and MSE value should be lower. Those best selections are in boldface letters.

3.2 Time-Dependent Bioluminescence Tomography

The work describes in this section is based on the paper by Adhikari et al. [2]. In bioluminescence imaging one seeks to reconstruct sources of light contained within a tissue sample from boundary measurements of scattered light. This imaging modality provides valuable insight into *in vivo* cellular and molecular processes in small animals, for example [55]. For this imaging problem, measured signals are modeled by solutions of an initial-boundary value problem of a partial differential equation modeling the multiple scattering of light by tissues. Hence, the main challenge in this problem lies in processing signals that are constrained by partial differential equations.

For this problem, it is reasonable to assume a sparse distribution of sources. In that regard, there have been several recent results that have employed sparsity-promoting methods to solve this bioluminescence imaging problem, *e.g.* [62, 63, 71, 24, 54, 143]. For all of those studies, the sources did not vary in time. In contrast, Unlu and Gulsen [127] identify the importance of considering a time-dependent source for these imaging problems.

Motivated by this study, we take on the problem of reconstructing time-dependent bioluminescent sources. In particular, we consider measurements with relatively low photon counts so that one must explicitly consider Poisson noise in the data. For that case, we employ the nonconvex Sparse Poisson Intensity Reconstruction ALgorithm (SPIRAL-ℓ_p) [5] to solve the nonconvex problem for the negative Poisson log-likelihood function. We show that this approach applied to the time-averaged data provides an effective method for reconstructing the spatial support of the bioluminescent sources. Upon determining these supports, we recover the characteristic time decay of each of the sources from the time-dependent data. We show using numerical simulations that this two-stage reconstruction method effectively solves this time-dependent bioluminescence problem.

The remainder of this section is as follows. In Section 3.2.1, we describe the forward model and inverse problem that make up this time-depdendent biolumines-

cence imaging problem. In Section 3.2.2, we describe the details of our two-stage method to recover the sources from boundary measurements of scattered light corrupted by Poisson noise. We give results from numerical simulations demonstrating this method in Section 3.2.3. Section 3.2.4 gives our conclusions.

3.2.1 Problem Formulation

Consider the domain Ω with boundary $\partial\Omega$ composed of a uniform absorbing and scattering medium. We assume that the optical properties of this medium are known to reasonable precision. Contained within Ω are a sparse distribution of time-dependent sources. For the time-dependent bioluminescence imaging problem, we seek to recover the spatial locations of these sources as well as their characteristic time behavior. In what follows, we describe the forward model and then the corresponding inverse problem for this bioluminescence problem.

Forward model

We model light scattering and absorption in the medium using the diffusion approximation [131, 12]. Let $\phi(\mathbf{r}, t)$ denote the optical fluence rate at position $\mathbf{r}$ at time t. It satisfies the diffusion equation,

$$\frac{1}{c}\frac{\partial \phi}{\partial t} - \kappa\nabla^2\phi + \mu_a\phi = S \quad \text{in } \Omega \times (0, T], \tag{3.1}$$

with κ denoting the diffusion coefficient, μ_a denoting the absorption coefficient, and S denoting the time-dependent bioluminescent sources contained in the medium. We solve (3.1) subject to initial condition

$$\phi(\mathbf{r}, 0) = 0 \quad \text{in } \Omega, \tag{3.2}$$

and boundary condition

$$\phi + 2\kappa\partial_n\phi = 0 \quad \text{on } \partial\Omega \times (0, T] \tag{3.3}$$

Here, $\partial_n\phi$ denotes the outward normal derivative of ϕ. Note that S provides the only source of light in this problem. Upon solution of the initial-boundary value

problem consisting of (3.1) subject to (3.2) and (3.3), we model measurements of scattered light leaving the boundary of the medium, $u(\mathbf{r}, t)$, through evaluation of

$$u(\mathbf{r}, t) = -\kappa \partial_n \phi = \frac{1}{2}\phi \quad \text{on } \partial\Omega \times (0, T]. \tag{3.4}$$

Note that we have substituted (3.3) into the first result of (3.4) to obtain the final result of (3.4).

Suppose we consider the time-averaged data defined as

$$\bar{u}(\mathbf{r}) = \frac{1}{2}\bar{\phi}(\mathbf{r}) = \frac{1}{2T} \int_0^T \phi(\mathbf{r}, t)\mathrm{d}t \quad \text{on } \partial\Omega. \tag{3.5}$$

The steady-state optical fluence rate, $\bar{\phi}$, satisfies the steady-state diffusion equation

$$-\kappa\nabla^2\bar{\phi} + \mu_a\bar{\phi} = \bar{S} \quad \text{in } \Omega, \tag{3.6}$$

subject to the boundary condition

$$\bar{\phi} + 2\kappa\partial_n\bar{\phi} = 0 \quad \text{on } \partial\Omega. \tag{3.7}$$

We will make use of this boundary value problem consisting of (3.6) subject to (3.7) in the analysis that follows.
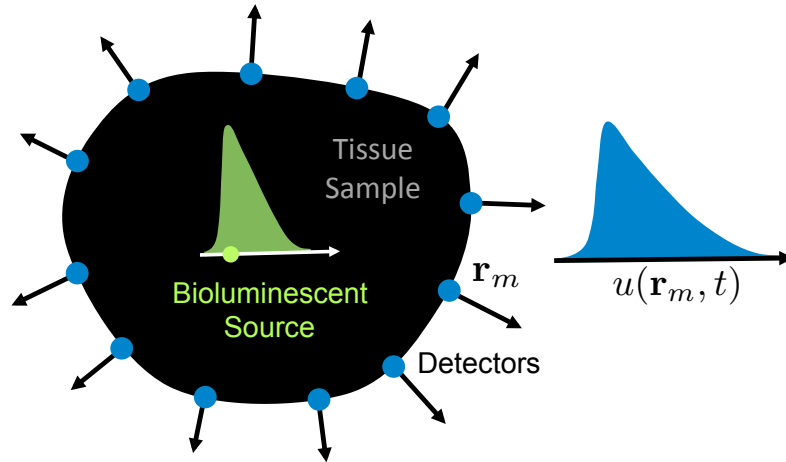
Figure 3.4: Schematic diagram of time-dependent bioluminescence tomography. Photon-count measurements $u(\mathbf{r}_m, t)$ are collected at detectors, which are placed at boundary locations $\mathbf{r}_m$ for $m = 1, \ldots, M$.

Inverse problem

Suppose we take measurements of the scattered light leaving the boundary of the medium at M distinct locations denoted by $\mathbf{r}_m \in \partial\Omega$ for $m = 1, \cdots, M$. Moreover, suppose we collect N samples these measurements in time with sampling rate, Δt with $T = N\Delta t$. This entire collection of data is given by the vector $\mathbf{u} \in \mathbb{R}^{MN}$ with

$$\mathbf{u} = [u(\mathbf{r}_1, t_1), \cdots, u(\mathbf{r}_M, t_1), \cdots, u(\mathbf{r}_M, t_N)]. \tag{3.8}$$

Because these measurements have relatively low photon counts, these data are subject to Poisson noise.

The inverse problem seeks to reconstruct $S(\mathbf{r}, t)$ appearing in (3.1) from the set of noisy measurements in $\mathbf{u}$. Because the optical properties of the medium are assumed known, this inverse problem is a linear, inverse source problem. Nonetheless, it is severely ill-posed. We propose the following two-stage method for reconstructing the sources.

1. Assuming a sparse distribution of sources that does not change over $[0, T]$, we apply SPIRAL-ℓ_p, a nonconvex, sparsity promoting optimization method (see Section 2.3.1 for more details), to determine the spatial support of the sources from the time-averaged data (3.19).

2. Using the determined support of the sources from Step 1, we recover the characteristic time of decay for each of the sources.

In what follows, we give the details for this two-stage reconstruction method and then show results from numerical simulations to evaluate its effectiveness in solving this problem.

3.2.2 Methodology

Finite difference discretization

We solve the initial-boundary value problem (3.1) subject to the initial condition (3.12) and the boundary condition (3.3) using the Crank-Nicolson method

[86]. We discretize the spatial domain Ω with a 2D spatial grid of the form $x_i = i\Delta x$ and $y_j = j\Delta y$ for $i = 0, \ldots, N_x, j = 0, \ldots, N_y$. We also discretize the temporal domain $[0, T]$ into N equally spaced intervals of length Δt. We let the vector $\mathbf{V}^{\tilde{N}}$ have entries $(V_{0,0}^{\tilde{N}}, V_{1,0}^{\tilde{N}}, \ldots, V_{N_x-1,N_y-1}^{\tilde{N}})$, where $V_{i,j}^{\tilde{N}} \approx \phi(x_i, y_j, \tilde{N}\Delta t)$ and $1 \leq \tilde{N} < N$. Similarly, we let the vector $\mathbf{S}^{\tilde{N}} = (S_{0,0}^{\tilde{N}}, S_{1,0}^{\tilde{N}}, \ldots, S_{N_x-1,N_y-1}^{\tilde{N}})$, where $S_{i,j}^{\tilde{N}} = S(x_i, y_j, \tilde{N}\Delta t)$. Then the Crank-Nicolson method leads to a linear model at time $\tilde{N}\Delta t$ in the form

$$\mathbf{L}^- \mathbf{V}^{\tilde{N}+1} - \mathbf{L}^+ \mathbf{V}^{\tilde{N}} = \tilde{\mathbf{S}}^{\tilde{N}+1}, \tag{3.9}$$

where

$$\mathbf{L}^- = \left(1 + \frac{c\mu_a \Delta t}{2}\right) \mathbf{I} - \mathbf{L}_b,$$

$$\mathbf{L}^+ = \left(1 - \frac{c\mu_a \Delta t}{2}\right) \mathbf{I} + \mathbf{L}_b,$$

and

$$\tilde{\mathbf{S}}^{\tilde{N}+1} = (\mathbf{S}^{\tilde{N}+1} + \mathbf{S}^{\tilde{N}})\frac{c\Delta t}{2}.$$

Here, $\mathbf{L}_b$ is the $N_x N_y \times N_x N_y$ finite difference operator given by

$$\mathbf{L}_b \mathbf{V}^{\tilde{N}} = \frac{c\kappa\Delta t}{2\Delta x^2}(V_{i-1,j}^{\tilde{N}} - 2V_{i,j}^{\tilde{N}} + V_{i+1,j}^{\tilde{N}}) + \frac{c\kappa\Delta t}{2\Delta y^2}(V_{i,j-1}^{\tilde{N}} - 2V_{i,j}^{\tilde{N}} + V_{i,j+1}^{\tilde{N}}).$$

For all time levels, (3.9) can be written as a system of linear equations of the form

$$\underbrace{\begin{bmatrix} \mathbf{L}^- & 0 & \cdots & 0 \\ -\mathbf{L}^+ & \mathbf{L}^- & \ddots & \vdots \\ 0 & \ddots & \ddots & 0 \\ 0 & 0 & -\mathbf{L}^+ & \mathbf{L}^- \end{bmatrix}}_{\mathbf{L}} \underbrace{\begin{bmatrix} \mathbf{V}^1 \\ \mathbf{V}^2 \\ \vdots \\ \mathbf{V}^N \end{bmatrix}}_{\mathbf{V}} = \underbrace{\begin{bmatrix} \tilde{\mathbf{S}}^1 \\ \tilde{\mathbf{S}}^2 \\ \vdots \\ \tilde{\mathbf{S}}^N \end{bmatrix}}_{\tilde{\mathbf{S}}},$$

where $\mathbf{L}$ is a sparse lower triangular block matrix of size $NN_x N_y \times NN_x N_y$, containing $\mathbf{L}^-$ and $\mathbf{L}^+$. As defined in (3.4), in the discrete setting, time-dependent measurements are obtained by restricting the numerical solution $\mathbf{V}$ at the boundary:

$$\mathbf{u} = \frac{1}{2}\mathbf{R}\mathbf{V} = \frac{1}{2}\mathbf{R}\mathbf{L}^{-1}\tilde{\mathbf{S}},$$

where boundary restriction operator $\mathbf{R}$ is a sparse matrix of size $MN \times NN_xN_y$ and $\frac{1}{2}\mathbf{R}\mathbf{L}^{-1}$ is defined as the system matrix $\mathbf{A}$. Instead of generating the system matrix $\mathbf{A}$ explicitly, we compute the action $\mathbf{A}(\mathbf{x})$ and $\mathbf{A}^T(\mathbf{x})$ on-the-fly using the forward and backward substitution techniques. Similarly, the actions of time-independent system matrix also has to be constructed to solve the steady-state boundary value problem in (3.6) and (3.7). Next we briefly recall our sparsity-promoting nonconvex optimization technique from Section 2.3.1 to recover interior sources.

Poisson intensity reconstruction

The arrival of photons at the detector is typically modeled by the Poisson noise model [113]:

$$\mathbf{y} \sim \text{Poisson}(\mathbf{A}\mathbf{f}^*),$$

where $\mathbf{y} \in \mathbb{Z}_+^m$ is a vector of observed photon counts, $\mathbf{f}^* \in \mathbb{R}_+^n$ is the vector of true signal intensity, and $\mathbf{A} \in \mathbb{R}_+^{m \times n}$ is the system matrix. Therefore, the nonconvex Poisson reconstruction problem has the following constrained optimization form:

$$
\begin{aligned}
\underset{\mathbf{f} \in \mathbb{R}^n}{\text{minimize}} \quad & F(\mathbf{f}) + \tau \, \|\mathbf{f}\|_p^p \\
\text{subject to} \quad & \mathbf{f} \succeq 0,
\end{aligned}
\tag{3.10}
$$

where $F(\mathbf{f})$ is the negative Poisson log-likelihood function (1.9):

$$F(\mathbf{f}) = \mathbf{1}^T\mathbf{A}\mathbf{f} - \sum_{i=1}^{m} y_i \, \log(\mathbf{e}_i^T\mathbf{A}\mathbf{f} + \beta).$$

We solve (3.10) using the SPIRAL-ℓ_p approach proposed in [5], which was described in detail in Sections 2.3.1 and 2.3.2.

Computational details

As we explained in inverse problem, our proposed method consists of two steps. In Step 1, we set the time-averaged measurements $\bar{\mathbf{u}}$ as the observation vector $\mathbf{y}$ of SPIRAL-ℓ_p algorithm, i.e., $\mathbf{y} = \bar{\mathbf{u}}$, while in Step 2, we set $\mathbf{y} = \mathbf{u}$. Similarly, the true signal $\mathbf{f}^*$ of SPIRAL-ℓ_p is set to the time-averaged $\tilde{\mathbf{S}}$ in Step 1, while $\mathbf{f}^*$ is $\tilde{\mathbf{S}}$ in Step 2. Note that the relevant system matrix also needs to be defined similarly according to each step.
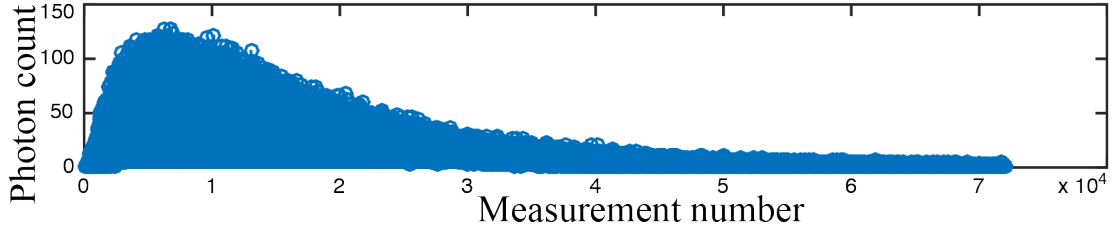
Figure 3.5: Time-dependent measurements **u** corrupted by 15% Poisson noise.

3.2.3 Numerical Results

We apply the proposed two-stage method for two 2D bioluminescence tomography problems. For the MATLAB simulations, we used the following optical properties: the absorption coefficient $\mu_a = 0.02$ and the diffusion coefficient $\kappa = 0.22$ [21]. We set $\Omega = (0,1) \times (0,1)$. Although this domain is considered to be small for the physical problem, it is sufficient to test and evaluate the method presented here. For both experiments, $N_x = N_y = 21$ and collected $N = 1000$ samples from $M = 72$ boundary detectors with sampling rate $\Delta t = 0.01$. Also, the decay rate of sources are set to 1.5. The simulated boundary measurements are corrupted by Poisson noise using the MATLAB's `poissrnd` function. The noise level (%) is computed as $100 \cdot \|\mathbf{A}\mathbf{f}^* - \mathbf{y}\|_2 / \|\mathbf{y}\|_2$. The SPIRAL-$\ell_p$ algorithm is initialized using $\mathbf{A}^T\mathbf{y}$ and terminates if the relative difference between consecutive iterates converged to $\|\mathbf{f}^{k+1} - \mathbf{f}^k\|_2 / \|\mathbf{f}^k\|_2 \leq 10^{-8}$. The regularization parameters (τ) for both experiments are manually optimized to get the minimum RMSE (RMSE (%) $= 100 \cdot \|\hat{\mathbf{f}} - \mathbf{f}^*\|_2 / \|\mathbf{f}^*\|_2$).

We are unaware of any other open source methods for solving time-dependent photon-limited bioluminescence problems, and thus, we do not present any comparisons with other methods.

Experiment 1

In this experiment, we wish to recover two bioluminescent point sources contained in the medium from approximately 15% Poisson noise corrupted time-dependent boundary measurements (see Fig. 3.5). In the first step of our proposed method, we obtained the time-averaged measurements $\bar{\mathbf{u}}$ (see Fig. 3.6) and
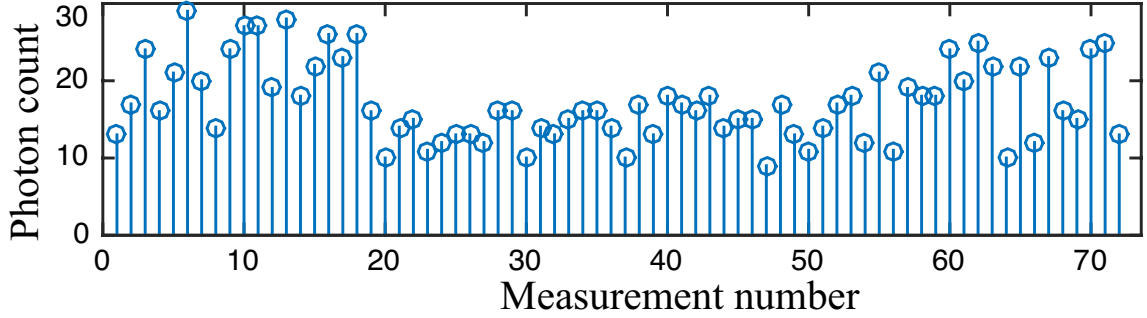
Figure 3.6: Time-averaged measurements $\bar{\mathbf{u}}$ at the 72 boundary detectors.

recovered the two locations accurately by solving the steady-state inverse problem using the SPIRAL-ℓ_p algorithm (see Fig. 3.7). Using the identified support in Fig. 3.7(b) and the time-dependent boundary measurements $\mathbf{u}$ in Fig. 3.5, we approximated the bioluminescent source intensities in space-time (see Fig. 3.8) by solving the time-dependent inverse problem using the SPIRAL-ℓ_1 approach. Specifically, since we have already identified the support for this intensity reconstruction, we use the ℓ_1-penalized SPIRAL without regularization (i.e., we set $\tau < \varepsilon$, where ε is machine precision) to reconstruct $\tilde{\mathbf{S}}$.
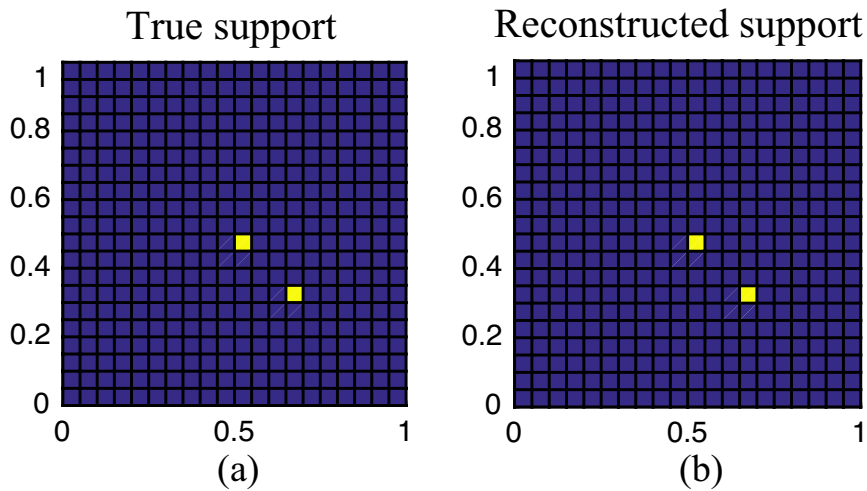
Figure 3.7: Spatial support of the point sources from the time-averaged data in Fig. 3.6. (a) True locations of the sources, (b) SPIRAL-$\ell_p(p = 0.5)$ reconstructed support. Note the SPIRAL-ℓ_p method recovered the true support accurately.
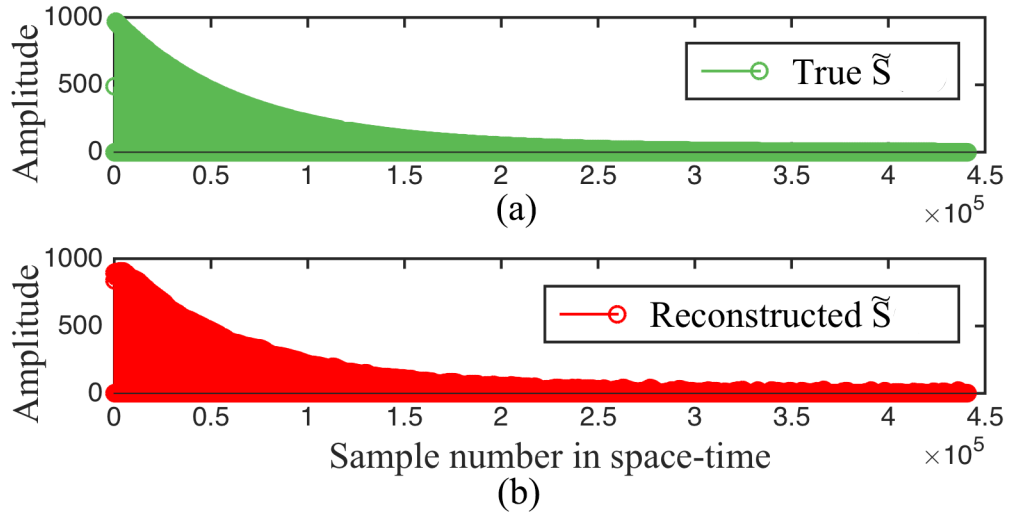
Figure 3.8: (a) The true source intensities in space-time, (b) Reconstructed source intensities in space-time with RMSE = 5.63%. RMSE (%) = $100 \cdot \|\hat{\mathbf{f}} - \mathbf{f}^*\|_2 / \|\mathbf{f}^*\|_2$.

The decay rate for two point sources is computed by plotting the maximum intensity reconstruction of each time step in Fig. 3.8(b) over the time in semi-log scale (see Fig. 3.9). In particular, the decay rate is approximated by the negative reciprocal of the slope of the linear fit (represented by the orange line in Fig. 3.9) to the reconstruction (represented in red). In this experiment, the decay rate is approximately 1.54, while the true rate is 1.5.
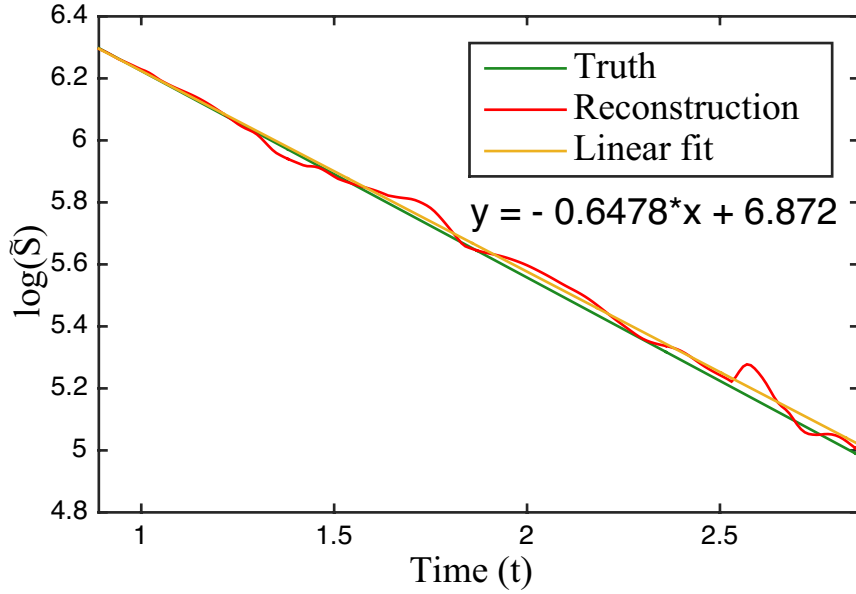
Figure 3.9: Approximation of the decay rate of the two point sources. The estimated decay rate using a linear fit to the reconstruction is 1.54, while the true decay rate is 1.50. The decay rate is equal to the negative reciprocal of the slope of the curve in semi-log scale and the half-life period from the peak time-dependent measurement is used as the time window.

Experiment 2

In this experiment, we wish to recover the support and the decay rate of two islands of pixels (see Fig. 3.10(a)) using 5% Poisson noise corrupted time-dependent measurements. By following the same approach as explained in Experiment 1, SPIRAL-ℓ_p identified the support of the sources (see Fig. 3.10(b)) with one spurious location (see the red box in Fig. 3.10(b)). To identify the support more accurately, we lowered the value of p from Experiment 1 to $p = 0.3$.

We used the recovered support (including the spurious location in Fig. 3.10(b)) to approximate the decay rate of the group of sources. Using a linear fit to the log of the intensity reconstruction (see Fig. 3.11), we estimated the decay rate to be 1.53, while the true decay rate is 1.50.
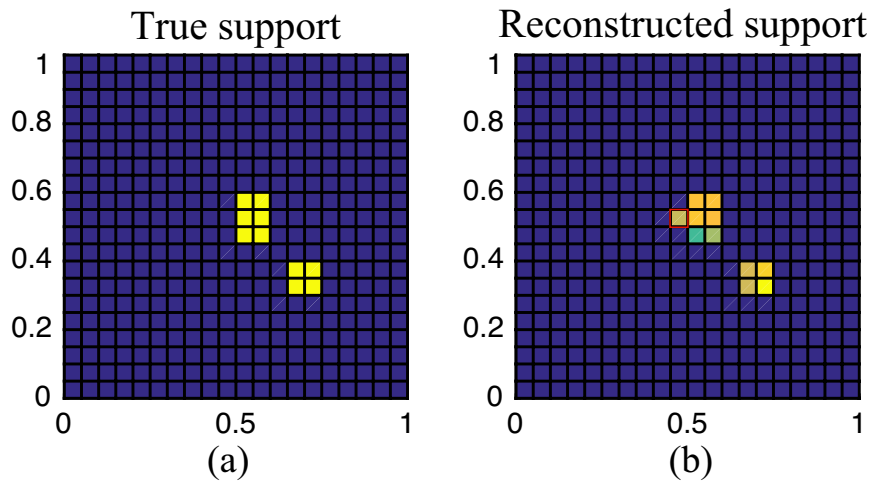
Figure 3.10: Spatial support of the two group of sources from the time-averaged data. (a) True locations of the sources, (b) SPIRAL-$\ell_p(p = 0.3)$ reconstructed support. Note that there is a spurious support in the reconstruction which is marked by red color box.
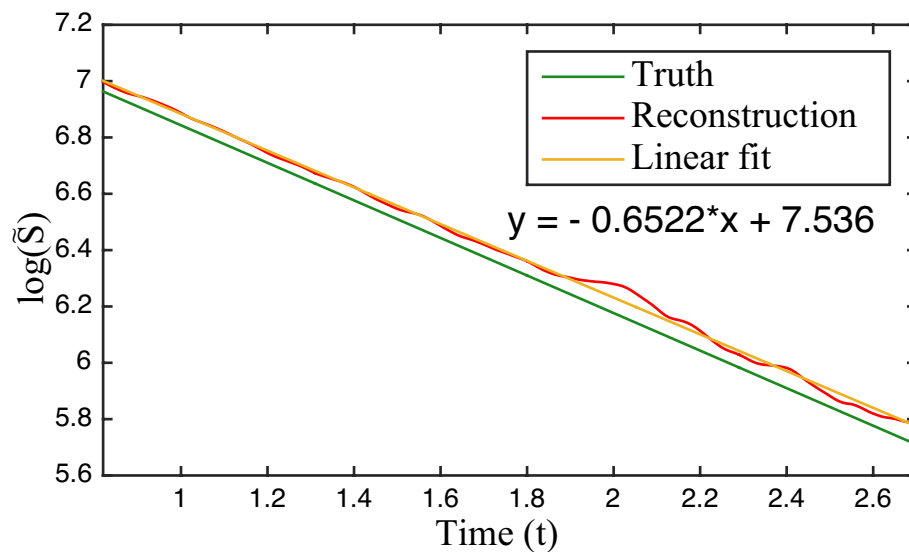
Figure 3.11: Decay rate of the two group of interior sources. Approximated decay rate through a linear fit to the reconstruction is 1.53, while the true decay rate is 1.50. The decay rate is equal to the negative reciprocal of the slope of the curve in semi-log scale and the half-life period from the peak time-dependent measurement is used as the time window.

3.2.4 Conclusion

We proposed a novel two-stage method to recover time-dependent bioluminescent sources from Poisson noise corrupted boundary measurements. Unlike previous methods, the first stage of our approach uses a nonconvex sparse Poisson intensity reconstruction method (SPIRAL-ℓ_p) to recover the support of the bioluminescent sources using the time-averaged data. In the second stage, we use the determined support of the sources to recover the characteristic time decay using the time-dependent data. Numerical experiments show that the proposed two-stage reconstruction method accurately solves this time-dependent bioluminescence problem. Furthermore, while this approach is efficient for small scale problems, it can be parallelized for large-scale problems.

3.3 Time-Dependent Fluorescence Lifetime Tomography

The work describes in this section is based on the paper by Adhikari et al. [3]. Fluorescence microscopy provides the ability to study *in vivo* cellular and molecular dynamics in real time, because of its sensitivity, specificity, and versatility [122]. In particular, fluorescence lifetime imaging (FLIM) is becoming increasingly important. The lifetime of a fluorophore provides useful information about the local environment (pH, ion, or oxygen concentration), but not on the local fluorophore concentration or absorption in the sample, etc [122, 76].

In fluorescence lifetime imaging, one seeks to reconstruct the spatial distribution of the fluorescence decay rates within the tissue sample. Typically, this spatial distribution is sparse. Consequently, there have been several recent studies that employed sparsity-promoting methods to solve this FLIM problem. However, these methods minimize the least-squares cost functional with Gaussian noise, *e.g.* [10, 31]. Implicitly, these studies assume that there is enough signal in the measurements made by photon counting detectors that Gaussian noise is a valid assumption. In contrast, we consider here time-dependent measurements with rela-

tively low photon counts. For that case, we must consider measurements corrupted by Poisson noise [13]. To do so, we use the nonconvex Sparse Poisson Intensity Reconstruction ALgorithm (SPIRAL-ℓ_p) [5] to minimize the ℓ_p-norm penalized negative Poisson log-likelihood function. We show that this approach applied to the time-averaged data provides an effective method for reconstructing the spatial support of the fluorophores. Upon determining these supports, we recover the fluorescence decay rates from the time-dependent data. Using numerical simulations, we show that this reconstruction method effectively solves this time-dependent FLIM problem.

3.3.1   Problem Formulation

For the fluorescence-lifetime imaging problem, we seek to reconstruct the fluorophore concentration along with the support and fluorescence-lifetime from the time-dependent measurements of emitted light due to pulsed excitation of a strongly scattering medium. We assume that the optical properties of the medium are known to reasonable precision. In what follows, we describe the forward model and then the corresponding inverse problem for this fluorescence-lifetime imaging problem.

Forward model: Let Ω denote the domain with boundary $\partial\Omega$. A pulse of exciting light is injected into Ω on $\partial\Omega$. Let $S(\mathbf{r}, t)$ for $\mathbf{r} \in \partial\Omega$ and $t > 0$ denote that exterior time-dependent source of exciting light. Let $I^e(\mathbf{r}, t)$ denotes the intensity of this exciting light source at position $\mathbf{r} \in \Omega$ at time $t \in [0, T]$. It is governed by the following initial-boundary value problem for the diffusion approximation [131, 12]:

$$\frac{1}{c}\frac{\partial I^e}{\partial t} - \nabla \cdot (\kappa^e \nabla I^e) + \mu_a^e I^e = 0 \quad \text{in } \Omega \times (0, T], \tag{3.11}$$

with κ^e denoting the diffusion coefficient and μ_a^e denoting the absorption coefficient at the exciting wavelength. We solve (3.11) subject to initial condition

$$I^e(\mathbf{r}, 0) = 0 \quad \text{in } \Omega, \tag{3.12}$$

and boundary condition

$$I^e + \alpha^e \kappa^e \frac{\partial I^e}{\partial n} = \begin{cases} \gamma^e S(\mathbf{r}, t) & \text{on } \mathbf{r} \in \mathbf{r}_s \\ 0 & \text{on } \mathbf{r} \in \partial\Omega \backslash \mathbf{r}_s \end{cases} \tag{3.13}$$

Here, $\partial I^e / \partial n$ denotes the outward normal derivative of I^e, constants α^e and γ^e are defined in terms of μ_a^e and κ^e as part of the diffusion approximation and $\mathbf{r}_s$ denotes the source location at the boundary.

Next, we consider that a portion of I^e is absorbed by the fluorophores and re-emitted. The transportation of emitted light I^f is then modeled by

$$\frac{1}{c} \frac{\partial I^f}{\partial t} - \nabla \cdot (\kappa^f \nabla I^f) + \mu_a^f I^f = Q(\mathbf{r}, t) \quad \text{in } \Omega \times (0, T], \tag{3.14}$$

with κ^f denoting the diffusion coefficient and μ_a^f denoting the absorption coefficient at the exciting wavelength. Here, the emission of fluorescent light is due to the excited interior source [13],

$$Q(\mathbf{r}, t) = \chi(\mathbf{r}) h(\mathbf{r}) \int_0^t e^{-(t-t')/\tau(\mathbf{r})} I^e(\mathbf{r}, t') dt', \tag{3.15}$$

where $\chi(\mathbf{r})$ is the indicator function, $h(\mathbf{r})$ is the fluorophore concentration, and $\tau(\mathbf{r})$ is the fluorescence-lifetime. We solve (3.14) subject to initial condition

$$I^f(\mathbf{r}, 0) = 0 \quad \text{in } \Omega, \tag{3.16}$$

and boundary condition

$$I^f + \alpha^f \kappa^f \frac{\partial I^f}{\partial n} = 0 \quad \text{on } \partial\Omega. \tag{3.17}$$

Upon solution of the initial-boundary value problem for emission light consisisting of (3.14) subject to (3.16) and (3.17), we model measurements of scattered light leaving the boundary of the medium, $u(\mathbf{r}, t)$, through evaluation of

$$u(\mathbf{r}, t) = -\kappa^f \frac{\partial I^f}{\partial n} = \frac{1}{\alpha^f} I^f \quad \text{on } \partial\Omega \times (0, T]. \tag{3.18}$$

Note that we have substituted (3.17) into the first result of (3.18) to obtain the final result of (3.18).

Suppose we consider the time-averaged data defined as

$$\bar{u}(\mathbf{r}) = \frac{1}{\alpha^f} \bar{I}^f(\mathbf{r}) = \frac{1}{\alpha^f T} \int_0^T I^f(\mathbf{r}, t) \mathrm{d}t \quad \text{on } \partial\Omega. \tag{3.19}$$

The steady-state optical fluence rate for emission light, $\bar{I}^f$, satisfies the steady-state diffusion equation

$$-\kappa^f \nabla^2 \bar{I}^f + \mu_a \bar{I}^f = \bar{Q} \quad \text{in } \Omega, \tag{3.20}$$

subject to the boundary condition

$$\bar{I}^f + \alpha^f \kappa^f \partial_n \bar{I}^f = 0 \quad \text{on } \partial\Omega. \tag{3.21}$$

We will make use of this boundary value problem consisting of (3.20) subject to (3.21) in the analysis that follows.

Inverse problem: The measurements of the scattered light leaving the boundary of the medium are taken at M distinct locations denoted by $\mathbf{r}_m \in \partial\Omega$ for $m = 1, \cdots, M$. Moreover, N samples of these measurements in time are collected with sampling rate, Δt with $T = N\Delta t$. The observed collection of data is given by the vector $\mathbf{u} \in \mathbb{R}^{MN}$ with $\mathbf{u} = [u(\mathbf{r}_1, t_1), \cdots, u(\mathbf{r}_M, t_1), u(\mathbf{r}_1, t_2), \cdots, u(\mathbf{r}_M, t_N)]$. Because these measurements have relatively low photon counts, we model the noise in the data using Poisson statistics.

The inverse problem seeks to reconstruct the sparse spatial distribution of fluorescence lifetime appearing in (3.15) from the set of noisy measurements in $\mathbf{u}$. We assume that the fluorophores are concentrated only in a small area. Furthermore, we assume that the optical properties of the medium for excitation and emission are known, i.e., $\kappa^e, \kappa^f, \mu_a^e$, and μ_a^f are known. Therefore, this inverse problem is linear. However, the problem is ill-posed. Hence, we include a regularization term that promotes sparsity in the solution. We propose the following three-stage method for reconstructing the fluorescence sources:

Step 1: Assuming a sparse distribution of fluorescence sources that does not change over $[0, T]$, we apply SPIRAL-ℓ_p [5], a nonconvex, sparsity promoting optimization method (see Section 2.3.1), to determine the spatial support, $\chi(\mathbf{r})$ of the sources from the time-averaged data in (3.19).

Step 2: Using the determined support $\chi(\mathbf{r})$ of the sources from Step 1, we apply SPIRAL-ℓ_1 [70] to determin $Q(\mathbf{r}, t)$ from the time-dependent measurements. Since we have identified the support in Step 1 and therefore no longer need to promote sparsity in the solution, we use SPIRAL-ℓ_1 with a negligible regularization penalty parameter.

Step 3: Using $\chi(\mathbf{r})$ and $Q(\mathbf{r}, t)$ from Steps 1 and 2, we apply a nonlinear least squares solver to recover the fluorophore concentration $h(\mathbf{r})$ and the lifetime $\tau(\mathbf{r})$ from (3.15).

Previous work for solving Poisson inverse problems include statistical multiscale modeling and analysis frameworks [97], nonparametric estimators using wavelet decompositions [11], and combination expectation-maximization algorithms with a total variation-based regularization [105]. Our proposed approach uses a sequence of separable approximations to the objective function with non-convex p-norm regularization to identify the support of the time-dependent fluorescence sources and to recover their lifetime parameters.

3.3.2 Methodology

Finite difference discretization: Both initial-boundary value problems (3.11) and (3.14) subject to the initial and boundary conditions ((3.12), (3.13) and (3.16), (3.17) respectively) are solved using the Crank-Nicolson method [86]. As defined in (3.18), in the discrete setting, the measurements are obtained by restricting the numerical solution of emission light, say $\mathbf{V}$, to the boundary:

$$\mathbf{u} = \frac{1}{\alpha^f} \mathbf{R} \mathbf{V} = \frac{1}{\alpha^f} \mathbf{R} \mathbf{L}^{-1} \tilde{\mathbf{Q}}, \tag{3.22}$$

where $\mathbf{R}$ is a boundary restriction operator, $\mathbf{L}$ is the finite difference operator and $\tilde{\mathbf{Q}}$ is averaged Q between consecutive time steps. More over, $\frac{1}{\alpha^f}\mathbf{R}\mathbf{L}^{-1}$ is defined as the system matrix $\mathbf{A}$ for the inverse algorithm. Instead of generating the system matrix $\mathbf{A}$ explicitly, we compute the action $\mathbf{A}(\mathbf{x})$ and $\mathbf{A}^T(\mathbf{x})$ on-the-fly using the forward and backward substitution techniques. Similarly, actions of the steady-state boundary value problem in (3.20) and (3.21) also have to be constructed in a similar technique.

Poisson intensity reconstruction: The arrival of photons at a detector is typically modeled by a Poisson noise model [113], $\mathbf{y} \sim \mathrm{Poisson}(\mathbf{A}\mathbf{f}^*)$, where $\mathbf{y} \in \mathbb{Z}_+^m$ is the vector of observed photon counts, $\mathbf{f}^* \in \mathbb{R}_+^n$ is the vector of true signal intensity, and $\mathbf{A} \in \mathbb{R}_+^{m \times n}$ is the system matrix. The negative Poisson log-likelihood function (1.9) corresponding to observing $\mathbf{y}$ given $\mathbf{A}\mathbf{f}$ is given by

$$F(\mathbf{f}) = \mathbf{1}^T \mathbf{A}\mathbf{f} - \sum_{i=1}^m y_i \, \log(\mathbf{e}_i^T \mathbf{A}\mathbf{f}).$$

We formulate our Poisson reconstruction problem as the following constrained optimization problem:

$$
\begin{aligned}
\hat{\mathbf{f}} \quad = \quad & \underset{f \in \mathbb{R}^n}{\arg\min} \quad \Phi(\mathbf{f}) \equiv F(\mathbf{f}) + \beta \, \|\mathbf{f}\|_p^p \\
& \text{subject to} \quad \mathbf{f} \succeq 0.
\end{aligned}
\tag{3.23}
$$

where $\|\mathbf{f}\|_p^p$ ($0 \le p < 1$) is a penalty function that promotes sparsity in our solution and $\beta > 0$ is a scalar regularization parameter. The nonnegativity constraint on $\mathbf{f}$ ensures that the solution, which corresponds to the fluorescence sources, is nonnegative. Our optimization problem formulation is different from the more commonly used least-squares minimization problem [13] in three ways: (1) instead of a least-squares data-fidelity term, we use a negative log-likelihood function to model the noise statistics more accurately; (2) instead of a Tikhonov regularization or a sparsity-promoting ℓ_1-norm, we use a non-convex p-norm, where $0 \le p < 1$, to bridge the convex ℓ_1-norm and the ℓ_0 counting semi-norm; and (3) we enforce a nonnegativity constraint on our solution. We solve the minimization problem (3.23) using the SPIRAL-ℓ_p approach (see Section 2.3.1 for further details).

3.3.3 Numerical Experiments
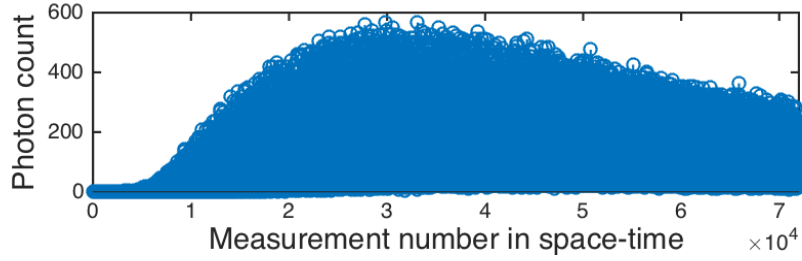
(a)
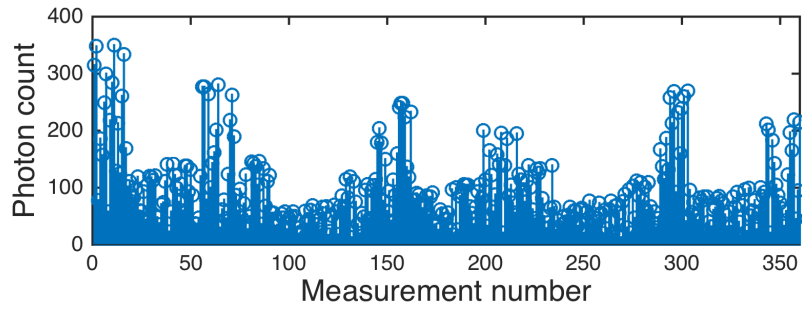
(b)

Figure 3.12: Measurements for Experiment 1: (a) Time-dependent measurements **u** corrupted by 7.5% Poisson noise, (b) Time-averaged measurements **ū** at the 360 boundary detectors (72 detectors per one exterior source).
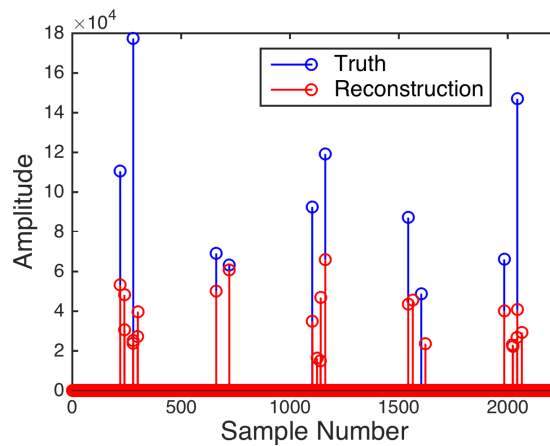
Figure 3.13: Support reconstruction for Experiment 1 for all 5 sources using SPIRAL-ℓ_p method ($p = 0.3$) in stage 1 of our proposed method. Here, RMSE = 0.79 and 23 nonzero components are in the reconstruction.

We apply the proposed three-stage reconstruction method to solve 2D fluorescence lifetime imaging problem. For the MATLAB simulations, we used a unit square domain $\Omega = (0,1) \times (0,1)$ with the following non-dimensionalized optical properties: the absorption coefficient $\mu_a = 0.05$ and the diffusion coefficient $\kappa = 0.0476$ [10]. For all experiments, $N = 200$ time-level samples from $M = 72$ boundary detectors with sampling rate $\Delta t = 0.05$ are colloected using 5 exterior near-infrared source points. Also, the fluorescence-lifetime and the fluorophore concentration are set to 5.7 and 2000, respectively [123]. The simulated boundary measurements are corrupted by Poisson noise using the MATLAB's `poissrnd` function. The noise level (%) is computed as $100 \cdot \|\mathbf{A}\mathbf{f}^* - \mathbf{y}\|_2/\|\mathbf{y}\|_2$. The SPIRAL-$\ell_p$ and SPIRAL-ℓ_1 algorithms in stage (1) and (2) are initialized using $\mathbf{A}^T\mathbf{y}$ and terminate if the relative objective values do not significantly change, i.e., $|\Phi(\mathbf{f}^{k+1}) - \Phi(\mathbf{f}^k)|/|\Phi(\mathbf{f}^k)| \leq 10^{-7}$. The regularization parameters (β) for both experiments are manually optimized to get the minimum RMSE (RMSE (%) $= 100 \cdot \|\hat{\mathbf{f}} - \mathbf{f}^*\|_2/\|\mathbf{f}^*\|_2$, where $\hat{\mathbf{f}}$ is an estimate of $\mathbf{f}^*$). Next we show numerical results for two experiments: two point source and two island source reconstruction.

(a) True support

(b) SPIRAL-$\ell_p(p = 0.3)$ Support

(c) SPIRAL-ℓ_1 Support
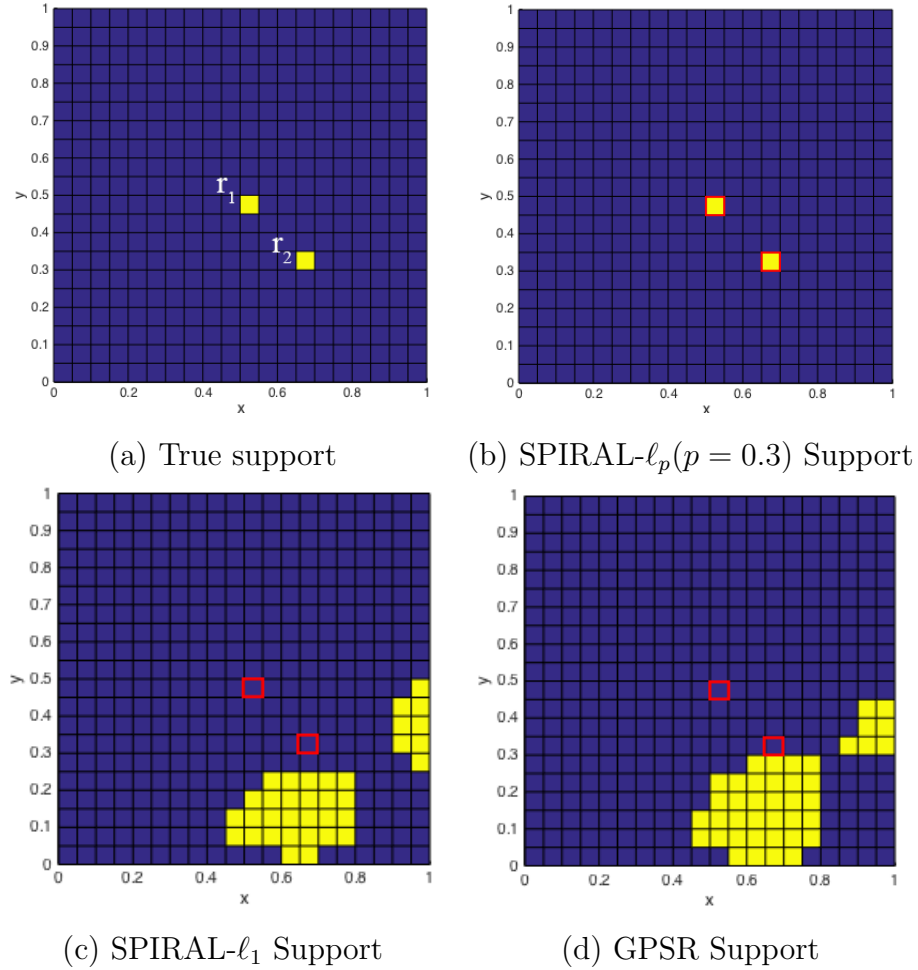
(d) GPSR Support

Figure 3.14: (a) True fluorophore locations in the 2D grid. (b) Final reconstructed support of the fluorophore by thresholding and computing the mode of the results in Fig. 3.13. (c) SPIRAL-ℓ_1 support reconstruction. (d) GPSR support reconstruction. Note the reconstructed support from existing methods in (c) and (d) are very inaccurate.

Here, we consider two experiments. Experiment 1 consists of a fluorescence reconstruction problem with two fluorophore point sources (see Fig. 3.14(a)) while Experiment 2 consists of two islands of fluorophore sources (see Fig. 3.16(a)). The observations $\mathbf{u}$ are time dependent and are corrupted by Poisson noise (see e.g., Fig. 3.12(a)). Step 1 of our proposed method uses the time-averaged measurements $\bar{\mathbf{u}}$ (see e.g., Fig. 3.12(b)) to obtain an estimate for the support of the fluorophores for all 5 exterior sources (see e.g., Fig. 3.13). The final reconstructed support
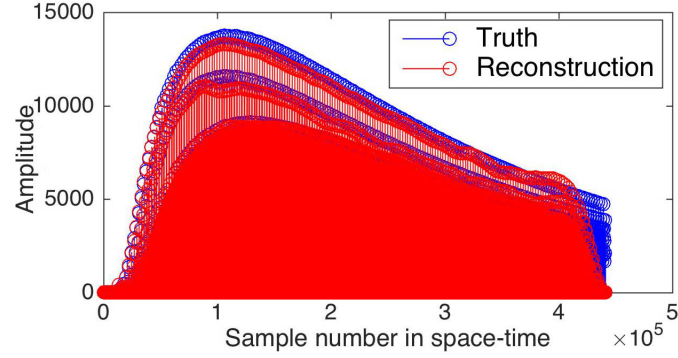
Figure 3.15: Experiment 1 SPIRAL-ℓ_1 reconstruction of $\tilde{\mathbf{Q}}$ with the given reconstructed support in Fig. 3.14(b). RMSE of the reconstruction is 0.108.

of the fluorophores is obtained by thresholding and computing the mode of the SPIRAL-ℓ_p reconstruction since the location of the fluorophores must be the same for each source (see Figs. 3.14(b) and 3.16(b)). Then given the estimated support from Step 1, in Step 2 we reconstructed $\tilde{\mathbf{Q}}$ in (3.22) using SPIRAL-ℓ_1 with negligible regularization since we already identified the support and no longer need to promote sparsity in the solution (see e.g., Fig. 3.15). In Step 3, we used the built-in Matlab nonlinear least-squares command `lsqnonlin` to compute the estimate $\hat{h}$ at the two source locations using the initial concentration value $\hat{h}_0 = 1.0$ for both locations and initial fluorescence lifetime value $\hat{\tau}_0 = 1.0$. Results are presented in Tables 3.3 and 3.4.

	Ground Truth	Estimate
$h(r_1)$	2.00×10^3	2.07×10^3
$h(r_2)$	2.00×10^3	1.95×10^3
τ	5.70	5.64

Table 3.3: A comparison between the true and the computed fluorophore concentrations, h, at point locations r_1 and r_2 and between the true and computed fluorescence lifetimes, τ for Experiment 1.

(a) True support

(b) SPIRAL-ℓ_p support

(c) SPIRAL-ℓ_1 support
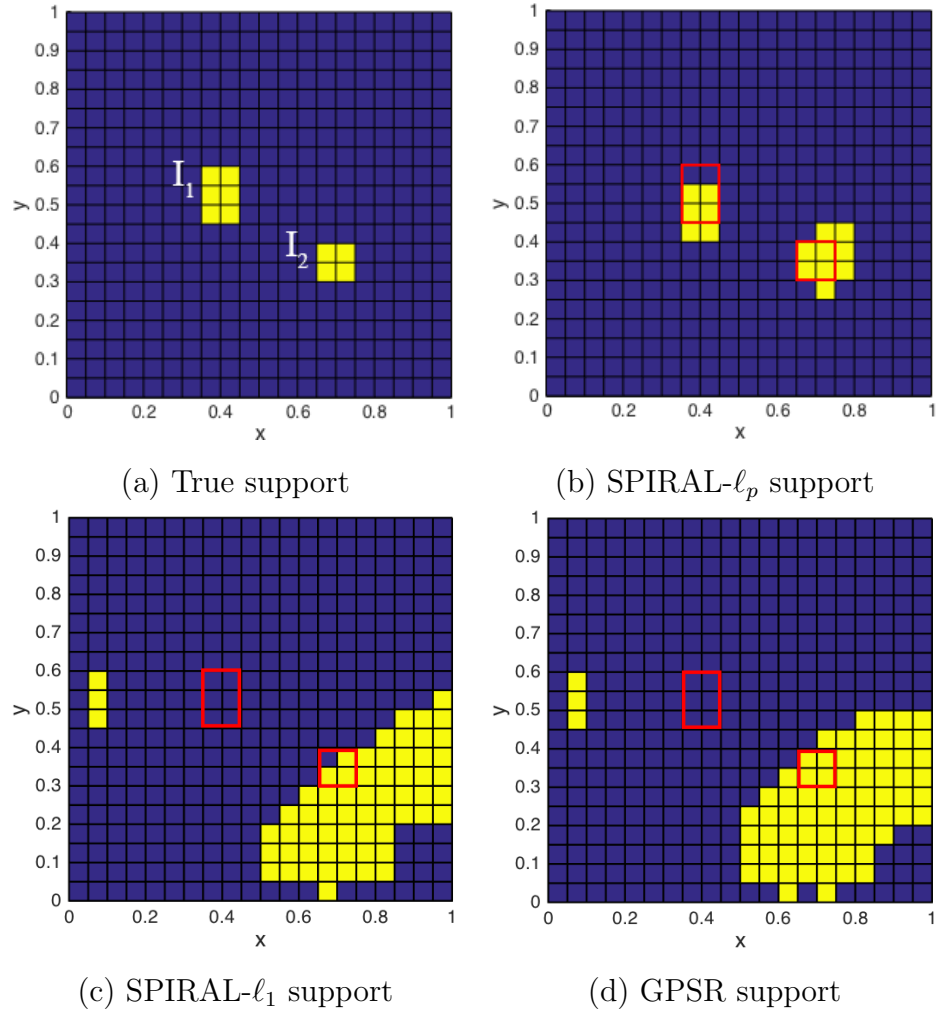
(d) GPSR support

Figure 3.16: (a) True fluorophore islands in the 2D grid. (b) Reconstructed support of the fluorophore by thresholding and computing the mode of the SPIRAL-ℓ_p ($p = 0.1$) reconstruction. (c) SPIRAL-ℓ_1 support reconstruction. (d) GPSR support reconstruction. Note the reconstructed islands from existing methods in (c) and (d) are very inaccurate.

3.3.4 Conclusion

We proposed a novel three-stage method to solve the fluorescence lifetime imaging problem from Poisson noise corrupted boundary measurements. For this imaging problem, measured signals are modeled by solutions of a coupled initial-boundary value problem for light scattering and absorption inside the sample.

	Ground Truth	Range of Estimate
$h(I_1)$	2.00×10^3	1.29×10^3 to 2.72×10^3
$h(I_2)$	2.00×10^3	0.58×10^3 to 0.95×10^3
τ	5.70	5.76

Table 3.4: A comparison between the true and the computed fluorophore concentrations, h, at islands I_1 and I_2 and between the true and computed fluorescence lifetimes, τ, for Experiment 2.

Furthermore, unlike previous methods, Poisson noise is explicitly modeled in the inverse problem and a nonconvex sparse recovery method (SPIRAL-ℓ_p) is used to determine the support of the fluorophores. Numerical experiments demonstrate that the proposed method accurately solves the FLIM problem than the existing methods.

3.4 Inferring Structural Variants from Sequencing Data

In this section, I briefly discuss my work on sparse recovery methods for structural variant detection in collaboration with the Sindi Lab at UC Merced. In particular, the work discribed here is based on conference proceeding papers co-authored with the Sindi Lab, [18, 19, 17], summarized with the explicit permission of Mario Banuelos and Prof. Suzanne Sindi.

Structural variants (SVs) are rearrangements of DNA sequences. SVs typically consist of many kinds of variation in genome such as inversions, insertions, deletions, and duplications (see Fig. 3.17). These structural variations make an important contribution to human diversity through complex traits such as behaviors and to disease traits such as Mendelian diseases [116, 110]. SVs are typically predicted by sequencing fragments from an unknown individual genome and mapping those fragments to a previously identified reference genome [92, 111]. If the starting points of the genomic fragments are chosen uniformly and randomly from the genome, then the expected number of fragments covering any position in the

(a) No Variant   (b) Deletion

(c) Inversion   (d) Novel Insertion
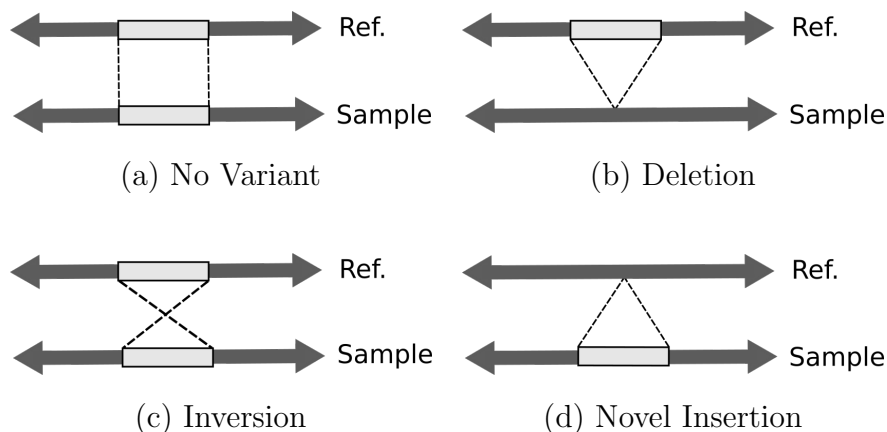
Figure 3.17: Different structural variations in a sample genome in comparison to the reference genome. Image courtesy of Mario Banuelos.

genome is given by a Poisson distribution [83]. The mean of this Poisson distribution is referred to as the *coverage* of the genome. Since, in most large sequencing studies, many individuals will be sequenced at low coverage, even if an individual carries a genetic variant, we may not sample a fragment from that particular region of the genome. Similarly, if we observe a single fragment supporting a variant, it may represent an erroneous mapping rather than a true observation.

There have been many published methods to identify SVs from sequencing data (see, e.g., [109, 74, 44]). However, these approaches almost universally rely on high-coverage of a single individual genome and not on the scenario emerging from many large-scale sequencing efforts where there is low-coverage of many individuals. In addition, prior approaches when applied to populations typically consider each individual in isolation when – in fact – common variants would be shared by many individuals. Finally, most methods utilize a threshold – minimum number of supporting fragments – to prioritize predicted variants rather than a likelihood based statistic. Indeed, inferring SV information from sequencing data has proven to be challenging because true SVs are rare and are prone to low-coverage noise.

In this work, we attempt to mitigate the deleterious effects of low-coverage sequences by following a maximum likelihood approach to SV prediction. Specifically, we model the noise using Poisson statistics and constrain the solution to promote sparsity, i.e., SV instances should be rare. Further, we consider multiple

individuals and use relatedness among individuals as a constraint on the solution space – to our knowledge, this is the first SV detection algorithm to do so. Specifically, in our work below we use the assumption that a parent and child are sequenced and require that any SVs predicted in the child be present in the parent. Numerical analysis of both simulated and real sequencing data suggest that our approach has the promise to improve SV detection in studies of many low-coverage individuals.

3.4.1 Problem Formulation

We propose to model the measurements through the Poisson process and to minimize the negative Poisson log-likelihood objective function with sparsity promoting regularizer: ℓ_1-norm or ℓ_p-norm ($0 \leq p < 1$), following the SPIRAL framework [70]. For simplicity, if we have only two individuals, i.e., one parent and one child, then the Poisson noise-corrupted measurements $\mathbf{y}_p \in \mathbb{Z}_+^n$ and $\mathbf{y}_c \in \mathbb{Z}_+^n$ can be modeled as

$$
\begin{aligned}
\mathbf{y}_p &\sim \mathrm{Poisson}(\mathbf{A}_p\mathbf{f}_p^*) \\
\mathbf{y}_c &\sim \mathrm{Poisson}(\mathbf{A}_c\mathbf{f}_c^*),
\end{aligned}
$$

where $\mathbf{f}_p^*$ and $\mathbf{f}_c^*$ are the true genomic variants of n-vector of $\{0, 1\}$ for the parent and child, respectively, and

$$
\begin{aligned}
\mathbf{A}_p &= (c_p - \epsilon)\mathbf{I} \in \mathbb{R}^{n \times n} \\
\mathbf{A}_c &= (c_c - \epsilon)\mathbf{I} \in \mathbb{R}^{n \times n},
\end{aligned}
$$

where constant sequence coverages $c_p, c_c \in \mathbb{R}$ and ϵ is an error term associated with the measurements. These observations can be written in the form (1.7) by stacking the signals, that is

$$
\mathbf{y} \sim \mathbf{Poisson}(\mathbf{A}\mathbf{f}^*),
$$

where $\mathbf{y} = [\mathbf{y}_p; \mathbf{y}_c] \in \mathbb{Z}_+^{2n}$, $\mathbf{A} \in \mathbb{R}^{2n \times 2n}$ is a block-diagonal matrix with diagonal $(\mathbf{A}_p; \mathbf{A}_c)$, and $\mathbf{f}^*$ is also stacked similarly. The unknown signal $\mathbf{f}^*$ is recovered by minimizing the negative Poisson log-likelihood $F(\mathbf{f})$ as we defined in (1.9). With

additional constraints on variants, the regularized SPIRAL subproblem minimization can be written in the form:

$$\mathbf{f}^{k+1} = \arg\min_{\mathbf{f} \in \mathbb{R}^{2n}} \quad \frac{1}{2}\|\mathbf{f} - \mathbf{s}^k\|_2^2 + \frac{\tau}{\alpha_k}\text{pen}(\mathbf{f})$$

$$\text{subject to} \quad 0 \preceq \mathbf{f}_c \preceq \mathbf{f}_p \preceq 1, \tag{3.24}$$

where

$$\mathbf{s}^k = \begin{bmatrix} \mathbf{s}_p^k \\ \mathbf{s}_c^k \end{bmatrix} = \mathbf{f}^k - \frac{1}{\alpha_k}\nabla F(\mathbf{f}^k),$$

where the penalty term $\text{pen}(\mathbf{f})$ is replaced by a sparsity promoting functional, such as $\|\mathbf{f}\|_1$ or $\|\mathbf{f}\|_p^p$ $(0 \leq p < 1)$. If $\|\mathbf{f}\|_1$ is the penalty term, then (3.24) can be expanded as

$$\mathbf{f}^{k+1} = \arg\min_{\mathbf{f}_p, \mathbf{f}_c \in \mathbb{R}^n} \quad \frac{1}{2}\|\mathbf{f}_p - \mathbf{s}_p^k\|_2^2 + \frac{\tau}{\alpha_k}\|\mathbf{f}_p\|_1 + \frac{1}{2}\|\mathbf{f}_c - \mathbf{s}_c^k\|_2^2 + \frac{\tau}{\alpha_k}\|\mathbf{f}_c\|_1$$

$$\text{subject to} \quad 0 \preceq \mathbf{f}_c \preceq \mathbf{f}_p \preceq 1. \tag{3.25}$$

We can now uncouple the objective function of (3.25) to scalar minimization problems of the form

$$\min_{f_p,\, f_c \in \mathbb{R}} \quad \frac{1}{2}(f_p - s_p)^2 + \lambda|f_p| + \frac{1}{2}(f_c - s_c)^2 + \lambda|f_c|$$

$$\text{subject to} \quad 0 \leq f_c \leq f_p \leq 1, \tag{3.26}$$

where $\lambda = \tau/\alpha_k$, f_p, f_c and s_p, s_c denote elements of the vectors $\mathbf{f}_p, \mathbf{f}_c$ and $\mathbf{s}_p^k, \mathbf{s}_c^k$, respectively. The solution to (3.26) is obtained by completing the squares and projecting to the feasible region (see Fig. 2 in [18]). This problem formulation also can be extended to two-parent and one-child case using a similar approach (see e.g., [19, 17]).

3.4.2 Numerical Results

The proposed method is implemented in Matlab by following the SPIRAL framework [70]. We evaluate the effectiveness of the proposed method through numerical experiments on both simulated and real genomic data. Specifically, I have contributed on performing experiments using simulated data to demonstrate the effectiveness of the proposed method with family constraints in (3.24) over the

regular constraints model (i.e., non-negativity constraints on both parent and child signals) and the thresholded observations (generic GASV).

(a)   (b)
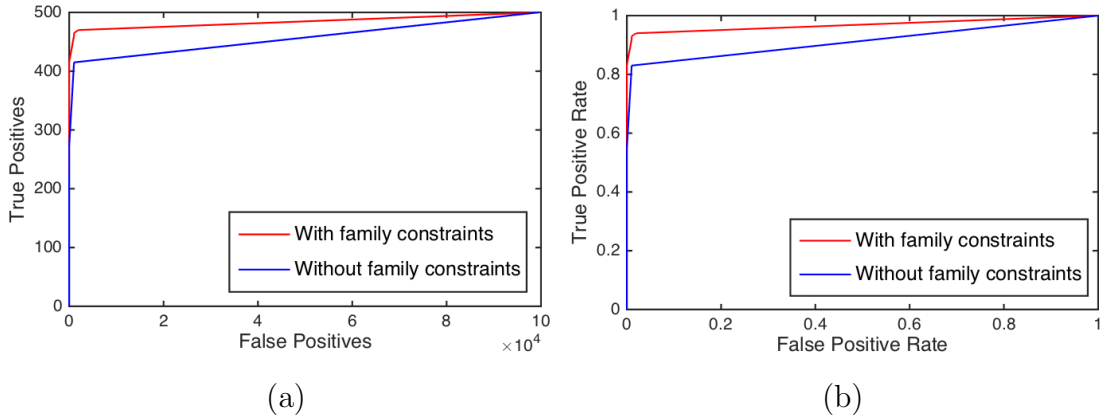
Figure 3.18: Reconstruction of the parent signal with $c_p = 2$, $c_c = 5$ and 70% similarity. (a) False positives vs. true positives in the reconstruction. (b) False positive rate vs. true positives rate of the reconstruction. Note the model with family constraints enhances the accuracy of SV detection.

We simulated both parent and child signals with length 10^5, where the child is chosen to have 70% of structural variants from the parent. In particular, 500 variants are present in the parent signal (i.e., sparsity is 0.5%), while the child has only 350 variants. We set $c_p = 2$, $c_c = 5$, and $\epsilon = 0.01$. The proposed familiarly constrained model recovers signals with high accuracy than the regular constraint method (see Figs. 3.18 (a) and (b) for true positives and true positive rates of parent signal reconstruction, respectively). We did not see any significant improvement of the regular constraint method over the simply thresholded observations with this simulated data.

3.4.3 Conclusion

This work presents a novel approach for inferring structural variants from Poisson noise-corrupted obervations. It is very challenging to accurately recovering SVs due to their scarcity and low-coverage. In this work, we explicitly model the rare occurrence of structural variants through Poisson statistics and incorporate

sparsity-inducing ℓ_1-norm penalty term for accurate recovery of sparse signals. Furthermore, we incorporate the relatedness of individuals as a constraint on the solution space. Specifically, we use the assumption that a parent and child are sequenced and require that any SVs predicted in the child be present in the parent. Moreover, if we replace the penalty term by the nonconvex ℓ_p-norm ($0 \leq p < 1$), then we can demonstrate that the solution is more accurate and sparser than the solution of ℓ_1-norm penalty functional (see [15]). Since humans are diploid – they have two copies of their genome and child receives one copy from each parent – this Poisson noise modeling method has been recently extended for sparse diploid biosignal recovery (see [16]).

3.5 Summary of Contribution

In this chapter, we investigated the effectiveness of the proposed nonconvex Poisson sparse recovery algorithms with applications. In particular, we solved the fluorescence molecular tomography problem with low photon counts using the SPIRAL-ℓ_p method. Here, we showed that the proposed nonconvex method is particularly effective in low SNR settings. More importantly, we proposed novel stage-based methods to solve time-dependent tomography problems: A two-stage method for bioluminescence tomography (BLT) and three-stage method for fluorescence lifetime imaging (FLIM) problem in low photon context. To the best of our knowledge, this is the first time to investigate time-dependent BLT and FLIM problems with Poisson noise corrupted measurements. Our proposed SV detection approaches are also the first SV detection algorithms to follow sparsity constrained Poisson log-likelihood objective function.

Chapter 4

Sparse Recovery Methods with Gaussian Noise

Sensing a sparse signal from underdetermined linear measurements is the main problem of compressed sensing. Sparse recovery is important in a variety of different applications such as medical imaging, photography, face recognition and network tomography. Basis Pursuit and the Least Absolute Shrinkage and Selection Operator (LASSO) are few popular models for sparse recovery. In this chapter, we minimize an objective function with a quadratic data-fidelity term (ℓ_2-norm) combined with a sparsity-promoting penalty function (such as ℓ_1-norm or ℓ_p-norm ($0 \leq p < 1$)). In Section 4.2, we propose to solve the $\ell_2 - \ell_1$ sparse recovery problem by transforming the objective function into an unconstrained differentiable function and applying a limited-memory trust-region method. Unlike gradient projection-type methods, which use only the current gradient, our method uses gradients from previous iterations to obtain a more accurate Hessian approximation. Moreover, we compute a global solution to the trust-region subproblem using a formula which makes use of an efficient partial spectral decomposition of the Hessian approximation via a QR factorization. In Section 4.3, we will extend this trust-region approach to solve the nonconvex $\ell_2 - \ell_p$ sparse recovery problem. Lastly, we will propose a sparsity inducing ℓ_p-norm regularized formulation for recovery and demixing problems.

.

4.1 Prior Work

In the literature, there are several types of optimization algorithms have been proposed to solve sparse recovery problems with Gaussian noise, many of them use a gradient decent-type approach. Figueiredo et al. proposed the Gradient Projection Sparse Reconstruction (GPSR) method, which is a gradient projection algorithm operates on a bound-constraints [61]. The SpaRSA is another closely related approach introduced by Wright et al. [134] to solve $\ell_2 - \ell_1$ problem, where each subproblem is constructed by approximating the Hessian using a scaled identity matrix. Based on the classic augmented Lagrangian function and alternating minimization approach, Yang and Zhang proposed YALL1 (Your ALgorithm for L1) to solve the ℓ_1-norm regularized problem [139]. Non-convex regularizers to bridge the sparsity promoting ℓ_1-norm and the ℓ_0 counting semi-norm have been previously investigated in [41, 40, 42, 43, 148]

Our proposed approaches in Sections 4.2 and 4.3 are based on quasi-Newton methods, which have been previously shown to be effective for sparsity recovery problems (see e.g., [141, 85, 145]). (For example, Becker and Fadili use a zero-memory rank-one quasi-Newton approach for proximal splitting [29].) Trust-region methods have also been implemented for sparse reconstruction (see e.g., [132, 72]). Our approach is novel in the transformation of the sparse recovery problem to a differentiable unconstrained minimization problem and in the use of eigenvalues for efficiently solving the trust-region subproblem.

4.2 Trust-Region Methods for Sparse Relaxation

This section concerns solving the sparse recovery problem of the form

$$\underset{\mathbf{f} \in \mathbb{R}^n}{\text{minimize}} \ \frac{1}{2}\|\mathbf{A}\mathbf{f} - \mathbf{b}\|_2^2 + \tau\|\mathbf{f}\|_1, \tag{4.1}$$

where $\mathbf{A} \in \mathbb{R}^{\tilde{m} \times \tilde{n}}$, $\mathbf{f} \in \mathbb{R}^{\tilde{n}}$, $\mathbf{b} \in \mathbb{R}^{\tilde{m}}$, $\tilde{m} \ll \tilde{n}$, and $\tau > 0$ is a constant regularization parameter (see [125, 37, 48]). The work describes here is based on the paper by Adhikari et al. [1]. By letting

$$\mathbf{f} = \mathbf{u} - \mathbf{v},$$

where $\mathbf{u}, \mathbf{v} \succeq 0$, we write (4.1) as the constrained but differentiable optimization problem

$$\underset{\mathbf{u},\mathbf{v}\in\mathbb{R}^{\tilde{n}}}{\text{minimize}} \quad \frac{1}{2}\|\mathbf{A}(\mathbf{u}-\mathbf{v})-\mathbf{b}\|_2^2 + \tau\mathbf{1}_{\tilde{n}}^T(\mathbf{u}+\mathbf{v}) \quad \text{s.t.} \quad \mathbf{u},\mathbf{v}\succeq 0, \qquad (4.2)$$

where $\mathbf{1}_{\tilde{n}}$ is the $\tilde{n}$-vector of ones (see, e.g., [61]). We transform (4.2) into an unconstrained optimization problem by the change of variables

$$(\mathbf{u})_i = \log(1 + e^{(\tilde{\mathbf{u}})_i}) \quad \text{and}$$
$$(\mathbf{v})_i = \log(1 + e^{(\tilde{\mathbf{v}})_i}),$$

where $(\mathbf{u})_i, (\mathbf{v})_i \in \mathbb{R}$ for $1 \leq i \leq \tilde{n}$ denotes i-th component of the vector $(\cdot)_i$ (see [14, 99]). With these definitions, $\mathbf{u}$ and $\mathbf{v}$ are guaranteed to be non-negative. Thus, (4.2) is equivalent to the following minimization problem:

$$\min_{\tilde{\mathbf{u}},\tilde{\mathbf{v}}\in\mathbb{R}^{\tilde{n}}} \Phi(\tilde{\mathbf{u}},\tilde{\mathbf{v}}) \triangleq \frac{1}{2}\sum_{i=1}^{\tilde{m}}\left[\left\{\sum_{j=1}^{\tilde{n}}(\mathbf{A})_{i,j}\log\left(\frac{1+e^{(\tilde{\mathbf{u}})_j}}{1+e^{(\tilde{\mathbf{v}})_j}}\right)\right\} - (\mathbf{b})_i\right]^2$$
$$+ \tau\sum_{j=1}^{\tilde{n}}\log\left((1+e^{(\tilde{\mathbf{u}})_j})(1+e^{(\tilde{\mathbf{v}})_j})\right). \qquad (4.3)$$

We propose solving (4.3) using a limited-memory quasi-Newton trust-region optimization approach, which we describe in the next section.

4.2.1 Trust-Region Methods

In this section, we outline the use of a trust-region method to solve (4.3). We begin by combining the unknowns $\tilde{\mathbf{u}}$ and $\tilde{\mathbf{v}}$ into one vector of unknowns

$$\mathbf{x} = [\tilde{\mathbf{u}}^T \ \ \tilde{\mathbf{v}}^T]^T \in \mathbb{R}^n,$$

where $n = 2\tilde{n}$. (With this substitution, Φ can be considered as a function of $\mathbf{x}$.) Trust-region methods to minimize $\Phi(\mathbf{x})$ define a sequence of iterates $\{\mathbf{x}_k\}$ that are updated as follows:

$$\mathbf{x}_{k+1} = \mathbf{x}_k + \mathbf{p}_k,$$

where $\mathbf{p}_k$ is defined as the *search direction*. Each iteration, a new search direction $\mathbf{p}_k$ is computed from solving the following quadratic subproblem with a two-norm

constraint:

$$\mathbf{p}_k = \arg\min_{\mathbf{p}\in\mathbb{R}^n} q_k(\mathbf{p}) \triangleq \mathbf{g}_k^T\mathbf{p} + \frac{1}{2}\mathbf{p}^T\mathbf{B}_k\mathbf{p} \ \ \text{s.t.} \ \ \|\mathbf{p}\|_2 \le \delta_k, \tag{4.4}$$

where $\mathbf{g}_k \triangleq \nabla\Phi(\mathbf{x}_k)$, $\mathbf{B}_k$ is an approximation to $\nabla^2\Phi(\mathbf{x}_k)$, and δ_k is a given positive constant. In large-scale optimization, solving (4.4) represents the bulk of the computational effort in trust-region methods.

Methods that solve the trust-region subproblem to high accuracy are often based on the optimality conditions for a global solution to the trust-region subproblem (see, e.g., [64, 93, 45]) given in the following theorem:

Theorem 3. *Let δ be a positive constant. A vector $\mathbf{p}^*$ is a global solution of the trust-region subproblem (4.4) if and only if $\|\mathbf{p}^*\|_2 \le \delta$ and there exists a unique $\sigma^* \ge 0$ such that $\mathbf{B} + \sigma^*\mathbf{I}$ is positive semidefinite and*

$$(\mathbf{B} + \sigma^*\mathbf{I})\mathbf{p}^* = -\mathbf{g} \quad and \quad \sigma^*(\delta - \|\mathbf{p}^*\|_2) = 0. \tag{4.5}$$

Moreover, if $\mathbf{B} + \sigma^*\mathbf{I}$ is positive definite, then the global minimizer is unique.

4.2.2   Quasi-Newton Matrices

In this section we show how to build an approximation $\mathbf{B}_k$ of $\nabla^2\Phi(\mathbf{x}_k)$ using limited-memory quasi-Newton matrices.

Given the continuously differentiable function Φ and a sequence of iterates $\{\mathbf{x}_k\}$, traditional quasi-Newton matrices are genererated from a sequence of update pairs $\{(\mathbf{s}_k, \mathbf{y}_k)\}$ where

$$\mathbf{s}_k \triangleq \mathbf{x}_{k+1} - \mathbf{x}_k$$

and

$$\mathbf{y}_k \triangleq \nabla\Phi(\mathbf{x}_{k+1}) - \nabla\Phi(\mathbf{x}_k).$$

In particular, given an initial matrix $\mathbf{B}_0$, the Broyden-Fletcher-Goldfarb-Shanno (BFGS) update (see e.g., [88, 95]) generates a sequence of matrices using the following recursion:

$$\mathbf{B}_{k+1} \triangleq \mathbf{B}_k - \frac{1}{\mathbf{s}_k^T\mathbf{B}_k\mathbf{s}_k}\mathbf{B}_k\mathbf{s}_k\mathbf{s}_k^T\mathbf{B}_k + \frac{1}{\mathbf{y}_k^T\mathbf{s}_k}\mathbf{y}_k\mathbf{y}_k^T, \tag{4.6}$$

provided $\mathbf{y}_k^T \mathbf{s}_k \neq 0$. In practice, $\mathbf{B}_0$ is often taken to be a nonzero constant multiple of the identity matrix, i.e., $\mathbf{B}_0 = \gamma \mathbf{I}$, for some $\gamma > 0$. In large -scale optimization, so-called *limited-memory* BFGS (L-BFGS) methods store and use only the m most-recently computed pairs $\{(\mathbf{s}_k, \mathbf{y}_k)\}$, where $m \ll n$. Often m may be very small (for example, Byrd et al. [36] suggest $m \in [3, 7]$). The BFGS update is the most widely-used rank-two update formula that

  (i)   satisfies the *secant condition* $\mathbf{B}_{k+1}\mathbf{s}_k = \mathbf{y}_k$,

  (ii) has hereditary symmetry,

  (iii) provided that $\mathbf{y}_i^T \mathbf{s}_i > 0$ for $i = 0, \ldots k$, then $\{\mathbf{B}_k\}$ exhibits hereditary positive-definiteness.

Often in practice, the condition $\mathbf{y}_k^T \mathbf{s}_k > 0$ can be enforced by either skipping updates when $\mathbf{y}_k^T \mathbf{s}_k \leq 0$ or using a *Wolfe line search* to help generate the sequence $\{\mathbf{x}_k\}$ (for more details, see, e.g., [95]). For the proposed trust-region method, $\nabla^2 \Phi(\mathbf{x})$ is approximated by an L-BFGS matrix.

The L-BFGS matrix $\mathbf{B}_{k+1}$ in (4.6) can be defined recursively as follows:

$$\mathbf{B}_{k+1} = \mathbf{B}_0 + \sum_{i=0}^{k} \left\{ -\frac{1}{\mathbf{s}_i^T \mathbf{B}_i \mathbf{s}_i} \mathbf{B}_i \mathbf{s}_i \mathbf{s}_i^T \mathbf{B}_i + \frac{1}{\mathbf{y}_i^T \mathbf{s}_i} \mathbf{y}_i \mathbf{y}_i^T \right\}.$$

Then $\mathbf{B}_{k+1}$ is at most a rank-$2(k+1)$ perturbation to $\mathbf{B}_0$, and thus, $\mathbf{B}_{k+1}$ can be written as

$$\mathbf{B}_{k+1} = \mathbf{B}_0 + \begin{bmatrix} \boldsymbol{\Psi}_k \end{bmatrix} \begin{bmatrix} \mathbf{M}_k \end{bmatrix} \begin{bmatrix} \boldsymbol{\Psi}_k^T \end{bmatrix}$$

for some $\boldsymbol{\Psi}_k \in \mathbb{R}^{n \times 2(k+1)}$ and $\mathbf{M}_k \in \mathbb{R}^{2(k+1) \times 2(k+1)}$. Byrd et al. [36] showed that $\boldsymbol{\Psi}_k$ and $\mathbf{M}_k$ are given by

$$\boldsymbol{\Psi}_k = \begin{bmatrix} \mathbf{B}_0 \mathbf{S}_k & \mathbf{Y}_k \end{bmatrix} \text{ and } \mathbf{M}_k = -\begin{bmatrix} \mathbf{S}_k^T \mathbf{B}_0 \mathbf{S}_k & \mathbf{L}_k \\ \mathbf{L}_k^T & -\mathbf{D}_k \end{bmatrix}^{-1},$$

where $\mathbf{S}_k \triangleq \begin{bmatrix} \mathbf{s}_0 & \mathbf{s}_1 & \mathbf{s}_2 & \cdots & \mathbf{s}_k \end{bmatrix} \in \mathbb{R}^{n \times (k+1)}$, and $\mathbf{Y}_k \triangleq \begin{bmatrix} \mathbf{y}_0 & \mathbf{y}_1 & \mathbf{y}_2 & \cdots & \mathbf{y}_k \end{bmatrix} \in \mathbb{R}^{n \times (k+1)}$, and $\mathbf{L}_k$ is the strictly lower triangular part and $\mathbf{D}_k$ is the diagonal part of the matrix $\mathbf{S}_k^T \mathbf{Y}_k \in \mathbb{R}^{(k+1) \times (k+1)}$, i.e., $\mathbf{S}_k^T \mathbf{Y}_k = \mathbf{L}_k + \mathbf{D}_k + \mathbf{U}_k$, where $\mathbf{U}_k$ is a strictly upper triangular matrix.

4.2.3   Solving the Trust-Region Subproblem

In this section, we show how to solve (4.4) efficiently. First, we transform (4.4) into an equivalent expression. For simplicity, we drop the subscript k. Let $\mathbf{\Psi} = \mathbf{QR}$ be the "thin" QR factorization of $\mathbf{\Psi}$, where $\mathbf{Q} \in \mathbb{R}^{n \times 2(k+1)}$ has orthonormal columns and $\mathbf{R} \in \mathbb{R}^{2(k+1) \times 2(k+1)}$ is upper triangular. Then

$$\mathbf{B}_{k+1} = \mathbf{B}_0 + \mathbf{\Psi M \Psi}^T = \gamma \mathbf{I} + \mathbf{QRMR}^T \mathbf{Q}^T.$$

Now let $\mathbf{V}\widehat{\mathbf{\Lambda}}\mathbf{V}^T = \mathbf{RMR}^T$ be the eigendecomposition of $\mathbf{RMR}^T \in \mathbb{R}^{2(k+1) \times 2(k+1)}$, where

$$\mathbf{V} \ \in \ \mathbb{R}^{2(k+1) \times 2(k+1)} \text{ is orthogonal,}$$

$$\widehat{\mathbf{\Lambda}} \ \in \ \mathbb{R}^{2(k+1) \times 2(k+1)} \text{ is diagonal,}$$

with $\widehat{\mathbf{\Lambda}} = \text{diag}(\hat{\lambda}_1, \ldots, \hat{\lambda}_{2(k+1)})$. We assume that the eigenvalues $\hat{\lambda}_i$ are ordered in increasing values, i.e., $\hat{\lambda}_1 \leq \hat{\lambda}_2 \leq \cdots \leq \hat{\lambda}_{2(k+1)}$. Since $\mathbf{Q}$ has orthonormal columns and $\mathbf{V}$ is orthogonal, then $\mathbf{P}_\| \triangleq \mathbf{QV} \in \mathbb{R}^{n \times 2(k+1)}$ also has orthonormal columns. Let $\mathbf{P}_\perp$ be a matrix whose columns form an orthonormal basis for the orthogonal complement of the column space of $\mathbf{P}_\|$. Then $\mathbf{P} \triangleq [\ \mathbf{P}_\| \quad \mathbf{P}_\perp] \in \mathbb{R}^{n \times n}$ is such that $\mathbf{P}^T \mathbf{P} = \mathbf{PP}^T = \mathbf{I}$. Thus, the spectral decomposition of $\mathbf{B}$ is given by

$$\mathbf{B} = \mathbf{P \Lambda P}^T, \text{ where } \mathbf{\Lambda} \triangleq \begin{bmatrix} \mathbf{\Lambda}_1 & 0 \\ 0 & \mathbf{\Lambda}_2 \end{bmatrix} = \begin{bmatrix} \hat{\mathbf{\Lambda}} + \gamma \mathbf{I} & 0 \\ 0 & \gamma \mathbf{I} \end{bmatrix}, \qquad (4.7)$$

where $\mathbf{\Lambda} = \text{diag}(\lambda_1, \ldots, \lambda_n)$, $\mathbf{\Lambda}_1 = \text{diag}(\lambda_1, \ldots, \lambda_{2(k+1)}) \in \mathbb{R}^{2(k+1) \times 2(k+1)}$, and $\mathbf{\Lambda}_2 = \gamma \mathbf{I}_{n-2(k+1)}$. Since the $\hat{\lambda}_i$'s are ordered, then the eigenvalues in $\mathbf{\Lambda}$ are also ordered, i.e., $\lambda_1 \leq \lambda_2 \leq \ldots \leq \lambda_{2(k+1)}$. The remaining eigenvalues, found on the diagonal of $\mathbf{\Lambda}_2$, are equal to γ. Finally, since $\mathbf{B}$ is positive definite, then $0 < \lambda_i$ for all i.

Defining $\mathbf{v} = \mathbf{P}^T \mathbf{p}$, the trust-region subproblem (4.4), can be written as

$$\mathbf{v}^* = \arg\min_{\mathbf{v} \in \mathbb{R}^n} q_k(\mathbf{v}) \triangleq \tilde{\mathbf{g}}^T \mathbf{v} + \frac{1}{2}\mathbf{v}^T \mathbf{\Lambda} \mathbf{v} \quad \text{s.t.} \ \ \|\mathbf{v}\|_2 \leq \delta, \qquad (4.8)$$

where $\tilde{\mathbf{g}} = \mathbf{P}^T \mathbf{g}$. From the optimality conditions in Theorem 1, $\mathbf{v}^*$ is a solution to (4.8) if and only if $\|\mathbf{v}^*\|_2 \leq \delta$ and satisfies the following equations:

$$(\mathbf{\Lambda} + \sigma^* \mathbf{I})\mathbf{v}^* = -\tilde{\mathbf{g}} \quad \text{and} \quad \sigma^*(\|\mathbf{v}^*\|_2 - \delta) = 0 \qquad (4.9)$$

for some scalar $\sigma^* \geq 0$. Note that the usual requirement that $\sigma^* + \lambda_i \geq 0$ for all i is not necessary here since $\lambda_i > 0$ for all i (i.e., $\mathbf{B}$ is positive definite). Note further that (4.9) implies that if $\sigma^* > 0$, the solution must lie on the boundary, i.e., $\|\mathbf{v}^*\|_2 = \delta$. In this case, the optimal σ^* can be obtained by finding solving the so-called *secular equation*:

$$\phi(\sigma) = \frac{1}{\|\mathbf{v}(\sigma)\|_2} - \frac{1}{\delta} = 0, \tag{4.10}$$

where $\|\mathbf{v}(\sigma)\|_2 = \| - (\mathbf{\Lambda} + \sigma \mathbf{I})^{-1} \tilde{\mathbf{g}}\|_2$. Since $\lambda_i + \sigma > 0$ for any $\sigma \geq 0$, $\mathbf{v}(\sigma)$ is well-defined. In particular, if we let

$$\tilde{\mathbf{g}} = \begin{bmatrix} \mathbf{P}_\|^T \\ \mathbf{P}_\perp^T \end{bmatrix} \mathbf{g} = \begin{bmatrix} \mathbf{P}_\|^T \mathbf{g} \\ \mathbf{P}_\perp^T \mathbf{g} \end{bmatrix} = \begin{bmatrix} \mathbf{g}_\| \\ \mathbf{g}_\perp \end{bmatrix},$$

then

$$\|\mathbf{v}(\sigma)\|_2^2 = \left\{ \sum_{i=1}^{2(k+1)} \frac{(\mathbf{g}_\|)_i^2}{(\lambda_i - \sigma)^2} \right\} + \frac{\|\mathbf{g}_\perp\|_2^2}{(\gamma - \sigma)^2}. \tag{4.11}$$

We note that $\phi(\sigma) \geq 0$ means $\mathbf{v}(\sigma)$ is feasible, i.e., $\|\mathbf{v}(\sigma)\|_2 \leq \delta$. Specifically, the unconstrained minimizer $\mathbf{v}(0) = -\mathbf{\Lambda}^{-1}\tilde{\mathbf{g}}$ is feasible if and only if $\phi(0) \geq 0$ (see Fig. 4.1(a)). If $\mathbf{v}(0)$ is not feasible, then $\phi(0) < 0$ and there exists $\sigma^* > 0$ such that $\mathbf{v}(\sigma^*) = -(\mathbf{\Lambda} + \sigma^* I)^{-1}\tilde{\mathbf{g}}$ with $\phi(\sigma^*) = 0$ (see Fig. 4.1(b)). Since $\mathbf{B}$ is positive definite, the function $\phi(\sigma)$ is strictly increasing and concave down for $\sigma \geq 0$, making it a good candidate for Newton's method. In fact, it can be shown that Newton's method will converge monontonically and quadratically to σ^* with initial guess $\sigma^{(0)} = 0$ [45].

The method to obtain σ^* is significantly different that the one used in [35] in that we explicitly use the eigendecomposition within Newton's method to compute the optimal σ^*. That is, we differentiate the reciprocal of $\|\mathbf{v}(\sigma)\|$ in (4.11) to compute the derivative of $\phi(\sigma)$ in (4.10), obtaining a Newton update that is expressed only in terms of $\mathbf{g}_\|$, $\mathbf{g}_\perp$, and the eigenvalues of $\mathbf{B}$. In contrast to [35], this approach eliminates the need for matrix solves for each Newton iteration (see Alg. 2 in [35]).

Given σ^* and $\mathbf{v}^*$, the optimal $\mathbf{p}^*$ is obtained as follows. Letting $\tau^* = \gamma + \sigma^*$,
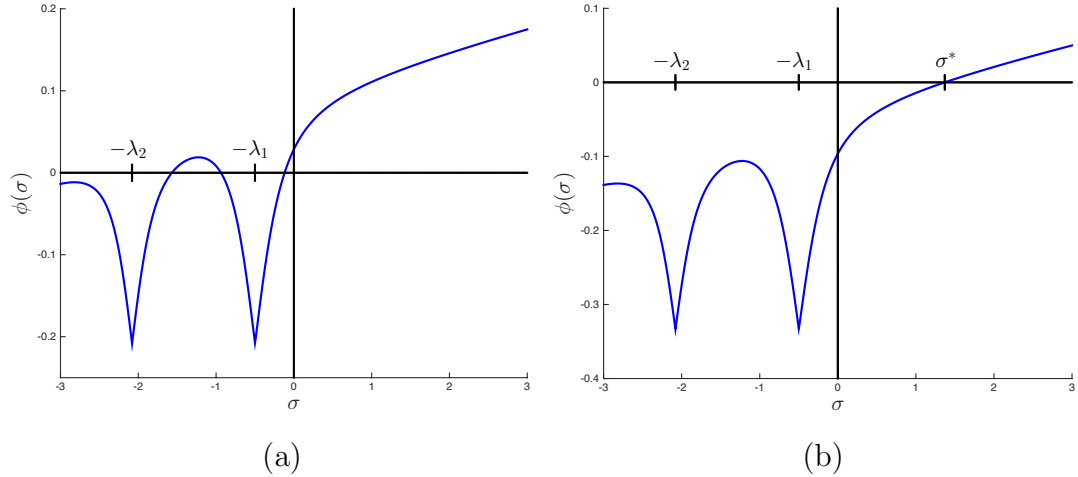
Figure 4.1: Plot of the secular function $\phi(\sigma)$ given in (4.10). (a) The case when $\phi(0) \geq 0$, which implies that the unconstrained minimizer of (4.8) is feasible. (b) When $\phi(0) < 0$, there exists $\sigma^* > 0$ such that $\phi(\sigma^*) = 0$, i.e., $\mathbf{v}^* = -(\mathbf{\Lambda} + \sigma^*\mathbf{I})^{-1}\tilde{\mathbf{g}}$ is well-defined and is feasible.

the solution to the first optimality condition, $(\mathbf{B} + \sigma^*\mathbf{I})\mathbf{p}^* = -\mathbf{g}$, is given by

$$
\begin{aligned}
\mathbf{p}^* &= -(\mathbf{B} + \sigma^*\mathbf{I})\mathbf{g} \\
&= -(\gamma\mathbf{I} + \mathbf{\Psi}\mathbf{M}\mathbf{\Psi}^T + \sigma^*\mathbf{I})^{-1}\mathbf{g} \\
&= -\frac{1}{\tau^*}\left[\mathbf{I} - \mathbf{\Psi}(\tau^*\mathbf{M}^{-1} + \mathbf{\Psi}^T\mathbf{\Psi})^{-1}\mathbf{\Psi}^T\right]\mathbf{g},
\end{aligned} \tag{4.12}
$$

using the Sherman-Morrison-Woodbury formula. Algorithm 1 details the proposed approach for solving the trust-region subproblem. Algorithm 2 outlines our overall limited-memory L-BFGS trust-region approach.

The method described here guarantees that the trust-region subpoblem is solved to high accuracy. Other L-BFGS trust-region methods that solve to high accuracy include [53], which uses a shifted L-BFGS approach, and [34], which uses a "shape-changing" norm in (4.4).

Convergence. Global convergence of Algorithm 2 can be proven by modifying the techniques found in [35, 102] that require that the following assumptions are satisfied: [A.1] There are constants l and u such that $l \leq \|\mathbf{B}_k\| \leq u$ for all k. [A.2] $\nabla\Phi$ is Lipschitz continuous. For Assumption A.1, since $\mathbf{B}_k$ is symmetric and positive definite, $\|\mathbf{B}_k\|_2 = \lambda_{\max}$. Because we are able to explicitly compute the eigenvalues of $\mathbf{B}_k$ in (4.7), we can satisfy Assumption A.1 by accepting an

---

ALGORITHM 1: L-BFGS Trust-Region Subproblem Solver

Compute $\mathbf{R}$ from the "thin" QR factorization of $\mathbf{\Psi}$;

Compute the spectral decomposition

$\quad \mathbf{RMR}^T = \mathbf{V}\hat{\mathbf{\Lambda}}\mathbf{V}^T$ with $\hat{\lambda}_1 \leq \hat{\lambda}_2 \leq \cdots \leq \hat{\lambda}_{2(k+1)}$;

Let $\mathbf{\Lambda}_1 = \hat{\mathbf{\Lambda}} + \gamma\mathbf{I}$;

Define $\mathbf{P}_\parallel = \mathbf{\Psi}\mathbf{R}^{-1}\mathbf{V}$ and $\mathbf{g}_\parallel = \mathbf{P}_\parallel^T\mathbf{g}$;

Compute $\|\mathbf{P}_\perp^T\mathbf{g}\|_2 = \sqrt{\|\mathbf{g}\|_2^2 - \|\mathbf{g}_\parallel\|_2^2}$;

if $\phi(0) \geq 0$ **then**

$\quad \sigma^* = 0$ and compute $\mathbf{p}^*$ from (4.12) with $\tau^* = \gamma$;

else

$\quad$ Use Newton's method to find σ^*;

$\quad$ Compute $\mathbf{p}^*$ from (4.12) with $\tau^* = \gamma + \sigma^*$;

end

---

update pair $(\mathbf{s}_k, \mathbf{y}_k)$ only if $l \leq \lambda_{\max} \leq u$. For Assumption A.2, the gradient of the function $\Phi(\mathbf{x})$ is continuously differentiable, and therefore, $\nabla\Phi$ must be Lipschitz continuous.

With these assumptions satisfied and noting that $\Phi(\mathbf{x}_k) \geq 0$ for all $\mathbf{x}_k$ (since each term in (4.3) is nonnegative), then by [35, Theorem 5.4] the sequence of iterates generated by Algorithm 2 converges to a critical point of Φ.

4.2.4 Numerical Experiments

We call the proposed method, Trust-Region Method for Sparse Relaxation (TrustSpa Relaxation, or simply TrustSpa). We compared the performance of TrustSpa with the Gradient Projection for Sparse Reconstruction (GPSR) method [61] (with the Barzilai and Borwein (BB) approach and without the debiasing option) and YALL1 (Your ALgorithm for L1) method [139]. We note that GPSR is among the most widely used sparse reconstruction methods available and has been cited by 479 IEEE publications alone. In [61], GPSR is shown to outperform the $l1\_ls$ [79] and IST [59] methods. The more recent YALL1 method is also citied more than 693 publications and is shown to outperform SpaRSA [134], FISTA [28],

---

ALGORITHM 2: TrustSpa: Limited-Memory BFGS Trust-Region Method for Sparse Relaxation

---

Define parameters: m, $0 < \tau_1 < 0.5$, $0 < \varepsilon$;

Initialize $\mathbf{x}_0 \in \mathbb{R}^n$ and compute $\mathbf{g}_0 = \nabla\Phi(\mathbf{x}_0)$;

Let $k = 0$;

while not converged

  if $\|\mathbf{g}_k\|_2 \leq \varepsilon$ **then done**

  Use Algorithm 1 to find $\mathbf{p}_k$ that solves (4.4);

  Compute $\rho_k = (\Phi(\mathbf{x}_k + \mathbf{p}_k) - \Phi(\mathbf{x}_k))/q_k(\mathbf{p}_k)$;

  Compute $\mathbf{g}_{k+1}$ and update $\mathbf{B}_{k+1}$;

  if $\rho_k \geq \tau_1$ **then**

    $\mathbf{x}_{k+1} = \mathbf{x}_k + \mathbf{p}_k$;

  else

    $\mathbf{x}_{k+1} = \mathbf{x}_k$;

  end if

  Compute trust-region radius δ_{k+1};

  $k \leftarrow k + 1$;

end while

---

and SPGL1 [128] in [139]. We evaluate the effectiveness of the proposed TrustSpa method by solving 1D and 2D signal reconstruction problems.

We implemented TrustSpa in Matlab R2015a using a MacBook Pro with Intel Core i7 2.8GHz processor with 16GB memory. Both TrustSpa and GPSR-BB methods are initialized at the same starting point, i.e., zero and terminate if the relative objective values do not significantly change, i.e, $|\Phi(\mathbf{x}^{k+1}) - \Phi(\mathbf{x}^k)|/|\Phi(\mathbf{x}^k)| \leq 10^{-8}$. Similarly, YALL1 method is also initialized with zero and is terminated as authors instructed in the YALL1 User's Guide [144] and its Matlab implementation, i.e., $\|\mathbf{x}^{k+1} - \mathbf{x}^k\|_2/\|\mathbf{x}^k\|_2 \leq 10^{-4}$. The regularization parameter τ in (4.1) is optimized independently for each algorithm to minimize the mean-squared error (MSE $= \frac{1}{\tilde{n}}\|\hat{\mathbf{f}} - \mathbf{f}\|_2^2$, where $\hat{\mathbf{f}}$ is an estimate of $\mathbf{f}$).

1D signal recovery

Similar to the experiment found in [61, Sec. IV.A], the true signal **f** is of size 4,096 with 160 randomly assigned nonzeros with amplitude ± 1 (see Fig. 4.2(a)). We obtain compressive measurements **b** of size 1,024 (see Fig. 4.2(b)) by projecting the true signal using a randomly generated system matrix (**A**) from the standard normal distribution with orthonormalized rows. In particular, the measurements are corrupted by 5% of Gaussian noise.

(a) Truth **f** ($\tilde{n} = 4096$, number of nonzeros $= 160$)

(b) Measurements **b** ($\tilde{m} = 1024$, noise level $= 5\%$)
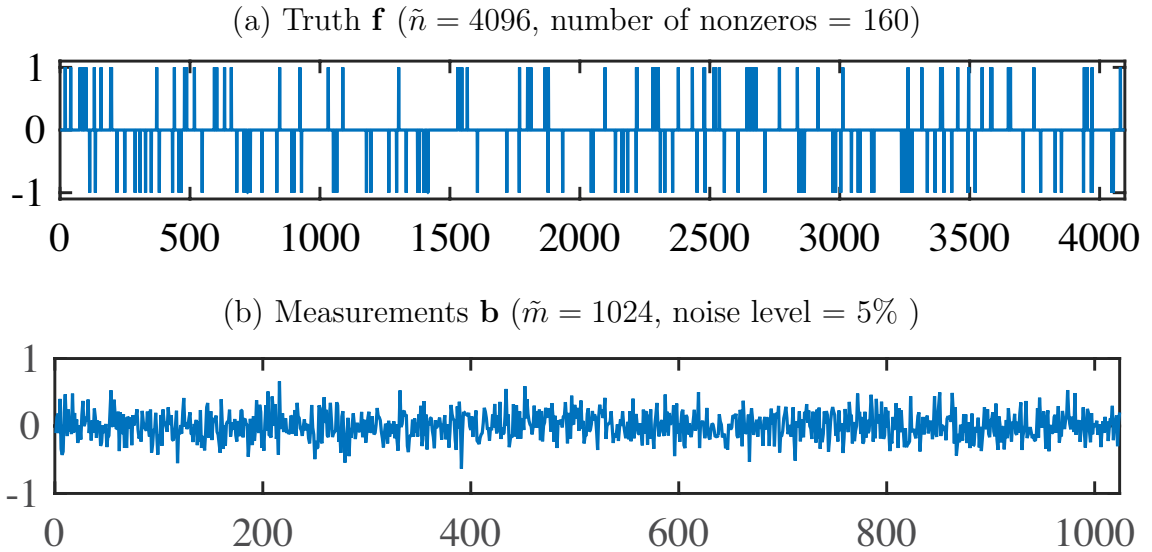
Figure 4.2: Experimental setup: (a) True signal **f** of size 4,096 with 160 $\pm$ spikes, (b) compressive measurements **b** with 5% Gaussian noise.

We ran the experiment 10 times with 10 different Gaussian noise realizations. The average MSE for GPSR-BB for the 10 trials is 1.758×10^{-4} and the average computational time is 4.45 seconds. The average MSE for YALL1 is 1.753×10^{-4} and the average computational time is 0.86 seconds. Note that the YALL1 is terminated with a lower tolerance value, i.e., 10^{-4}. If we use 10^{-8} as the YALL1's stopping tolerance, then we will get same solution with higher computational time. In comparison, the average MSE for TrustSpa is 9.827×10^{-5}, and the average computational time is 3.52 seconds. For one particular trial with 5% noise, the GPSR-BB reconstruction, $\hat{\mathbf{f}}_{\text{GPSR}}$ (see Fig. 4.3(a)), has MSE 1.624×10^{-4} and the
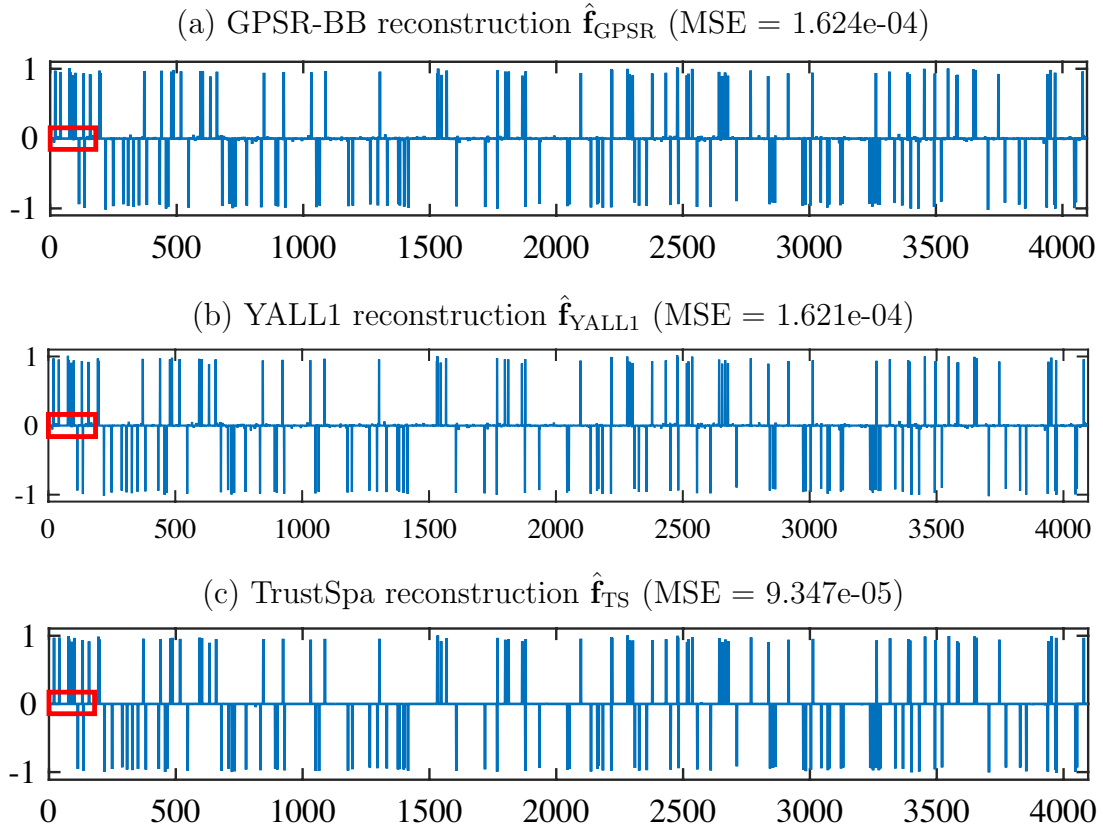
Figure 4.3: (a) GPSR-BB reconstruction, $\hat{\mathbf{f}}_{\text{GPSR}}$, (b) YALL1 reconstruction, $\hat{\mathbf{f}}_{\text{YALL1}}$, (c) TrustSpa reconstruction, $\hat{\mathbf{f}}_{\text{TS}}$. MSE $= (1/\tilde{n})\|\hat{\mathbf{f}} - \mathbf{f}\|_2^2$. Note the lower MSE for the proposed method.

YALL1 reconstruction $\hat{\mathbf{f}}_{\text{YALL1}}$ (see Fig. 4.3(b)), has MSE 1.621×10^{-4} while the TrustSpa reconstruction, $\hat{\mathbf{f}}_{\text{TS}}$ (see Fig. 4.3(c)), has MSE 9.347×10^{-5}. Note that the $\hat{\mathbf{f}}_{\text{TS}}$ has fewer reconstruction artifacts (see Fig. 4.4). Quantitatively, $\hat{\mathbf{f}}_{\text{GPSR}}$ has 786 nonzeros, where the spurious solutions are between the order of 10^{-2} and 10^{-3}. In contrast, because of the variable transformations used by TrustSpa, the algorithm terminates with no zero components in its solution; however, only 579 components are greater than 10^{-6} in absolute value. This has the effect of rendering most spurious solutions less visible.
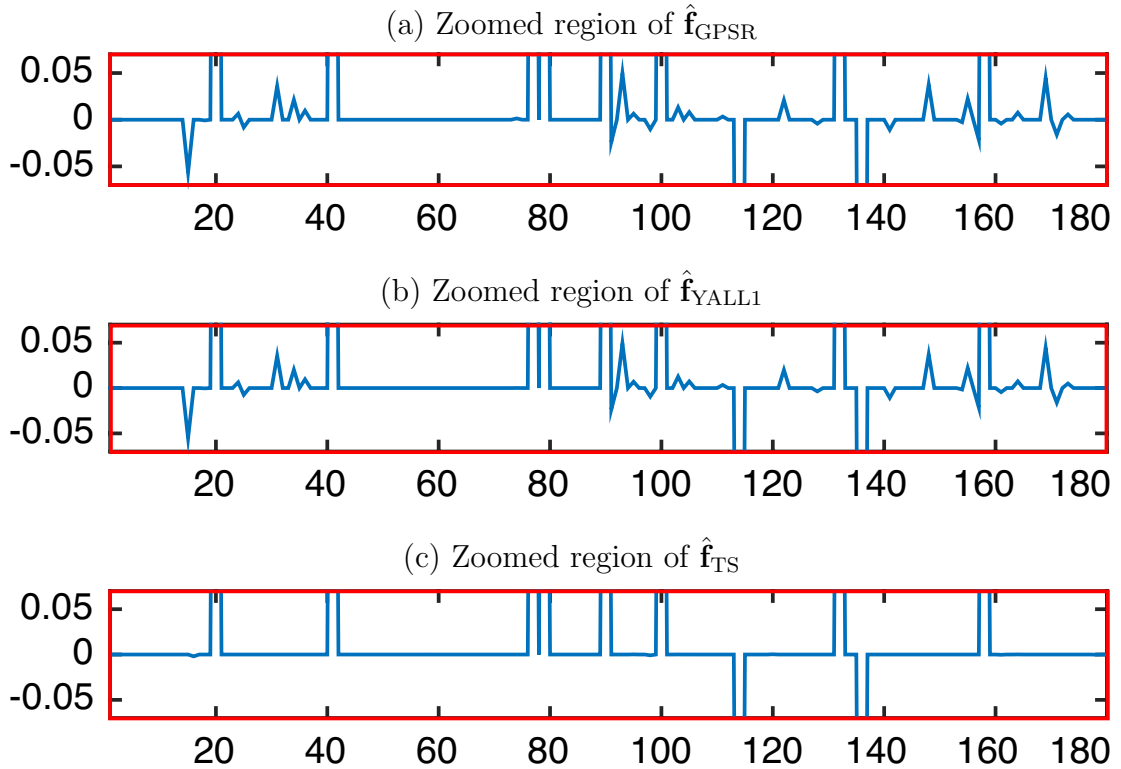
Figure 4.4: Zoomed boxed regions in the reconstructions in Fig. 4.3: (a) A zoomed region of $\hat{\mathbf{f}}_{\text{GPSR}}$, (b) A zoomed region of $\hat{\mathbf{f}}_{\text{YALL1}}$, (c) a zoomed region of $\hat{\mathbf{f}}_{\text{TS}}$. Note the presence of artifacts in GPSR-BB and YALL1 reconstructions that are absent in the proposed method's reconstruction.

2D image deblurring

In this experiment, we wish to recover a Quick Response (QR) code of size 512×512 (see Fig. 4.5(a)) from the 3% zero-mean Gaussian noise corrupted blurry image (see Fig. 4.5(b) and the blue zoomed region in Fig. 4.5(c)). GPSR-BB took 20 seconds (129 iterations) to converge, and its reconstruction $\hat{\mathbf{f}}_{\text{GPSR}}$ has MSE 5.3×10^{-1}. YALL1 took 40 seconds (1450 iterations) to converge to 10^{-4} stopping tolerance, and its reconstruction $\hat{\mathbf{f}}_{\text{YALL1}}$ has MSE 4.03×10^{-1}. In contrast, the proposed TrustSpa took only 16 seconds (42 iterations) to converge (see Fig. 4.6(a)), and its reconstruction $\hat{\mathbf{f}}_{\text{TS}}$ has only MSE 3.9×10^{-1}. Here, $\hat{\mathbf{f}}_{\text{TS}}$ has a lower MSE value due to the low variance of reconstructed amplitudes.

| (a) True image **f** | (b) Observation **b** | (c) Zoomed region |
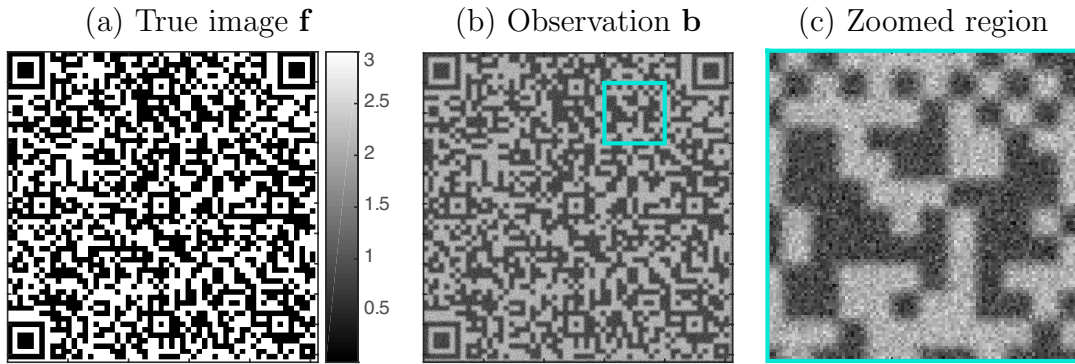
Figure 4.5: Experimental setup: (a) true QR code image **f**, (b) blurry observation **b** with 3% Gaussian noise, (c) a zoomed region of **b**.

| (a) $\hat{\mathbf{f}}_{TS}$ | (b) $\hat{\mathbf{f}}_{TS}$ log-error |
| (c) $\hat{\mathbf{f}}_{GPSR}$ log-error | (d) $\hat{\mathbf{f}}_{YALL1}$ log-error |
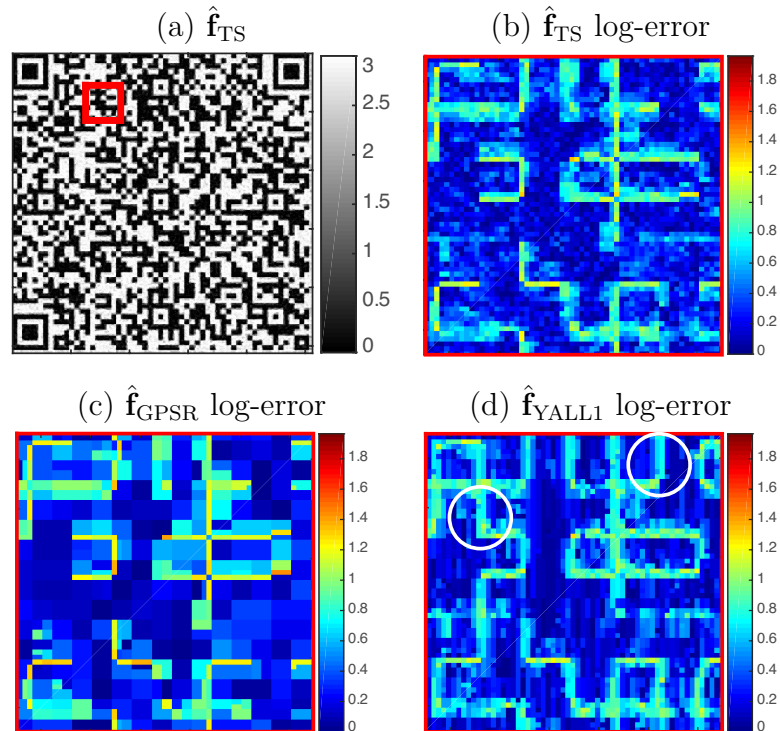
Figure 4.6: (a) TrustSpa reconstruction in true image scale, (b) (c) and (d) a zoomed-in region of the error plots $\log(1 + |\mathbf{f} - \hat{\mathbf{f}}_{TS}|)$, $\log(1 + |\mathbf{f} - \hat{\mathbf{f}}_{YALL1}|)$ and $\log(1 + |\mathbf{f} - \hat{\mathbf{f}}_{GPSR}|)$ respectively. Note the log error of $\hat{\mathbf{f}}_{GPSR}$ has higher amplitude and YALL1 has more artifacts than the TrustSpa.

In particular, $\hat{\mathbf{f}}_{GPSR}$ is in the range [-3, 6.5], $\hat{\mathbf{f}}_{YALL1}$ is in the range [-1.4, 4.4] and

$\hat{\mathbf{f}}_{\text{TS}}$ is in [-1.5, 4.5]. These very high and very low amplitude artifacts in $\hat{\mathbf{f}}_{\text{GPSR}}$ can be mostly found around edges of the black codes (compare zoomed-in log error plots in Fig. 4.6(b) and 4.6(c) for yellow and orange areas). Even though YALL1 gives competitive results in MSE, it does not recover edges of QR image as good as TrustSpa does (compare circled areas in Fig. 4.6(d) with 4.6(b)).

4.2.5 Conclusion

We proposed an approach for solving the ℓ_2-ℓ_1 minimization problem that arises in compressed sensing and sparse recovery problems. Unlike gradient projection-type methods, which uses only the current gradient, our approach uses gradients from previous iterations to obtain a more accurate Hessian approximation. Numerical experiments in 1D and 2D show that our proposed approach mitigates spurious solutions more effectively with a lower average MSE in a smaller amount of time.

4.3 Trust-Region Methods for Nonconvex Sparse Recovery Optimization

In Section 4.2, we proposed limited memory trust-region methods to solve a ℓ_1-norm penalized sparse recovery problem. This section concerns solving ℓ_p-norm $(0 < p < 1)$ regularized sparse recovery problem of the form

$$\underset{\mathbf{f}\in\mathbb{R}^{\tilde{n}}}{\text{minimize}} \ \frac{1}{2}\|\mathbf{A}\mathbf{f} - \mathbf{b}\|_2^2 + \tau\|\mathbf{f}\|_p^p, \tag{4.13}$$

where $\mathbf{A} \in \mathbb{R}^{\tilde{m}\times\tilde{n}}$, $\mathbf{f} \in \mathbb{R}^{\tilde{n}}$, $\mathbf{b} \in \mathbb{R}^{\tilde{m}}$, $\tilde{m} \ll \tilde{n}$, $0 < p < 1$, and $\tau > 0$ is a constant regularization parameter. Non-convex regularizers have been previously investigated in [41, 40, 42, 43, 148] and this work is based on the paper by Adhikari et al. [8]. By letting

$$\mathbf{f} = \mathbf{u} - \mathbf{v},$$

where $\mathbf{u}, \mathbf{v} \succeq 0$, we write (4.13) as a constrained optimization problem

$$\underset{\mathbf{u},\mathbf{v}\in\mathbb{R}^{\tilde{n}}}{\text{minimize}} \qquad \frac{1}{2}\|\mathbf{A}(\mathbf{u}-\mathbf{v})-\mathbf{b}\|_2^2 + \tau\sum_{j=1}^{\tilde{n}}((\mathbf{u})_j + (\mathbf{v})_j)^p$$
$$\text{subject to} \qquad \mathbf{u},\mathbf{v} \succeq 0, \tag{4.14}$$

where $(\cdot)_j$ denotes the jth element of the vector $(\cdot)$. We transform (4.14) into an unconstrained optimization problem by the change of variables

$$(\mathbf{u})_j = \log(1 + e^{(\tilde{\mathbf{u}})_j}) \quad \text{and} \quad (\mathbf{v})_j = \log(1 + e^{(\tilde{\mathbf{v}})_j}),$$

where $(\tilde{\mathbf{u}})_j$, $(\tilde{\mathbf{v}})_j \in \mathbb{R}$ for $1 \le j \le \tilde{n}$ (see [14, 99]). With these definitions, $\mathbf{u}$ and $\mathbf{v}$ are guaranteed to be non-negative. Thus, (4.14) is equivalent to the following minimization problem:

$$\min_{\tilde{\mathbf{u}},\tilde{\mathbf{v}}\in\mathbb{R}^{\tilde{n}}} \Phi(\tilde{\mathbf{u}},\tilde{\mathbf{v}}) \triangleq \frac{1}{2}\sum_{i=1}^{\tilde{m}}\left[\left\{\sum_{j=1}^{\tilde{n}}(\mathbf{A})_{i,j}\log\left(\frac{1+e^{(\tilde{\mathbf{u}})_j}}{1+e^{(\tilde{\mathbf{v}})_j}}\right)\right\} - (\mathbf{b})_i\right]^2$$
$$+ \tau\sum_{j=1}^{\tilde{n}}\left(\log(1+e^{(\tilde{\mathbf{u}})_j}) + \log(1+e^{(\tilde{\mathbf{v}})_j})\right)^p, \tag{4.15}$$

where $(\cdot)_{i,j}$ indicates the (i,j)-th element of the matrix $(\cdot)$. To compute the gradient of $\Phi(\tilde{\mathbf{u}},\tilde{\mathbf{v}})$, we define the following: Let $\tilde{\mathbf{w}}_1, \tilde{\mathbf{w}}_2 \in \mathbb{R}^{\tilde{n}}$ with

$$\begin{aligned}(\tilde{\mathbf{w}}_1)_i &= \log((1+e^{(\tilde{\mathbf{u}})_i})/(1+e^{(\tilde{\mathbf{v}})_i})), \\ (\tilde{\mathbf{w}}_2)_i &= \left(\log(1+e^{(\tilde{\mathbf{u}})_i}) + \log(1+e^{(\tilde{\mathbf{v}})_i})\right)^{p-1},\end{aligned}$$

and let

$$\Phi_1(\tilde{\mathbf{u}},\tilde{\mathbf{v}}) = \mathbf{A}^T\mathbf{A}\tilde{\mathbf{w}}_1 \quad \text{and} \quad \Phi_2(\tilde{\mathbf{u}},\tilde{\mathbf{v}}) = \tau p\,\tilde{\mathbf{w}}_2.$$

Furthermore, let $\mathbf{D}_{\tilde{\mathbf{u}}}, \mathbf{D}_{\tilde{\mathbf{v}}} \in \mathbb{R}^{\tilde{n}\times\tilde{n}}$ be diagonal matrices with

$$(\mathbf{D}_{\tilde{\mathbf{u}}})_{i,i} = \frac{e^{(\tilde{\mathbf{u}})_i}}{1+e^{(\tilde{\mathbf{u}})_i}} \quad \text{and} \quad (\mathbf{D}_{\tilde{\mathbf{v}}})_{i,i} = \frac{e^{(\tilde{\mathbf{v}})_i}}{1+e^{(\tilde{\mathbf{v}})_i}},$$

Then the gradient of the function $\Phi(\tilde{\mathbf{u}},\tilde{\mathbf{v}})$, i.e., $\nabla\Phi = [\nabla_{\tilde{\mathbf{u}}}\Phi; \nabla_{\tilde{\mathbf{v}}}\Phi]$ is given by

$$\begin{aligned}\nabla_{\tilde{\mathbf{u}}}\Phi &= \mathbf{D}_{\tilde{\mathbf{u}}}\left[\ \Phi_1(\tilde{\mathbf{u}},\tilde{\mathbf{v}}) - \mathbf{A}^T\mathbf{b} + \Phi_2(\tilde{\mathbf{u}},\tilde{\mathbf{v}})\right], \\ \nabla_{\tilde{\mathbf{v}}}\Phi &= \mathbf{D}_{\tilde{\mathbf{v}}}\left[-\Phi_1(\tilde{\mathbf{u}},\tilde{\mathbf{v}}) + \mathbf{A}^T\mathbf{b} + \Phi_2(\tilde{\mathbf{u}},\tilde{\mathbf{v}})\right].\end{aligned}$$

We propose solving (4.15) using a limited-memory quasi-Newton trust-region optimization approach (this is similar to Sections 4.2.1, 4.2.2, and 4.2.3), which we describe briefly in next sections. we begin by describing quasi-Newton matrices and then demonstrate their use in a trust-region method to solve (4.15).

4.3.1   Limited-Memory Quasi-Newton Matrices

Given a continuously-differentiable function $\Phi(\mathbf{x})$ as in (4.15), i.e., $\mathbf{x} = [\tilde{\mathbf{u}}, \tilde{\mathbf{v}}]^T \in \mathbb{R}^n$, and a sequence of iterates $\{\mathbf{x}_k\}$, quasi-Newton matrices can be used to approximate $\nabla^2\Phi(\mathbf{x})$. Traditionally, a quasi-Newton matrix is generated by updating an initial matrix $\mathbf{B}_0$ using a sequence of pairs $\{(\mathbf{s}_k, \mathbf{y}_k)\}$, where

$$\mathbf{s}_k \triangleq \mathbf{x}_{k+1} - \mathbf{x}_k \quad \text{and} \quad \mathbf{y}_k \triangleq \nabla\Phi(\mathbf{x}_{k+1}) - \nabla\Phi(\mathbf{x}_k).$$

One of the most widely-used update formulae is the Broyden-Fletcher-Goldfab-Shanno (BFGS) update given by

$$\mathbf{B}_{k+1} \triangleq \mathbf{B}_k - \frac{1}{\mathbf{s}_k^T\mathbf{B}_k\mathbf{s}_k}\mathbf{B}_k\mathbf{s}_k\mathbf{s}_k^T\mathbf{B}_k + \frac{1}{\mathbf{y}_k^T\mathbf{s}_k}\mathbf{y}_k\mathbf{y}_k^T, \tag{4.16}$$

provided $\mathbf{y}_k^T\mathbf{s}_k \neq 0$ and $\mathbf{B}_0$ is a symmetric positive-definite matrix. For simplicity, $\mathbf{B}_0$ is often taken to be a scalar multiple of the identity matrix, i.e., $\mathbf{B}_0 = \gamma\mathbf{I}$ for some $\gamma > 0$. As we discussed in Section 4.2.2, the compact representation for an L-BFGS matrix will be used in the trust-region method for solving (4.15).

4.3.2   Trust-Region Methods

Trust-region methods are one of two important classes of methods for unconstrained optimization (see, e.g., [95, 45]). As we explained in Section 4.2.1, basic trust-region methods generate a sequence of iterates $\{\mathbf{x}_k\}$ by the relation $\mathbf{x}_{k+1} = \mathbf{x}_k + \mathbf{p}_k$, where $\mathbf{p}_k$ is an approximate solution to the *trust-region subproblem* given by

$$\mathbf{p}_k = \underset{\mathbf{p}\in\mathbb{R}^n}{\arg\min} \quad q_k(\mathbf{p}) \triangleq \mathbf{g}_k^T\mathbf{p} + \frac{1}{2}\mathbf{p}^T\mathbf{B}_k\mathbf{p} \tag{4.17}$$
$$\text{subject to} \quad \|\mathbf{p}\|_2 \leq \delta_k,$$

where $\mathbf{g}_k \triangleq \nabla\Phi(\mathbf{x}_k)$, $\mathbf{B}_k$ is an approximation to $\nabla^2\Phi(\mathbf{x}_k)$, and δ_k is a given positive constant. At the end of each trust-region iteration, the *trust-region radius* δ_k is used to update δ_{k+1}; depending on how well the quadratic model predicted actual decreases in the function $\Psi(\mathbf{x})$ from $\mathbf{x}_k$ to $\mathbf{x}_{k+1}$, the trust-region radius is possibly increased or decreased for the next iteration. To solve (4.15), $\mathbf{B}_k$ is taken to be an L-BFGS matrix.

Generally speaking, computing an approximate solution to the trust-region subproblem is the computational bottleneck for most trust-region methods. While trust-region subproblems can be defined using any norm, there is an important advantage in using the Euclidean two-norm: There are well-known optimality conditions for a global solution to (4.17) (see [64, 93]). These optimality conditions allow one to monitor how close iterates for solving the subproblem are to a global solution; they have also inspired algorithms that solve (4.17) by explicitly trying to satisfy the optimality conditions. There are two important advantages in taking $\mathbf{B}_k$ to be an L-BFGS matrix: (i) the trust-region subproblem is convex and (ii) $\mathbf{B}_k$ has structure that can be exploited to solve (4.17) efficiently.

4.3.3 Solving the Trust-Region Subproblem

To solve the trust-region subproblem when $\mathbf{B}_k$ is an L-BFGS matrix, we use the method described in Section 4.2.3. This method solves each trust-region subproblem to high accuracy using the optimality conditions for a global solution to (4.17). Tailored to the case when $\mathbf{B}_k$ is positive definite, the optimality conditions in [64] and [93] are given in Theorem 3 in Section 4.2.3 (see [8] for details).

4.3.4 Numerical Results

(a) Truth $\mathbf{f}^*$ ($\tilde{n} = 4096$, number of nonzeros $= 160$)

(b) Observations $\mathbf{b}$ ($\tilde{m} = 1024$, noise level $\approx 5\%$)
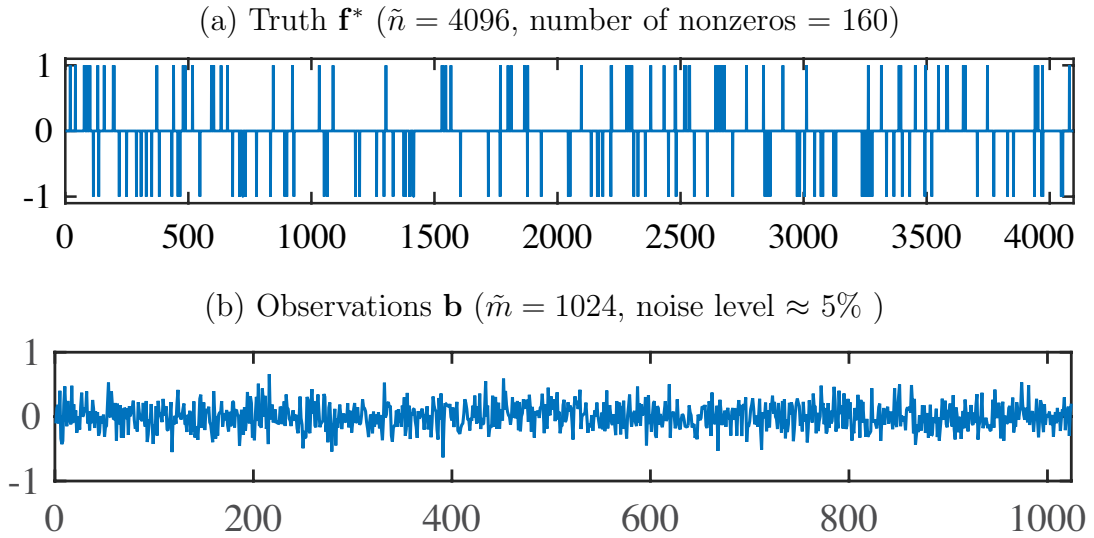
Figure 4.7: Experimental setup: (a) True signal $\mathbf{f}^*$ of size 4,096 with 160 $\pm$ spikes, (b) low-dimensional observations $\mathbf{b}$ with 5% Gaussian noise. Noise level (%) $= 100 \cdot \|\mathbf{A}\mathbf{f}^* - \mathbf{b}\|_2 / \|\mathbf{b}\|_2$.

We demonstrate the effectiveness of the proposed method, called TrustSpa-ℓ_p, by reconstructing a sparse signal (in the canonical basis) of size 4,096 with 160 randomly assigned nonzeros with maximum amplitude ± 1 (see Fig. 4.7(a)). The system matrix ($\mathbf{A}$) is randomly generated with samples from a standard Gaussian distribution, which linearly projects the true signal ($\mathbf{f}^*$) to the low-dimensional observations $\mathbf{b}$ (see Fig. 4.7(b)). These observations are corrupted by 5% of Gaussian noise, where the noise level (%) $= 100 \cdot \|\mathbf{A}\mathbf{f}^* - \mathbf{b}\|_2 / \|\mathbf{b}\|_2$.

(a) TrustSpa-ℓ_p reconstruction $\hat{\mathbf{f}}_{\text{TS-}\ell_p}$ (MSE = 1.403e-05)

(b) Zoomed region of $\hat{\mathbf{f}}_{\text{TS-}\ell_p}$

(c) Zoomed region of TrustSpa-ℓ_1 reconstruction $\hat{\mathbf{f}}_{\text{TS-}\ell_1}$
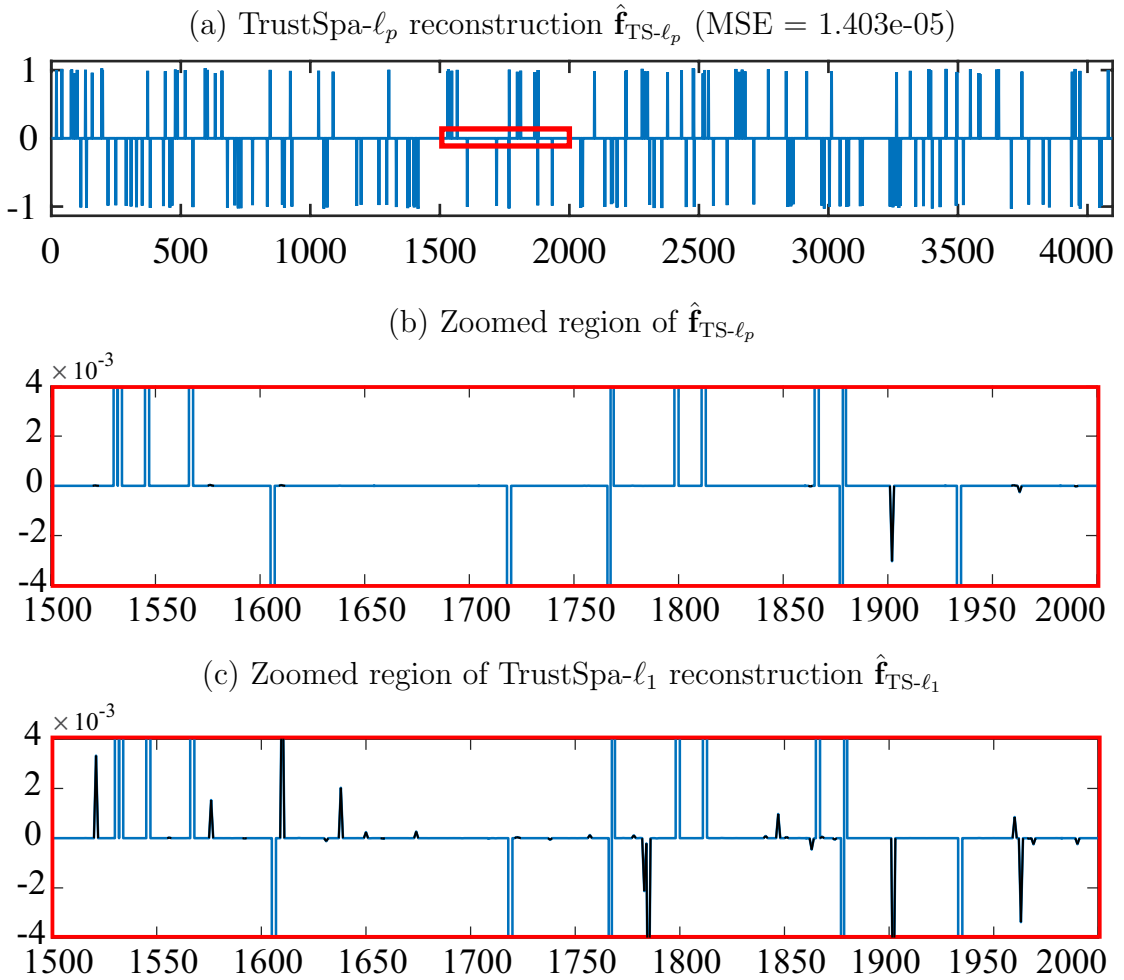
Figure 4.8:   (a) TrustSpa-ℓ_p reconstruction, $\hat{\mathbf{f}}_{\text{TS-}\ell_p}$, with $p = 0.7$, (b) a zoomed region of $\hat{\mathbf{f}}_{\text{TS-}\ell_p}$, (c) the corresponding zoomed region of TrustSpa-ℓ_1 reconstruction, $\hat{\mathbf{f}}_{\text{TS-}\ell_1}$. MSE $= (1/\tilde{n})\|\hat{\mathbf{f}} - \mathbf{f}^*\|_2^2$. Note the presence of artifacts (represented in black spikes) in the TrustSpa-ℓ_1 reconstruction that are rarely present in the TrustSpa-ℓ_p reconstruction.

We implemented the proposed TrustSpa-ℓ_p method in MATLAB R2015a using a MacBook Pro with Intel Core i7 2.8GHz 4-core processor with 16GB memory. The results are compared with the widely-used Gradient Projection for Sparse Reconstruction (GPSR) method [61] without the debiasing option and our TrustSpa-ℓ_1 method (see Section 4.2). In these experiments, all the methods are initialized at the same starting point, i.e., zero and terminate if the relative objective values

do not significantly change, i.e, $|\Phi(\mathbf{x}_{k+1}) - \Phi(\mathbf{x}_k)|/|\Phi(\mathbf{x}_k)| \leq 10^{-8}$. The regularization parameter τ in (4.13) is tuned for the minimum mean-squared error (MSE $= \frac{1}{\tilde{n}}\|\hat{\mathbf{f}} - \mathbf{f}^*\|_2^2$, where $\hat{\mathbf{f}}$ is an estimate of $\mathbf{f}^*$).
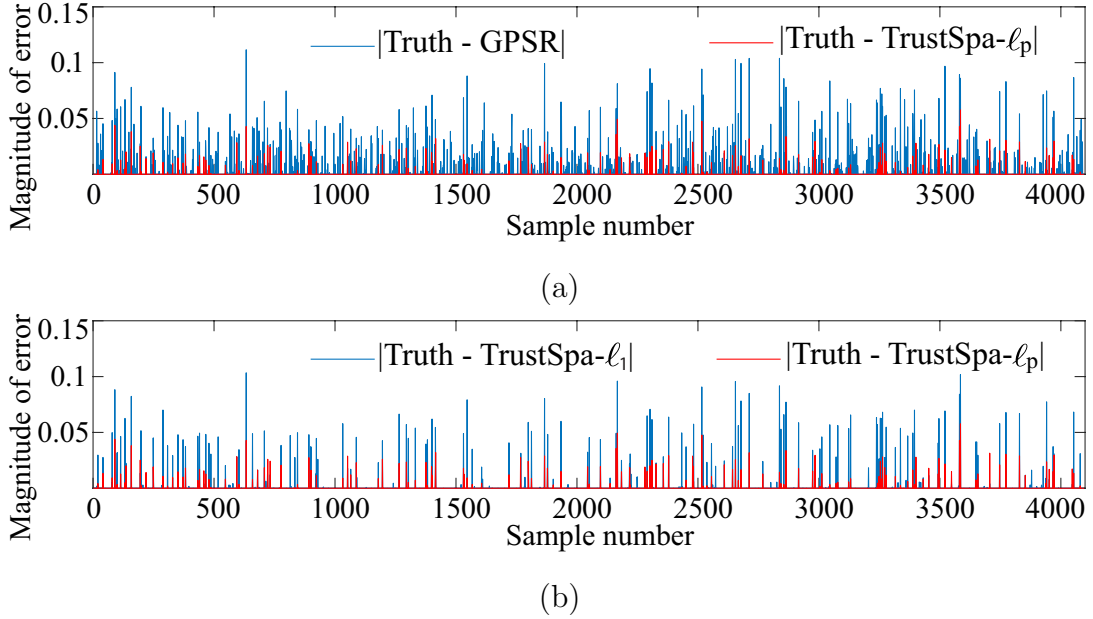
Figure 4.9: Magnitude of error between the true signal $\mathbf{f}^*$ and reconstructions: (a) magnitude of error of the GPSR reconstruction $\hat{\mathbf{f}}_{\mathrm{GPSR}}$ vs. magnitude of error of $\hat{\mathbf{f}}_{\mathrm{TS}-\ell_p}$, (b) magnitude of error of $\hat{\mathbf{f}}_{\mathrm{TS}-\ell_1}$ vs. magnitude of error of $\hat{\mathbf{f}}_{\mathrm{TS}-\ell_p}$. Note the lower error for the proposed TrustSpa-ℓ_p when $p = 0.7$ (represented in red), whose values are more closer to zero.

Using the compressive measurements $\mathbf{b}$ (see Fig. 4.7(b)), a single-trial optimal reconstruction using the proposed TrustSpa-ℓ_p for $p = 0.7$ is given by Fig. 4.8(a). The TrustSpa-ℓ_p reconstruction, $\hat{\mathbf{f}}_{\mathrm{TS}-\ell_p}$, has MSE 1.403×10^{-5}, while the TrustSpa-ℓ_1, $\hat{\mathbf{f}}_{\mathrm{TS}-\ell_1}$ (see Fig. 4.8(c) for a zoomed region of $\hat{\mathbf{f}}_{\mathrm{TS}-\ell_1}$) has MSE 9.347×10^{-5}, and the GPSR reconstruction (see Fig. 4.3(a) for the full reconstruction) has MSE 1.624×10^{-4}. Specifically, notice that the $\hat{\mathbf{f}}_{\mathrm{TS}-\ell_1}$ has more spurious artifacts (shown in black in Fig. 4.8(c)) than the artifacts in $\hat{\mathbf{f}}_{\mathrm{TS}-\ell_p}$ (see black spikes in Fig. 4.8(b)). Quantitatively, $\hat{\mathbf{f}}_{\mathrm{TS}-\ell_p}$ has only 263 nonzero components greater than 10^{-6} in absolute value, while $\hat{\mathbf{f}}_{\mathrm{TS}-\ell_1}$ has 579 nonzeros.

In addition, we analyzed the discrepancy between the true and approximated

amplitudes from each method using magnitude error plots (see Fig. 4.9). In particular, the magnitude of error of the $\hat{\mathbf{f}}_{\text{TS-}\ell_p}$ is much closer to zero (see the red color spikes in Fig. 4.9(a) and (b)) than the magnitude of error of the GPSR reconstruction $\hat{\mathbf{f}}_{\text{GPSR}}$ (see blue spikes in Fig. 4.9(a)) and the $\hat{\mathbf{f}}_{\text{TS-}\ell_1}$ (see blue spikes in Fig. 4.9(b)). These results indicate that the TrustSpa-ℓ_p method better approximates the truth in terms of signal amplitude.

Furthermore, ten-trial average MSE values and average computational times for each method are reported in Table 4.1, showing that the above single trial claims are robust with different Gaussian noise realizations.

Method	Ten-trial average	
	MSE	Time (seconds)
GPSR	1.758×10^{-4}	4.45
TrustSpa-ℓ_1	9.827×10^{-5}	3.52
TrustSpa-$\ell_\mathbf{p}$	$\mathbf{1.791 \times 10^{-5}}$	**1.57**

Table 4.1: Reconstruction MSE and computational time for the results averaged over ten-trials. MSE $= (1/\tilde{n})\|\hat{\mathbf{f}} - \mathbf{f}^*\|_2^2$.

In our experience with this 5% Gaussian noise corrupted dataset, there is no any significant improvement in MSE value for p-values less than 0.7. Therefore, we have used the TrustSpa-ℓ_p reconstruction with $p = 0.7$ as a representative for the TrustSpa-ℓ_p method.

4.3.5 Conclusion

Here, we proposed a quasi-Newton trust-region method for solving a non-convex penalized sparsity recovery problem. We formulate the minimization problem as a smooth unconstrained optimization problem using a change of variables. We bridge the commonly-used convex ℓ_1 norm with the ℓ_0 quasi-norm using a non-convex ℓ_p norm. Numerical results show that the proposed TrustSpa-ℓ_p approach eliminates spurious solutions more effectively than using an ℓ_1-regularization term. Furthermore, the proposed method converges faster over the 10-trial average.

4.4 Recovery and Demixing of Sparse Signals using Nonconvex Regularization

In many real-world applications such as separation of texture in images (this is so-called source separation) [52], image inpainting and super-resolution [90], we have to recover and demix signals. In this collaborative work with Dr. Fei Wen, we address the sparse recovery and demixing problem of signals that are sparse in some known dictionary. In particular, I propose to employ the ℓ_p-norm $(0 \leq p < 1)$ penalty term to enforce the sparsity of the reconstructions. This nonconvex formulation is typically difficult to solve. We propose two first-order algorithms based on block coordinate descent (BCD) and alternative direction method of multipliers (ADMM) to solve this noncovex sparse recovery problem. The new algorithms are convergent in the nonconvex case under some mild conditions and scale well for high-dimensional problems. Various numerical experiments showed that the new algorithms can achieve considerable performance gain over the existing ℓ_1-regularized algorithms. The techinical detilas and experiemntal results in this section are based on our paper [133] with the explicit permission from Dr. Fei Wen.

4.4.1 Introduction

This work concerns of solving the problem of identifying two sparse signals $\mathbf{f}_k \in \mathbb{R}^{n_k}$, $k = 1, 2$, from linear measurements $\mathbf{b} \in \mathbb{R}^m$. Specifically, in the presence of noise, the measurement model can be written as

$$\mathbf{b} = \mathbf{A}_1\mathbf{f}_1 + \mathbf{A}_2\mathbf{f}_2 + \mathbf{n}, \tag{4.18}$$

where $\mathbf{A}_k \in \mathbb{R}^{m \times n_k}$ are known system matrices and $\mathbf{n}$ is the additive Gaussian noise. Here, signals $\mathbf{f_1}$ and $\mathbf{f_2}$ are known to be sparse. For example, in source separation applications [119], $\mathbf{A_1}$ and $\mathbf{A_2}$ are two dictionaries allowing for sparse representation of the two distinct features, and $\mathbf{f_1}$ and $\mathbf{f_2}$ are the corresponding sparse coefficients describing these features. In image inpainting, $\mathbf{A_1}$ be a basis for the image (e.g., inverse discrete cosine transformation) and $\mathbf{f_1}$ holds the cor-

responding sparse coefficients. Since image corruptions such as over-written text and salt-and-pepper noise are sparse in canonical basis, we can select corruptions as $\mathbf{f_2}$ while $\mathbf{A_2} = \mathbf{I}$.

To recover $\mathbf{f_1}$ and $\mathbf{f_2}$ from noise corrupted measurements $\mathbf{b}$, we propose to solve the following ℓ_p-norm regularized constrained minimization problem:

$$(\hat{\mathbf{f}}_1, \hat{\mathbf{f}}_2) = \underset{\mathbf{f_1}, \mathbf{f_2}}{\arg\min} \quad \left\{ \mu \|\mathbf{f_1}\|_{p_1}^{p_1} + \|\mathbf{f_2}\|_{p_2}^{p_2} \right\}$$
$$\text{subject to} \quad \|\mathbf{A_1}\mathbf{f_1} + \mathbf{A_2}\mathbf{f_2} - \mathbf{b}\|_2 \leq \varepsilon, \tag{4.19}$$

where $0 \leq p_1, p_2 < 1$, $\varepsilon > 0$, μ is a positive parameter which takes the statistic difference between the two components into consideration and its optimal value is related with the statistical information of the true signals $\mathbf{f_1}$ and $\mathbf{f_2}$. Further, this constrained optimization problem (4.19) can also be written as an unconstrained optimization problem:

$$\underset{\mathbf{f_1}, \mathbf{f_2}}{\text{minimize}} \quad \Phi(\mathbf{f_1}, \mathbf{f_2}) = \left\{ \frac{1}{\beta} \|\mathbf{A_1}\mathbf{f_1} + \mathbf{A_2}\mathbf{f_2} - \mathbf{b}\|_2^2 + \mu \|\mathbf{f_1}\|_{\mathbf{p_1}}^{\mathbf{p_1}} + \|\mathbf{f_2}\|_{\mathbf{p_2}}^{\mathbf{p_2}} \right\} \tag{4.20}$$

where $\beta > 0$ is a penalty parameter. When $p_1 = p_2 = 1$, the problem (4.20) reduces down to an ℓ_1-norm regularization problem which is widely used as a sparse promoting method. Since the problem is convex under the ℓ_1-norm, it is easy to trace the global minimum. However, with the ℓ_1-norm regularization we can not expect to recover a much sparser signal, which always has small artifacts [121]. Moreover, minimum number of measurements required for a perfect recontruction can also be reduced as the p-value reduces below 1 [42]. Therefore, according to the literature, the ℓ_p-norm regularization has shown significantly better recovery performance in many applications (see eg., [101, 81]).

4.4.2 Methodology

In the following, I briefly explain two algorithms that we developed to solve the problem (4.20) based on the BCD and ADMM, which are two popular first-order frameworks for solving nonsmooth problems.

Proximal BCD Algorithm

The block coordinate descent (BCD) method minimizes Φ cyclically over each variable $\mathbf{f_1}$ and $\mathbf{f_2}$, while fixing one variable at their last updated value. Specifically, for the problem (4.20), at the $k+1$-th iteration, $\mathbf{f_1}$ and $\mathbf{f_2}$ are alternatingly updated by minimizing the objective as

$$\mathbf{f}_1^{k+1} = \arg\min_{\mathbf{f}_1} \left\{ \frac{1}{\beta} \left\| \mathbf{A}_1\mathbf{f}_1 + \mathbf{A}_2\mathbf{f}_2^k - \mathbf{b} \right\|_2^2 + \mu \left\| \mathbf{f}_1 \right\|_{p_1}^{p_1} \right\}, \tag{4.21}$$

$$\mathbf{f}_2^{k+1} = \arg\min_{\mathbf{f}_2} \left\{ \frac{1}{\beta} \left\| \mathbf{A}_1\mathbf{f}_1^{k+1} + \mathbf{A}_2\mathbf{f}_2 - \mathbf{b} \right\|_2^2 + \left\| \mathbf{f}_2 \right\|_{p_2}^{p_2} \right\}. \tag{4.22}$$

The resulting subproblems (4.21) and (4.22) are difficult to solve analytically due to the nonsmoothnesses and nonconvexity of the ℓ_p-norm terms. Therefore, we propose to adopt an linearizion to the ℓ_2-norm terms in (4.21) and (4.22) and use proximity operator to solve for $k+1$-th iterate (see Section III-A in [133]).

ADMM Algorithm

The alternative direction method of multipliers (ADMM) is a powerful framework which is well suited to solve high-dimensional optimization problems arising in image processing applications. Here, we use two auxiliary variables $\mathbf{z}_1 = \mathbf{f}_1$ and $\mathbf{z}_2 = \mathbf{f}_2$ to reformulate the problem (4.20) as

$$\minimize_{\mathbf{f}_1, \mathbf{f}_2, \mathbf{z}_1, \mathbf{z}_2} \left\{ \left\| \mathbf{A}_1\mathbf{f}_1 + \mathbf{A}_2\mathbf{f}_2 - \mathbf{b} \right\|_2^2 + \beta\mu \left\| \mathbf{z}_1 \right\|_{p_1}^{p_1} + \beta \left\| \mathbf{z}_2 \right\|_{p_2}^{p_2} \right\}$$

$$\text{subject to} \quad \mathbf{f}_1 = \mathbf{z}_1, \ \mathbf{f}_2 = \mathbf{z}_2. \tag{4.23}$$

Even though the reformulation (4.23) seems trivial, the resulting problem now be solved using methods of constrained optimization – the augmented Lagrangian method (see Section III-B in [133]).

Moreover, the above proposed BCD and ADMM methods can be extended to recover 3 channel RGB color images where each channel is assumed to have a similar sparsity pattern.

(a) True image ($\mathbf{f}^*$)

(b) Salt-and-pepper noise corrupted image

(c) JP (PSNR = 21.48 dB)

(d) YALL1 (PSNR = 25.80 dB)

(e) BCD (PSNR = 34.62 dB)

(f) ADMM (PSNR = 34.44 dB)
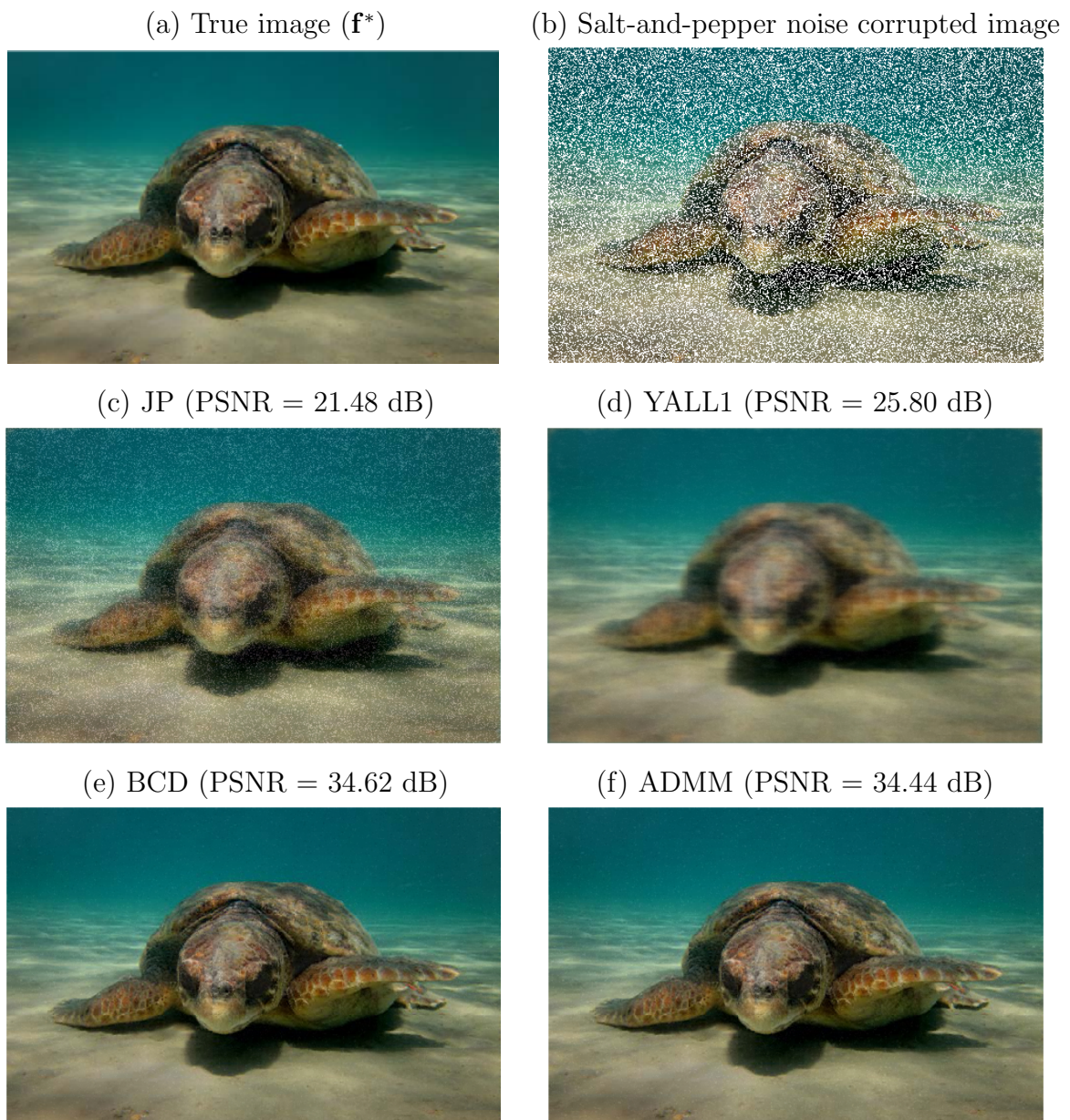
Figure 4.10: Restoration of a 318×500 image corrupted by salt-and-pepper noise (sparsely occurring black and white pixels). (a) True image of interest. (b) Image corrupted by 30% salt-and-pepper noise. (c) Recovered image using JP method. (d) Recovered image using YALL1 method. (e) Proposed BCD reconstruction with $p_1 = 0.9$ and $p_1 = 0.3$. (f) Proposed ADMM reconstruction with $p_1 = 0.8$ and $p_1 = 0.4$. Note the proposed methods (e) and (f) outperform JP and YALL1 in PSNR (dB) $= 10 \log_{10}(\max(\mathbf{f}^*)^2/\mathrm{MSE})$.

4.4.3 Numerical Experiments

We investigate the performance of the two proposed methods using image in-painting experiments, in comparison with two existing ℓ_1-norm solvers: JP [120] and YALL1 [139] solvers. The both proposed BCD and ADMM algorithms are initialized by standard ADMM with $p_1 = p_2 = 1, \mu = 1$ and set $\beta = 10^{-6}$. With properly tuned p_1 and p_2, both the new methods achieve surprisingly better recovery performance compared with the JP and YALL1 methods (see 4.10). The best performance of BCD method (PSNR = 34.62 dB) is given by $p_1 = 0.9$ and $p_2 = 0.3$, which yields a 8.8 dB recovery PSNR improvement than the YALL1. The proposed ADMM (PSNR = 34.44 dB) also gives comparable results to the BCD with 8.6 dB recovery PSNR improvement than the YALL1 reconstruction.

4.4.4 Conclusion

In this method, we proposed a novel formulation for sparse signal recovery and demixing using the ℓ_p-norm ($0 \leq p < 1$) for sparsity inducing. Two first-order algorithms have been developed based on the BCD and ADMM frameworks, which are convergent under some mild conditions and scale well for high-dimensional problems. Furthermore, the new algorithms have been extended for the multitask case. Experiments demonstrated that the new algorithms can achieve considerable performance gain over the ℓ_1-minimization algorithms.

4.5 Summary of Contribution

To solve the ℓ_2-ℓ_1 problem, we proposed a limited-memory trust-region method. Here, we formulated the objective function as a smooth unconstrained optimization problem and use eigenvalues for efficiently solving the trust-region subproblems. We extended this approach to ℓ_p-norm relaxation for better sparse recovery by bridging the gap between the ℓ_1-norm and the ℓ_0 quasi-norm. In addition, we proposed a novel formulation for sparse signal recovery and demixing using the ℓ_p-norm penalization.

Chapter 5

Conclusion

5.1 Summary

Acquisition of a sparse signal from an undersampled set of linear measurements is the main problem of compressed sensing (CS). Within the CS community, minimizing the ℓ_1-penalized least-squares problem is the most popular approach for sparse signal recovery. The least-squares data-fidelity term assumes a Gaussian noise model. However, there are many real-world applications that do not follow Gaussian noise statistics. For example, a low number of photons hitting a detector can not be effectively modeled using a Gaussian noise model, rather require a Poisson noise model. Therefore, under the Poisson noise model, the signal of interest has been usually recovered by exploiting signal sparsity through convex regularizers such as ℓ_1-norm or TV_1 seminorm [70]. But these convex regularizers are merely two representative measures of sparsity. Therefore, in our research, we have investigated relaxations of the regularizers in the Poisson inverse problem to nonconvex regularizers that prompt sparsity even better.

The following summarizes my contributions of the dissertation towards sparse Poisson intensity reconstruction algorithms:

- We proposed SPIRAL-ℓ_p [5], a nonconvex method for further enforce sparsity and structure in the solution using the ℓ_p-norm ($0 \leq p < 1$). We showed that this approach can be uncoupled into the separable ℓ_p-minimization prob-

lems, with each scalar minimization problem is solved using generalized soft-thresholding function [100]. We demonstrated that the proposed method for $p < 1$ eliminates the spurious artifacts found in the SPIRAL-ℓ_1 [70] reconstruction for simulated data. Moreover, we discussed the convergence of the proposed nonconvex algorithm to a critical point.

- If the image of interest is not sparse, we proposed a p-th power ($0 \leq p < 1$) total variation regularized optimization approach (SPIRAL-TV$_p$ [4]) using iterative reweighting. The proposed method iteratively convexifies a sequence of nonconvex subproblems using a weighted TV approach and is solved using a modification to the FISTA method for TV-based denoising. We explored the effectiveness of the proposed method through numerical experiments in image deblurring.

- Recently, we proposed a novel nonconvex Poisson intensity reconstruction method by introducing sparsity promoting Shannon entropy to the SPIRAL framework (SPIRAL-Shannon). In particular, the non-separable Shannon regularization function is approximated using its first-order Taylor series. We showed that this method achieved comparable results to the SPIRAL-ℓ_p with less computational effort.

- In many photon-limited applications including medical imaging, additional information on the signal of interest is often available. Specifically, its maximum and minimum amplitudes at specific regions might be known *a priori*. To fill this gap in SPIRAL framework, we proposed an approach that incorporates this information by the inclusion of upper and lower bound constraints (B-SPIRAL-ℓ_1 [6]).

The following summarizes my contributions of the dissertation towards applications to the proposed nonconvex sparse Poisson intensity reconstruction methods:

- We demonstrated that the SPIRAL-ℓ_p method is effective in solving the fluorescence molecular tomography (FMT) inverse problem when the observations are low-dimensional and are corrupted by high Poisson noise levels [9].

- We proposed following novel stage-based methods to solve time-dependent tomography problems under the Poisson point process:

    - A two-stage method to recover support and the decay rate of time-dependent bioluminescent sources [2].

    - A three-stage method to recover support, fluorescence lifetime, and fluorophore concentration [3].

    There are three main challenges in these two problems: (1) Signals are constrained by partial differential equations. (2) Low photon counts at the boundary are corrupted by Poisson noise. (3) Discretized problem becomes large-scale in space and time.

- We proposed sparse recovery methods for structural variant detection in collaboration with the Sindi Lab at UC Merced [18, 19, 17, 15, 16].

In the context of Gaussian noise, there are various methods for solving the least-squares problem using convex and nonconvex regularization techniques. The following summarizes my contributions of the dissertation towards solving sparsity promoting least-squares optimization problem:

- We proposed to solve the $\ell_2 - \ell_1$ sparse recovery problem using a limited memory trust-region approach [1]. Unlike gradient projection-type methods, which uses only the current gradient, our approach uses gradients from previous iterations to obtain a more accurate Hessian approximation. We demonstrated that the proposed nonconvex method eliminates spurious solutions more effectively and efficiently in numerical experiments in 1D and 2D settings.

- To promote sparsity and the structure of the solution, we proposed to extend the above trust-region approach to solve the $\ell_2 - \ell_p$ $(0 \leq p < 1)$ sparse recovery problem [8].

- Recentely, we proposed methods for recovery and demixing of sparse signals using nonconvex regularization in collaboration with Dr. Fei Wen [133].

5.2 Future Work

We believe that this is the beginning of nonconvex techniques in photon-limited imaging. Therefore, to fill up some remaining gaps in Poisson noise context, we would like to propose following future work:

- Poisson regression model assumes that the mean and the variance of the observed counts are the same, i.e., $\mathrm{Var}(\mathbf{y}_i) = \mathrm{E}(\mathbf{y}_i)$. However, in practice, photon count data often demonstrate over- or under-dispersion compared to the Poisson model [106]. Therefore, it might be effective to model the measurements using Conway-Maxwell-Poisson distribution [78] and regularized using sparsity promoting nonconvex regularizers such as ℓ_p-norm to recover a sparse solution.

- Following a similar approach as in [133], one can research to develop an algorithm that operates on Poisson noise context to recover and demix two sparse signals by exploiting their sparsity structure.

- Develop an algorithm for solving potentially nonlinear photon-limited inverse problems.

Under the Gaussian noise context, we would like to propose trust-region SR1 methods to solve the $\ell_2 - \ell_p$ nonconvex sparsity recovery optimization. In our recent work, the Hessian of the quadratic subproblem is efficiently approximated by the limited-memory BFGS method, which preserves the hereditary positive-definiteness. Since the sparse recovery problem is nonconvex, here we propose to use the limited-memory SR1 (Symmetric Rank 1) trust-region optimization approach, where the Hessian approximation is not necessarily positive definite.

Appendix A

A.1 The Negative Poisson Log-Likelihood Function Formulation

Under the Poisson process model (1.7), the unknown $\mathbf{f}^*$ can be recovered by maximizing the probability of observing measurements $\mathbf{y}$. By assuming each y_i is mutually independent, the *likelihood function* can be written as

$$
\begin{aligned}
L(\mathbf{A}\mathbf{f}^*) &= \prod_{i=1}^{m} p(y_i | (\mathbf{A}\,\mathbf{f}^*)_i), \\
&= \prod_{i=1}^{m} \frac{(\mathbf{e_i}^T \mathbf{A}\mathbf{f}^*)^{y_i} e^{-(\mathbf{e_i}^T \mathbf{A}\mathbf{f}^*)}}{y_i!},
\end{aligned}
$$

where $\mathbf{e_i}$ is the ith canonical basis unit vector. Let $\lambda_i = \mathbf{e_i}^T \mathbf{A}\mathbf{f}^*$,

$$
\begin{aligned}
&= \prod_{i=1}^{m} \frac{(\lambda_i)^{y_i} e^{-\lambda_i}}{y_i!}, \\
&= \frac{\lambda_1^{y_1} \lambda_2^{y_2} \ldots \lambda_m^{y_m} e^{-(\sum_{i=1}^{m} \lambda_i)}}{\prod_{i=1}^{m} y_i!}.
\end{aligned}
$$

Then the log-likelihood function is defined as,

$$
\begin{aligned}
l(\mathbf{Af}^*) &= \log L(\mathbf{Af}^*), \\
&= y_1 \log(\lambda_1) + \ldots + y_m \log(\lambda_m) - \sum_{i=1}^{m} \lambda_i \, \log(e) - \underbrace{\log \prod_{i=1}^{m} y_i!}_{\text{Independent of } f^*}, \\
&= \sum_{i=1}^{m} y_i \, \log(\lambda_i) - \sum_{i=1}^{m} \lambda_i, \\
&= \sum_{i=1}^{m} y_i \log(\mathbf{e_i}^T \mathbf{Af}^*) - \mathbf{1}^T \mathbf{Af}^*,
\end{aligned}
$$

where $\mathbf{1}$ is an m-vector of ones and we neglected $\log(y_i!)$ terms since they are constant with respect to $\mathbf{f}^*$. Thus, the negative Poisson log-likelihood function is given by

$$
F(\mathbf{f}) = -l(\mathbf{Af}) = \mathbf{1}^T \mathbf{Af} - \sum_{i=1}^{m} y_i \log(\mathbf{e}_i^T \mathbf{Af}).
$$

A.2   Subproblem Formulation in SPIRAL

The Poisson intensity reconstruction subproblems take the following constrained minimization form:

$$
\begin{aligned}
\mathbf{f}^{k+1} &= \underset{\mathbf{f} \in \mathbb{R}^n}{\arg\min} \quad F^k(\mathbf{f}) + \tau \, \text{pen}(\mathbf{f}), \\
&\quad \text{subject to } \mathbf{f} \succeq 0,
\end{aligned}
$$

where $F^k(\mathbf{f})$ denotes the second order Taylor series approximation to the $F(\mathbf{f})$ at $\mathbf{f}^k$:

$$
\begin{aligned}
F^k(\mathbf{f}) &\approx F(\mathbf{f}^k) + (\mathbf{f} - \mathbf{f}^k)^T \nabla F(\mathbf{f}^k) + \frac{1}{2}(\mathbf{f} - \mathbf{f}^k)^T \underbrace{\nabla^2 F(\mathbf{f}^k)}_{\approx \alpha_k \mathbf{I}} (\mathbf{f} - \mathbf{f}^k) \\
&= F(\mathbf{f}^k) + (\mathbf{f} - \mathbf{f}^k)^T \nabla F(\mathbf{f}^k) + \frac{\alpha_k}{2} \| \mathbf{f} - \mathbf{f}^k \|_2^2 .
\end{aligned}
$$

Then

$$
\begin{aligned}
\mathbf{f}^{k+1} &= \underset{f \in \mathbb{R}^n}{\arg\min} \quad \underbrace{F(\mathbf{f}^k)}_{\text{independent of } f} + (\mathbf{f} - \mathbf{f}^k)^T \nabla F(\mathbf{f}^k) + \frac{\alpha_k}{2} \parallel \mathbf{f} - \mathbf{f}^k \parallel_2^2 + \tau \, \text{pen}(\mathbf{f}) \\
&= \underset{f \in \mathbb{R}^n}{\arg\min} \quad (\mathbf{f} - \mathbf{f}^k)^T \nabla F(\mathbf{f}^k) + \frac{\alpha_k}{2} \parallel \mathbf{f} - \mathbf{f}^k \parallel_2^2 + \tau \, \text{pen}(\mathbf{f}) \\
&= \underset{f \in \mathbb{R}^n}{\arg\min} \quad \frac{1}{\alpha_k} \mathbf{f}^T \nabla F(\mathbf{f}^k) - \frac{1}{\alpha_k} \mathbf{f}^{kT} \nabla F(\mathbf{f}^k) \\
&\quad + \frac{1}{2}(\mathbf{f} - \mathbf{f}^k)^T (\mathbf{f} - \mathbf{f}^k) + \frac{\tau}{\alpha_k} \, \text{pen}(\mathbf{f}) \\
&= \underset{f \in \mathbb{R}^n}{\arg\min} \frac{1}{2}(\mathbf{f} - \mathbf{f}^k)^T (\mathbf{f} - \mathbf{f}^k) + \frac{1}{2\alpha_k} \mathbf{f}^T \nabla F(\mathbf{f}^k) - \frac{1}{2\alpha_k} \mathbf{f}^{kT} \nabla F(\mathbf{f}^k) \\
&\quad + \frac{1}{2\alpha_k} \nabla F(\mathbf{f}^k)^T \mathbf{f} - \frac{1}{2\alpha_k} \nabla F(\mathbf{f}^k)^T \mathbf{f}^k + \frac{\tau}{\alpha_k} \, \text{pen}(\mathbf{f}) \\
&= \underset{f \in \mathbb{R}^n}{\arg\min} \quad \frac{1}{2}\{(\mathbf{f} - \mathbf{f}^k)^T (\mathbf{f} - \mathbf{f}^k) + \frac{1}{\alpha_k}(\mathbf{f} - \mathbf{f^k})^T \nabla F(\mathbf{f}^k) \\
&\quad + \frac{1}{\alpha_k} \nabla F(\mathbf{f}^k)^T (\mathbf{f} - \mathbf{f}^k) + \underbrace{\frac{1}{\alpha_k^2} \nabla F(\mathbf{f}^k)^T \nabla F(\mathbf{f}^k)}_{\text{add constant}}\} + \frac{\tau}{\alpha_k} \, \text{pen}(\mathbf{f}) \\
&= \underset{f \in \mathbb{R}^n}{\arg\min} \quad \frac{1}{2}\left\{\left[(\mathbf{f} - \mathbf{f^k})^T + \frac{1}{\alpha_k}\nabla F(\mathbf{f}^k)^T\right]\left[(\mathbf{f} - \mathbf{f^k}) + \frac{1}{\alpha_k}\nabla F(\mathbf{f}^k)\right]\right\} + \frac{\tau}{\alpha_k} \, \text{pen}(\mathbf{f}) \\
&= \underset{f \in \mathbb{R}^n}{\arg\min} \quad \frac{1}{2} \parallel \mathbf{f} - \underbrace{(\mathbf{f}^k + \frac{1}{\alpha_k}\nabla F(\mathbf{f}^k))}_{\mathbf{s}_k} \parallel_2^2 + \frac{\tau}{\alpha_k} \, \text{pen}(\mathbf{f}).
\end{aligned}
$$

A.3   Finding the Thresholding Value $\gamma_p(\lambda)$

Since the solution f^* of (2.14) is nonnegative when $s > 0$, we can write the objective function and its first derivative as

$$
\begin{aligned}
\Omega(f) &= \frac{1}{2}(f - s)^2 + \lambda f^p, \\
\Omega'(f) &= f - s + \lambda p f^{p-1}
\end{aligned}
$$

respectively. When $s = \gamma_p(\lambda)$, there exists f_p^* such that

$$
\begin{aligned}
\Omega(f_p^*) &= \Omega(0) \\
\frac{1}{2}(f_p^* - \gamma_p(\lambda))^2 + \lambda f_p^* &= \frac{1}{2}(\gamma_p(\lambda))^2,
\end{aligned} \tag{A.1}
$$

and

$$\Omega'(f_p^*) = 0$$
$$f_p^* - \gamma_p(\lambda) + \lambda p(f_p^*)^{p-1} = 0$$
$$\gamma_p(\lambda) = f_p^* + \lambda p(f_p^*)^{p-1}. \tag{A.2}$$

Then, we can substitute $\gamma_p(\lambda)$ in Eq. (A.2) to Eq. (A.1), and obtain the following equation

$$(f_p^*)^p(2\lambda(1-p) - (f_p^*)^{2-p}) = 0.$$

Since $f_p^* > 0$, we can obtain f_p^* as

$$f_p^* = (2\lambda(1-p))^{\frac{1}{2-p}}. \tag{A.3}$$

Then the thresholding value $\gamma_p(\lambda)$ is obtained by substituting f_p^* in Eq. (A.3) back into the Eq. (A.2):

$$\gamma_p(\lambda) = (2\lambda(1-p))^{\frac{1}{2-p}} + \lambda p(2\lambda(1-p))^{\frac{p-1}{2-p}}.$$

A.4 Special Cases of GST Function

When $p = 0$, the GST function $T_0(s, \lambda)$ is called the *hard-thresholding function*, and it solves

$$\underset{f}{\text{minimize}} \quad \frac{1}{2}(f - s)^2 + \lambda|f|^0,$$

where

$$|f|^0 = \begin{cases} 0, & \text{if } f = 0 \\ 1, & \text{if } f \neq 0. \end{cases}$$

In this case, the GST function is given by

$$T_0(s, \lambda) = \begin{cases} 0, & \text{if } |s| \leq \gamma_0(\lambda) \\ s, & \text{if } |s| > \gamma_0(\lambda), \end{cases} \tag{A.4}$$

where the thresholding value is obtained by evaluating (2.17) at $p = 0$, i.e., $\gamma_0(\lambda) = (2\lambda)^{1/2}$.

When $p = 1$, the GST function becomes the *soft-thresholding function*, where $\gamma_1(\lambda) = \lambda$, and

$$T_1(s, \lambda) = \begin{cases} 0, & \text{if } |s| \leq \gamma_1(\lambda) \\ \text{sgn}(s)(|s| - \lambda), & \text{if } |s| > \gamma_1(\lambda). \end{cases}$$

A.5 Image Quality Metrics

(1) The Volume Ratio (VR) [124]: The VR measures the ratio between the true and the reconstructed target volumes and is given by

$$\text{VR} = \frac{|\text{rROI}|}{|\text{ROI}|},$$

where ROI is the true region of interest and rROI is the reconstructed region of interest containing the reconstructed signals whose amplitudes are higher than half of the maximum amplitude of the reconstructed signal. Here, $|\cdot|$ denotes the number of elements of the set. Ideally, VR is close to 1.

(2) The dice similarity coefficient (Dice) [46]: Dice measures the location accuracy of the reconstructed target with respect to the true location and is given by

$$\text{Dice} = \frac{2 * |\text{rROI} \cap \text{ROI}|}{|\text{rROI}| + |\text{ROI}|}$$

Here, $|\cdot|$ also denotes the number of elements of the set. Similarly, in the ideal case, Dice is close to 1.

(3) The Contrast-to-Noise Ratio (CNR) [114]: CNR measures how easy it is to see the reconstructed target from the background. CNR is given by

$$\text{CNR} = \frac{\text{Mean}(f_{\text{ROI}}) - \text{Mean}(f_{\text{ROB}})}{\sqrt{\omega_{\text{ROI}}\text{Var}(f_{\text{ROI}}) + (1 - \omega_{\text{ROI}})\text{Var}(f_{\text{ROB}})}},$$

where $\omega_{\text{ROI}} = |\text{ROI}|/(|\text{ROI}| + |\text{ROB}|)$, ROB is the true background region and f denotes the reconstructed signal. A high CNR value means a high contrast between the reconstructed target and the background.

(4) The Mean Square Error (MSE): MSE measures the difference between the approximation and the truth, and it is given by

$$\text{MSE} = \frac{1}{n}\|\mathbf{f} - \mathbf{f}^*\|_2^2,$$

where $\mathbf{f} \in \mathbb{R}^n$ and $\mathbf{f}^* \in \mathbb{R}^n$ are the reconstructed and true signals, respectively. Smaller MSE value is preferred.

A.6 Proof of the Relation

$$\sqrt{\alpha^2 x^2 + \beta^2 y^2} = \max_{p_1, p_2} \{f = \alpha x p_1 + \beta y p_2 : p_1^2 + p_2^2 \leq 1\}.$$
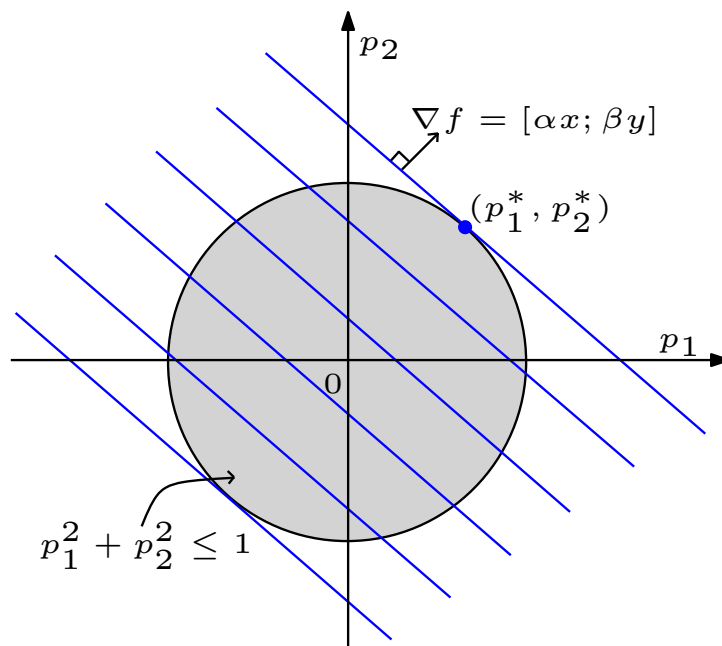
Figure A.1: Function f is maximized at the point (p_1^*, p_2^*).

Proof. As shown in the Fig. A.1, f is maximized at the boundary of the circle. Therefore

$$p_1^2 + p_2^2 = 1 \implies p_1 = \sqrt{1 - p_2^2}.$$

Then the objective function can be written as

$$f = \alpha x p_1 + \beta y p_2 = \alpha x \sqrt{1 - p_2^2} + \beta y \, p_2,$$

and the p_2 value at the maximum point is obtained by setting derivative of f to zero:

$$\frac{df}{dp_2} = 0$$

$$\alpha x \frac{1}{2}(1 - p_2^2)^{-\frac{1}{2}}(-2p_2) + \beta y = 0$$

$$p_2^* = \sqrt{\frac{\beta^2 y^2}{\alpha^2 x^2 + \beta^2 y^2}}.$$

Then p_1^* will be

$$p_1^* = \sqrt{1 - p_2^{*2}} = \sqrt{\frac{\alpha^2 x^2}{\alpha^2 x^2 + \beta^2 y^2}}.$$

Then the maximum function value at the point (p_1^*, p_2^*) is given by

$$\alpha x p_1^* + \beta y p_2^* = \sqrt{\alpha^2 x^2 + \beta^2 y^2}.$$

$\square$

Bibliography

[1] L. Adhikari, J. B. Erway, S. Lockhart, and R. F. Marcia. Limited memory trust-region methods for sparse relaxation. Submitted to *SPIE*, 2017.

[2] L. Adhikari, A. D. Kim, and R. F. Marcia. Nonconvex sparse poisson intensity reconstruction for time-dependent bioluminescence tomography. In *2016 International Symposium on Information Theory and Its Applications (ISITA)*, pages 280–284. IEEE, 2016.

[3] L. Adhikari, A. D. Kim, and R. F. Marcia. Sparse reconstruction for fluorescence lifetime imaging microscopy with poisson noise. In *2016 IEEE Global Conference on Signal and Information Processing (GlobalSIP)*, 2016.

[4] L. Adhikari and R. F. Marcia. p-th power total variation regularization in photon-limited imaging via iterative reweighting. In *2015 European Signal Processing Conference (EUSIPCO)*, pages 1621–1625, 2015.

[5] L. Adhikari and R. F. Marcia. Nonconvex relaxation for poisson intensity reconstruction. In *2015 IEEE International Conference on Acoustics, Speech and Signal Processing (ICASSP)*, pages 1483–1487. IEEE, 2015.

[6] L. Adhikari and R. F. Marcia. Bounded sparse photon-limited image recovery. In *2016 IEEE International Conference on Image Processing (ICIP)*, pages 3508–3512. IEEE, 2016.

[7] L. Adhikari and R. F. Marcia. Non-convex Shannon entropy for photon-limited imaging. Submitted to *SPIE*, 2017.

[8] L. Adhikari, R. F. Marcia, J. B. Erway, and R. J. Plemmons. Trust-region methods for nonconvex sparse recovery optimization. In *2016 International Symposium on Information Theory and Its Applications (ISITA)*, pages 275–279, Oct 2016.

[9] L. Adhikari, D. Zhu, C. Li, and R. F. Marcia. Nonconvex reconstruction for low-dimensional fluorescence molecular tomographic poisson observations. In *2015 IEEE International Conference on Image Processing (ICIP)*, pages 2404–2408. IEEE, 2015.

[10] D. Álvarez, P. Medina, and M. Moscoso. Fluorescence lifetime imaging from time resolved measurements using a shape-based approach. *Opt. Express*, 17(11):8843–8855, May 2009.

[11] A. Antoniadis and J. Bigot. Poisson inverse problems. *The Annals of Statistics*, pages 2132–2158, 2006.

[12] S. R. Arridge. Optical tomography in medical imaging. *Inverse Problems*, 15(2):R41, 1999.

[13] S. R. Arridge and J. C. Schotland. Optical tomography: forward and inverse problems. *Inverse Problems*, 25(12):123010, 2009.

[14] A. Banerjee, S. Merugu, I. S. Dhillon, and J. Ghosh. Clustering with Bregman divergences. *The Journal of Machine Learning Research*, 6:1705–1749, 2005.

[15] M. Banuelos, L. Adhikari, R. Almanza, A. Fujikawa, J. Sahagún, K. Sanderson, M. Spence, S. Sindi, and R. F. Marcia. Non-convex regularization for sparse genomic variant signal detection. Submitted to *2017 IEEE International Symposium on Medical Measurements and Applications*, 2016.

[16] M. Banuelos, L. Adhikari, R. Almanza, A. Fujikawa, J. Sahagún, K. Sanderson, M. Spence, S. Sindi, and R. F. Marcia. Sparse diploid spatial biosignal recovery for genomic variation detection. Submitted to *2017 IEEE International Symposium on Medical Measurements and Applications*, 2016.

[17] M. Banuelos, R. Almanza, L. Adhikari, R. F. Marcia, and S. Sindi. Constrained variant detection with sparc: Sparsity, parental relatedness, and coverage. In *2016 IEEE 38th Annual International Conference of the Engineering in Medicine and Biology Society (EMBC)*, pages 3490–3493. IEEE, 2016.

[18] M. Banuelos, R. Almanza, L. Adhikari, S. Sindi, and R. F. Marcia. Sparse signal recovery methods for variant detection in next-generation sequencing data. In *2016 IEEE International Conference on Acoustics, Speech and Signal Processing (ICASSP)*, pages 864–868. IEEE, 2016.

[19] M. Banuelos, R.i Almanza, L. Adhikari, R. F. Macia, and S. Sindi. Sparse genomic structural variant detection: Exploiting parent-child relatedness for signal recovery. In *2016 IEEE Statistical Signal Processing Workshop (SSP)*, pages 1–5. IEEE, 2016.

[20] J. M. Bardsley and J. Goldes. An iterative method for edge-preserving map estimation when data-noise is Poisson. *SIAM Journal on Scientific Computing*, 32(1):171–185, 2010.

[21] J. C. Baritaux and M. Unser. A primal-dual reconstruction algorithm for fluorescence and bioluminescence tomography. In *2011 IEEE International Symposium on Biomedical Imaging: From Nano to Macro*, pages 960–963, 2011.

[22] A. H. Barnett, J. P. Culver, A. G. Sorensen, A. Dale, and D. A. Boas. Robust inference of baseline optical properties of the human head with three-dimensional segmentation from magnetic resonance imaging. *Appl. Opt.*, 42(16):3095–3108, Jun 2003.

[23] J. Barzilai and J. M. Borwein. Two-point step size gradient methods. *IMA J. Numeri. Anal*, 8(1):141–148, 1988.

[24] H. R. A. Basevi, K. M. Tichauer, F. Leblond, H. Dehghani, J. A. Guggenheim, R. W. Holt, and I. B. Styles. Compressive sensing based reconstruction in bioluminescence tomography improves image resolution and robustness to noise. *Biomedical optics express*, 3(9):2131–2141, 2012.

[25] A. Beck. On the convergence of alternating minimization for convex programming with applications to iteratively reweighted least squares and decomposition schemes. *SIAM Journal on Optimization*, 25(1):185–209, 2015.

[26] A. Beck and M. Teboulle. FISTA method for TV-based denoising problems. `http://iew3.technion.ac.il/~becka/papers/tv_fista.zip`.

[27] A. Beck and M. Teboulle. Fast gradient-based algorithms for constrained total variation image denoising and deblurring problems. *Image Processing, IEEE Transactions on*, 18(11):2419–2434, Nov 2009.

[28] A. Beck and M. Teboulle. A fast iterative shrinkage-thresholding algorithm for linear inverse problems. *SIAM journal on imaging sciences*, 2(1):183–202, 2009.

[29] S. Becker and J. Fadili. A quasi-newton proximal splitting method. In *Advances in Neural Information Processing Systems*, pages 2618–2626, 2012.

[30] M. Bertero, P. Boccacci, G. Desiderà, and G Vicidomini. Image deblurring with poisson data: from cells to galaxies. *Inverse Problems*, 25(12):123006, 2009.

[31] S. Bloch, F. Lesage, L. McIntosh, A. Gandjbakhche, K. Liang, and S. Achilefu. Whole-body fluorescence lifetime imaging of a tumor-targeted near-infrared molecular probe in mice. *Journal of Biomedical Optics*, 10(5):054003–054003–8, 2005.

[32] S. Boyd and L. Vandenberghe. *Convex optimization*. Cambridge University Press, 2004.

[33] B. Brooksby, S. Jiang, H. Dehghani, B. W. Pogue, K. D. Paulsen, J. Weaver, C. Kogel, and S. P. Poplack. Combining near-infrared tomography and magnetic resonance imaging to study in vivo breast tissue: implementation of a laplacian-type regularization to incorporate magnetic resonance structure. *Journal of Biomedical Optics*, 10:051504–051504–10, 2005.

[34] O. Burdakov, L. Gong, Y.-X. Yuan, and S. Zikrin. On efficiently combining limited memory and trust-region techniques. Technical Report 2013:13, Linkping University, Optimization, 2015.

[35] J. V. Burke, A. Wiegmann, and L. Xu. Limited memory BFGS updating in a trust-region framework. Technical report, University of Washington, 1996.

[36] R. H. Byrd, J. Nocedal, and R. B. Schnabel. Representations of quasi-Newton matrices and their use in limited-memory methods. *Math. Program.*, 63:129–156, 1994.

[37] E. J. Candès and T. Tao. Decoding by linear programming. *IEEE Trans. Inform. Theory*, 15(12):4203–4215, 2005.

[38] E.J. Candès, J. Romberg, and T. Tao. Robust uncertainty principles: Exact signal reconstruction from highly incomplete frequency information. *IEEE Transactions on information theory*, 52(2):489, 2006.

[39] A. Chambolle. An algorithm for total variation minimization and applications. *Journal of Mathematical Imaging and Vision*, 20(1-2):89–97, 2004.

[40] R. Chartrand. Exact reconstruction of sparse signals via nonconvex minimization. *Signal Processing Letters, IEEE*, 14(10):707–710, Oct 2007.

[41] R. Chartrand. Nonconvex compressed sensing and error correction. In *Proceedings of 2007 IEEE ICASSP*, Honolulu, Hawaii, April 2007.

[42] R. Chartrand and V. Staneva. Restricted isometry properties and nonconvex compressive sensing. *Inverse Problems*, 24(3):035020, 2008.

[43] R. Chartrand and W. Yin. Iteratively reweighted algorithms for compressive sensing. In *Proc. IEEE International Conference on Acoustics, Speech, and Signal Processing*, pages 3869–3872, 2008.

[44] K. Chen, J. W. Wallis, M. D. McLellan, D. E. Larson, J. M. Kalicki, C. S. Pohl, S. D. McGrath, M. C. Wendl, Q. Zhang, D. P. Locke, et al. Breakdancer: an algorithm for high-resolution mapping of genomic structural variation. *Nature methods*, 6(9):677–681, 2009.

[45] A. R. Conn, N. I. M. Gould, and P. L. Toint. *Trust-Region Methods*. Society for Industrial and Applied Mathematics (SIAM), Philadelphia, PA, 2000.

[46] L. R. Dice. Measures of the amount of ecologic association between species. *Ecology*, 26:297–302, 1945.

[47] D. L. Donoho. De-noising by soft-thresholding. *IEEE Trans. Information Theory*, 41(3):613–627, 1995.

[48] D. L. Donoho. Compressed sensing. *IEEE Trans. Inform. Theory*, 52(4):1289–1306, 2006.

[49] D. L. Donoho and M. Elad. Optimally sparse representation in general (nonorthogonal) dictionaries via ℓ_1 minimization. *Proceedings of the National Academy of Sciences*, 100(5):2197–2202, 2003.

[50] D. L. Donoho, I. M. Johnstone, J. C. Hoch, and A. S. Stern. Maximum entropy and the nearly black object. *Journal of the Royal Statistical Society. Series B (Methodological)*, pages 41–81, 1992.

[51] J. Dutta, S. Ahn, C. Li, S. R Cherry, and R. M. Leahy. Joint ℓ_1 and total variation regularization for fluorescence molecular tomography. *Physics in medicine and biology*, 57(6):1459, 2012.

[52] M. Elad, J. L Starck, P. Querre, and D. L. Donoho. Simultaneous cartoon and texture image inpainting using morphological component analysis (mca). *Applied and Computational Harmonic Analysis*, 19(3):340–358, 2005.

[53] J. B. Erway and R. F. Marcia. Algorithm 943: MSS: MATLAB software for L-BFGS trust-region subproblems for large-scale optimization. *ACM Transactions on Mathematical Software*, 40(4):28:1–28:12, June 2014.

[54] J. Feng, C. Qin, K. Jia, S. Zhu, K. Liu, D. Han, X. Yang, Q. Gao, and J. Tian. Total variation regularization for bioluminescence tomography with the split bregman method. *Applied Optics*, 51(19):4501–4512, 2012.

[55] J. Feng, C. Qin, K. Jia, S. Zhu, X. Yang, and J. Tian. Bioluminescence tomography imaging in vivo: recent advances. *Selected Topics in Quantum Electronics, IEEE Journal of*, 18(4):1394–1402, 2012.

[56] J. A. Fessler and A. O. Hero. Penalized maximum-likelihood image reconstruction using space-alternating generalized EM algorithms. *IEEE Trans. on Image Proc.*, 4(10):1417–1429, Oct 1995.

[57] J.A. Fessler and H. Erdogan. A paraboloidal surrogates algorithm for convergent penalized-likelihood emission image reconstruction. In *Nuclear Science Symposium, 1998. Conference Record. 1998 IEEE*, volume 2, pages 1132–1135 vol.2, 1998.

[58] M. A. T. Figueiredo and J. M. Bioucas-Dias. Restoration of poissonian images using alternating direction optimization. *IEEE Transactions on Image Processing*, 19(12):3133–3145, 2010.

[59] M. A. T. Figueiredo and R. D. Nowak. An EM algorithm for wavelet-based image restoration. *Image Processing, IEEE Transactions on*, 12(8):906–916, 2003.

[60] M.A.T. Figueiredo and J.M. Bioucas-Dias. Deconvolution of poissonian images using variable splitting and augmented lagrangian optimization. In *Statistical Signal Processing, 2009. SSP '09. IEEE/SP 15th Workshop on*, pages 733–736, Aug 2009.

[61] M.A.T. Figueiredo, R.D. Nowak, and S.J. Wright. Gradient projection for sparse reconstruction: Application to compressed sensing and other inverse problems. *IEEE Journal of Selected Topics in Signal Processing*, 1(4):586–597, 2007.

[62] H. Gao and H. Zhao. Multilevel bioluminescence tomography based on radiative transfer equation part 1: l1 regularization. *Optics Express*, 18(3):1854–1871, 2010.

[63] H. Gao and H. Zhao. Multilevel bioluminescence tomography based on radiative transfer equation part 2: total variation and l1 data fidelity. *Optics Express*, 18(3):2894–2912, 2010.

[64] D. M. Gay. Computing optimal locally constrained steps. *SIAM J. Sci. Statist. Comput.*, 2(2):186–197, 1981.

[65] T. Goldstein and S. Osher. The split bregman method for l1-regularized problems. *SIAM Journal on Imaging Sciences*, 2(2):323–343, 2009.

[66] J. W. Goodman and J. F. Belsher. Fundamental limitations in linear invariant restoration of atmospherically degraded images. *Proc. SPIE*, 0075:141–154, 1976.

[67] P. J. Green. Bayesian reconstructions from emission tomography data using a modified em algorithm. *IEEE transactions on medical imaging*, 9(1):84–93, 1990.

[68] D. Han, J. Tian, S. Zhu, J. Feng, C. Qin, B. Zhang, and X. Yang. A fast reconstruction algorithm for fluorescence molecular tomography with sparsity regularization. *Opt. Express*, 18(8):8630–8646, 2010.

[69] Z. T. Harmany, R. F. Marcia, and R. M. Willett. The Sparse Poisson Intensity Reconstruction ALgorithms (SPIRAL) Toolbox. `http://drz.ac/code/spiraltap/`.

[70] Z. T. Harmany, R. F. Marcia, and R. M. Willett. This is SPIRAL-TAP: Sparse Poisson intensity reconstruction algorithms; theory and practice. *Image Processing, IEEE Trans. on*, 21(3):1084–1096, March 2012.

[71] X. He, J. Liang, X. Wang, J. Yu, X. Qu, X. Wang, Y. Hou, D. Chen, F. Liu, and J. Tian. Sparse reconstruction for quantitative bioluminescence tomography based on the incomplete variables truncated conjugate gradient method. *Optics Express*, 18(24):24825–24841, 2010.

[72] M. Hintermüller and T. Wu. Nonconvex TV^q-models in image restoration: Analysis and a trust-region regularization–based superlinearly convergent solver. *SIAM Journal on Imaging Sciences*, 6(3):1385–1415, 2013.

[73] T. Hohage and F. Werner. Inverse problems with poisson data: statistical regularization theory, applications and algorithms. *Inverse Problems*, 32(9):093001, 2016.

[74] F. Hormozdiari, C. Alkan, E. E. Eichler, and S. C. Sahinalp. Combinatorial algorithms for structural variation detection in high-throughput sequenced genomes. *Genome research*, 19(7):1270–1278, 2009.

[75] S. Huang, D. N Tran, and T. D. Tran. Sparse signal recovery based on nonconvex entropy minimization. In *2016 IEEE International Conference on Image Processing (ICIP)*, pages 3867–3871. IEEE, 2016.

[76] H. C. Ishikawa-Ankerhold, R. Ankerhold, and G. P. C. Drummen. Advanced fluorescence microscopy techniques – FRAP, FLIP, FLAP, FRET and FLIM. *Molecules*, 17(4):4047, 2012.

[77] M. Jansen. Multiscale poisson data smoothing. *Journal of the Royal Statistical Society. Series B (Statistical Methodology)*, 68(1):27–48, 2006.

[78] J. B. Kadane, G. Shmueli, T. P. Minka, S. Borle, P. Boatwright, et al. Conjugate analysis of the Conway-Maxwell-Poisson distribution. *Bayesian analysis*, 1(2):363–374, 2006.

[79] S Kim, K. Koh, M. Lustig, S. Boyd, and D. Gorinevsky. A method for large-scale ℓ_1-regularized least squares problems with applications in signal processing and statistics. *IEEE J. Select. Topics Signal Process*, 1(4):606–617, 2007.

[80] D. R. Kincaid and E. W. Cheney. *Numerical Analysis: Mathematics of Scientific Computing.* American Mathematical Society, 3rd edition, 2002.

[81] M. Lai, Y. Xu, and W. Yin. Improved iteratively reweighted least squares for unconstrained smoothed ℓ_q minimization. *SIAM Journal on Numerical Analysis*, 51(2):927–957, 2013.

[82] P. K. Lamm. Variable-smoothing regularization methods for inverse problems. 1999.

[83] E. S. Lander and M. S. Waterman. Genomic mapping by fingerprinting random clones: a mathematical analysis. *Genomics*, 2(3):231–239, 1988.

[84] J. N Laska, M. A. Davenport, and R. G. Baraniuk. Exact signal recovery from sparsely corrupted measurements through the pursuit of justice. In *2009 Conference Record of the Forty-Third Asilomar Conference on Signals Systems and Computers*, pages 1556–1560. IEEE, 2009.

[85] J. Lee, Y. Sun, and M. Saunders. Proximal Newton-type methods for convex optimization. In *Advances in Neural Information Processing Systems*, pages 836–844, 2012.

[86] R. LeVeque. *Finite Difference Methods for Ordinary and Partial Differential Equations: Steady-State and Time-Dependent Problems*. SIAM, Society for Industrial and Applied Mathematics, classics in applied mathematics edition, 7 2007.

[87] C. Li, G. Wang, J. Qi, and S. R. Cherry. Three-dimensional fluorescence optical tomography in small animal imaging using simultaneous positron emission tomography priors. *Optics letters*, 34:2933–2935, 2009.

[88] D. C. Liu and J. Nocedal. On the limited memory BFGS method for large scale optimization. *Math. Program.*, 45:503–528, 1989.

[89] Q. Lyu, Z. Lin, Y. She, and C. Zhang. A comparison of typical ℓ_p minimization algorithms. *Neurocomputing*, 119:413–424, 2013.

[90] S. G. Mallat and G. Yu. Super-resolution with sparse mixing estimators. *IEEE Transactions on Image Processing*, 19(11):2889–2900, 2010.

[91] R. F. Marcia and R. M. Willett. Compressive coded aperture superresolution image reconstruction. In *IEEE International Conference on Acoustics, Speech and Signal Processing*, pages 833–836. IEEE, 2008.

[92] P. Medvedev, M. Stanciu, and M. Brudno. Computational methods for discovering structural variation with next-generation sequencing. *Nature methods*, 6:S13–S20, 2009.

[93] J. J. Moré and D. C. Sorensen. Computing a trust region step. *SIAM J. Sci. and Statist. Comput.*, 4:553–572, 1983.

[94] B. K. Natarajan. Sparse approximate solutions to linear systems. *SIAM journal on computing*, 24(2):227–234, 1995.

[95] J. Nocedal and S. Wright. *Numerical optimization.* Springer Science & Business Media, 2006.

[96] R. Nowak and E.D. Kolaczyk. A multiscale map estimation method for poisson inverse problems. In *Signals, Systems amp; Computers, 1998. Conference Record of the Thirty-Second Asilomar Conference on*, volume 2, pages 1682–1686, Nov 1998.

[97] R. D. Nowak and E. D. Kolaczyk. A statistical multiscale framework for poisson inverse problems. *IEEE Transactions on Information Theory*, 46(5):1811–1825, Aug 2000.

[98] J. Nunez and J. Llacer. A general bayesian image reconstruction algorithm with entropy prior. preliminary application to HST data. *Publications of the Astronomical Society of the Pacific*, 105(692):1192, 1993.

[99] A. Oh and R. Willett. Regularized non-Gaussian image denoising. *ArXiv Preprint 1508.02971*, 2015.

[100] A. Orkusyan, L. Adhikari, J. Valenzuela, and R. F. Marcia. Analysis of p-norm regularized subproblem minimization for sparse photon-limited image recovery. In *2016 IEEE International Conference on Acoustics, Speech and Signal Processing (ICASSP)*, pages 1407–1411. IEEE, 2016.

[101] J. K. Pant, W. Lu, and A. Antoniou. New improved algorithms for compressive sensing based on ℓ_p norm. *IEEE Transactions on Circuits and Systems II: Express Briefs*, 61(3):198–202, 2014.

[102] M. J. D. Powell. Convergence properties of a class of minimization algorithms. *Nonlinear programming*, 2(0):1–27, 1975.

[103] S. Qaisar, R. M. Bilal, W. Iqbal, M. Naureen, and S. Lee. Compressive sensing: From theory to applications, a survey. *Journal of Communications and networks*, 15(5):443–456, 2013.

[104] L. I. Rudin, S. Osher, and E. Fatemi. Nonlinear total variation based noise removal algorithms. *Phys. D*, 60(1-4):259–268, November 1992.

[105] A. Sawatzky, C. Brune, T. Kösters, F. Wübbeling, and M. Burger. EM-TV methods for inverse problems with Poisson noise. In *Level Set and PDE Based Reconstruction Methods in Imaging*, pages 71–142. Springer, 2013.

[106] K. F. Sellers and G. Shmueli. A flexible regression model for count data. 2008.

[107] S. Setzer, G. Steidl, and T. Teuber. Deblurring Poissonian images by split Bregman techniques. *Journal of Visual Communication and Image Representation*, 21:193–199, 2010.

[108] C. E. Shannon. A mathematical theory of communication. *Bell system technical journal*, 27, 1948.

[109] S. Sindi, E. Helman, A. Bashir, and B. J. Raphael. A geometric approach for classification and comparison of structural variants. *Bioinformatics*, 25(12):i222–i230, 2009.

[110] S. Sindi, S. Önal, L. C. Peng, H. Wu, and B. J. Raphael. An integrative probabilistic model for identification of structural variation in sequencing data. *Genome biology*, 13(3):R22, 2012.

[111] S. S. Sindi and B. J. Raphael. Identification of structural variation. *Genome Analysis: Current Procedures and Applications*, page 1, 2014.

[112] J. Skilling and R. K. Bryan. Maximum entropy image reconstruction: general algorithm. *Monthly notices of the royal astronomical society*, 211(1):111–124, 1984.

[113] D. L. Snyder and M. I. Miller. Random point processes in space and time. *Springer-Verlag, New York, NY*, 1991.

[114] X. Song, B. W. Pogue, S. Jiang, M. M. Doyley, H. Dehghani, T. D. Tosteson, and K. D. Paulsen. Automated region detection based on the contrast-to-noise ratio in near-infrared tomography. *Appl. Opt.*, 43:1053–1062, 2004.

[115] J. A. Sorenson and M. E. Phelps. *Physics in Nuclear Medicine*. Grune & Stratton, 1980.

[116] P. Stankiewicz and J. R. Lupski. Structural variation in the human genome and its role in disease. *Annual review of medicine*, 61:437–455, 2010.

[117] J. Starck and F. Murtagh. *Astronomical Image and Data Analysis*. Springer, 2002.

[118] J .L. Starck, E. Pantin, and F. Murtagh. Deconvolution in astronomy: A review. *Publications of the Astronomical Society of the Pacific*, 114(800):1051, 2002.

[119] C. Studer and R. G. Baraniuk. Stable restoration and separation of approximately sparse signals. *Applied and Computational Harmonic Analysis*, 37(1):12–35, 2014.

[120] C. Studer, P. Kuppinger, G. Pope, and H. Bolcskei. Recovery of sparsely corrupted signals. *IEEE Transactions on Information Theory*, 58(5):3115–3130, 2012.

[121] Q. Sun. Recovery of sparsest signals via ?q-minimization. *Applied and Computational Harmonic Analysis*, 32(3):329–341, 2012.

[122] S. R. Swift and L. Trinkle-Mulcahy. Basic principles of FRAP, FLIM and FRET. *Proc R Microsc Soc.*, 39:3–10, 2004.

[123] E. Terpetschnig and D. M. Jameson. Fluorescence lifetime. *ISS Techinical Note*, 2005.

[124] F. Tian, G. Alexandrakis, and H. Liu. Optimization of probe geometry for diffuse optical brain imaging based on measurement density and distribution. *Appl. Opt.*, 48(13):2496–2504, 2009.

[125] R. Tibshirani. Regression shrinkage and selection via the lasso. *Journal of the Royal Statistical Society. Series B (Methodological)*, pages 267–288, 1996.

[126] A. N. Tikhonov, V. Arsenin, and F. John. *Solutions of ill-posed problems*, volume 14. Winston Washington, DC, 1977.

[127] M. B. Unlu and G. Gulsen. Effects of the time dependence of a bioluminescent source on the tomographic reconstruction. *Applied Optics*, 47(6):799–806, 2008.

[128] E. Van Den Berg and M. P Friedlander. Probing the pareto frontier for basis pursuit solutions. *SIAM Journal on Scientific Computing*, 31(2):890–912, 2008.

[129] I. K. Vong. Theory of Poisson point process and its application to traffic modelling. Technical report, Technical Reports, Australian Mathematical Sciences Institute, 2013.

[130] D. Wang, X. Song, and J. Bai. Adaptive-mesh-based algorithm for fluorescence molecular tomography using an analytical solution. *Opt. Express*, 15:9722–9730, Jul 2007.

[131] Lihong V Wang and Hsin-i Wu. *Biomedical Optics: Principles and Imaging.* John Wiley & Sons, 2012.

[132] Y. Wang, J. Cao, and C. Yang. Recovery of seismic wavefields based on compressive sensing by an l1-norm constrained trust region method and the piecewise random subsampling. *Geophysical Journal International*, 187(1):199–213, 2011.

[133] F. Wen, L. Adhikari, P. Liu, R. F. Marcia, and W. Yu. Recovery and demixing of sparse signals using nonconvex regularization. Submitted to *IEEE Transactions on Image Processing*, 2017.

[134] S. J. Wright, R. D. Nowak, and M. Figueiredo. Sparse reconstruction by separable approximation. *IEEE Transactions on Signal Processing*, 57(7):2479–2493, 2009.

[135] P. K. Yalavarthy, B. W. Pogue, H. Dehghani, C. M. Carpenter, S Jiang, and K. D. Paulsen. Structural information within regularization matrices improves near infrared diffuse optical tomography. *Opt. Express*, 15:8043–8058, Jun 2007.

[136] P. K. Yalavarthy, B. W. Pogue, H. Dehghani, and K. D. Paulsen. Weight-matrix structured regularization provides optimal generalized least-squares estimate in diffuse optical tomography. *Medical Physics*, 34(6):2085–2098, 2007.

[137] J. Yan. *Methods for ℓ_p/TV_p Regularized Optimization and Their Applications in Sparse Signal Processing*. PhD thesis, University of Victoria, 2014.

[138] J. Yan and W. Lu. Image denoising by generalized total variation regularization and least squares fidelity. *Multidimensional Systems and Signal Processing*, 26(1):243–266, 2015.

[139] J. Yang and Y. Zhang. Alternating direction algorithms for ℓ_1-problems in compressive sensing. *SIAM journal on scientific computing*, 33(1):250–278, 2011.

[140] J. Yu, J. Cheng, Y. Hou, and X. He. Sparse reconstruction for fluorescence molecular tomography via a fast iterative algorithm. *Journal of Innovative Optical Health Sciences*, 07(03):1450008, 2014.

[141] J. Yu, S.V.N. Vishwanathan, S. Günter, and N. N. Schraudolph. A quasi-Newton approach to nonsmooth convex optimization problems in machine learning. *The Journal of Machine Learning Research*, 11:1145–1200, 2010.

[142] Q. Zhang, R. Plemmons, D. Kittle, D. Brady, and S. Prasad. Joint segmentation and reconstruction of hyperspectral data with compressed measurements. *Applied Optics*, 50(22):4417–4435, 2011.

[143] X. Zhang, Y. Lu, and T. Chan. A novel sparsity reconstruction method from poisson data for 3d bioluminescence tomography. *Journal of scientific computing*, 50(3):519–535, 2012.

[144] Y. Zhang, J. Yang, and W. Yin. User's guide for YALL1: Your ALgorithms for L1 optimization. *Technique report*, pages 09–17, 2009.

[145] G. Zhou, X. Zhao, and W. Dai. Low rank matrix completion: A smoothed l0-search. In *2012 50th Annual Allerton Conference on Communication, Control, and Computing (Allerton)*, pages 1010–1017. IEEE, 2012.

[146] D. Zhu and C. Li. Nonconvex regularizations in fluorescence molecular tomography for sparsity enhancement. *Physics in Medicine and Biology*, 59(12):2901–2912, 2014.

[147] D. Zhu and C. Li. Nonuniform update for sparse target recovery in fluorescence molecular tomography accelerated by ordered subsets. *Biomed. Opt. Express*, 5(12):4249–4259, Dec 2014.

[148] W. Zuo, D. Meng, L. Zhang, X. Feng, and D. Zhang. A generalized iterated shrinkage algorithm for non-convex sparse coding. In *Computer Vision (ICCV), 2013 IEEE International Conference on*, pages 217–224, Dec 2013.